Statistical anatomical modelling for efficient and personalised spine biomechanical models

I. Castro Mateos

A thesis submitted for the degree of

Doctor of Philosophy (PhD)

2016

Statistical anatomical modelling for efficient and personalised spine biomechanical models

Isaac Castro Mateos

Department of Electronic and Electrical Engineering

The University of Sheffield

A thesis submitted for the degree of

Doctor of Philosophy (PhD)

March, 2016

To my beloved wife, Rui Hua, for her useful comments and her zui hao chi de fan

Abstract

Personalised medicine is redefining the present and future of healthcare by increasing treatment efficacy and predicting diseases before they actually manifest. This innovative approach takes into consideration patient's unique genes, environment, and lifestyle. An essential component is physics-based simulations, which allows the outcome of a treatment or a disease to be replicated and visualised using a computer. The main requirement to perform this type of simulation is to build patient-specific models. These models require the extraction of realistic object geometries from images, as well as the detection of diseases or deformities to improve the estimation of the material properties of the studied object.

The aim of this thesis was the design of a general framework for creating patient-specific models for biomechanical simulations using a framework based on statistical shape models. The proposed methodology was tested on the construction of spine models, including vertebrae and intervertebral discs (IVD).

The proposed framework is divided into three well defined components:

The paramount and first step is the extraction of the organ or anatomical structure from medical images. In the case of the spine, IVDs and vertebrae were extracted from Magnetic Resonance images (MRI) and Computed Tomography (CT), respectively.

The second step is the classification of objects according to different factors, for instance, bones by its type and grade of fracture or IVDs by its degree of degeneration. This process is essential to properly model material properties, which depends on the possible pathologies of the tissue.

The last component of the framework is the creation of the patient-specific model itself by combining the information from previous steps.

The behaviour of the developed algorithms was tested using different datasets of spine images from both computed tomography (CT) and Magnetic resonance (MR) images from different institutions, type of population and image resolution.

Research is to see what everybody else has seen, and to think what nobody else has thought...

Albert Szent-Gyorgyi

Acknowledgement

DECLARATION

I, Isaac Castro Mateos, hereby declare that this thesis is the result of my original work and does not include the outcome of work done in collaboration or by other people except where it is specified, acknowledged or cited. I further state that this dissertation as a whole, or part of it, has not been submitted, or, is being concurrently submitted for a degree, diploma or any other qualification at the University of Sheffeld or any other University or similar institution.

Part of this thesis have been extracted from a number of publications, all of which were written primarily by the author of this dissertation, Isaac Castro Mateos, during and as a result of this Ph.D. research. Co-authors provided with images, ground-truth data, and/or feedbacks on the manuscripts and/or experiments.

Publications

Published Journal articles during the thesis

[1] **Castro-Mateos, Isaac**; Pozo, José M.; Cootes, Timothy F.; Wilkinson, J. Mark; Eastell, Richard; and Frangi, Alejandro F. "Statistical Shape and Appearance Models in Osteoporosis." *Current osteoporosis reports* 12, no. 2 (2014): 163-173.

[2] **Castro-Mateos, Isaac**; Pozo, José M.; Eltes, Peter E.; Del Rio, Luis; Lazary, Aron; and Frangi, Alejandro F. "3D segmentation of annulus fibrosus and nucleus pulposus from T2-weighted magnetic resonance images." *Physics in medicine and biology* 59, no. 24 (2014): 7847.

[3] **Castro-Mateos, Isaac**; Pozo, José; Pereañez, Marco; Lekadir, Karim; Lazary, Aron; and Frangi, Alejandro F. "Statistical interspace models (SIMs): Application to robust 3D spine segmentation" *IEEE T Med Imaging* 34,8 (2015); 1663 – 1675.

[4] Pereañez, Marco; Lekadir, Karim; **Castro-Mateos, Isaac**; Pozo, José; and Frangi, Alejandro F. "Accurate Segmentation of Vertebral Bodies and Processes using Statistical Shape Decomposition and Conditional Models." *IEEE T Med Imaging*,

[5] Jianhua,Yao; Burns, Joseph E; Forsberg, Daniel; Seitel, Alexander; Rasoulian, Abtin; Abolmaesumi, Purang; Hammernik, Kerstin; Urschler, Martin; Ibragimov, Bulat; Korez, Robert; Vrtovec, Tomaz; **Castro-Mateos, Isaac** and others. "A Multicenter Milestone Study of Clinical Vertebral CT Segmentation." *Computerized Medical Imaging and Graphics*, 2016

[6] Malandrino, Andrea; Pozo, José M.; **Castro-Mateos, Isaac**; Frangi, Alejandro F.; van Rijsbergen, Marc M.; Ito, Keita; Wilke, Hans-Joachim; Dao, Tien Tuan; Ho Ba Tho, Marie-Christine; and Noailly, Jérôme. "On the relative relevance of subject-specific geometries and degeneration-specific mechanical properties for the study of cell death in human intervertebral disk models." *Frontiers in bioengineering and biotechnology* 3 (2015).

Published Conference papers during the thesis

[7] **Castro-Mateos, Isaac**; Pozo, José M.; Lazary, Aron; and Frangi, Alejandro F. "2D segmentation of intervertebral discs and its degree of degeneration from T2-weighted magnetic resonance images." *In SPIE Medical Imaging, pp. 903517-903517. International Society for Optics and Photonics*, 2014.

[8] Ravikumar, Nishant; **Castro-Mateos, Isaac**, Pozo, José M.; Frangi, Alejandro F.; and Taylor, Zeike. "3D active shape models of human brain structures: application

to patient-specific mesh generation." *In SPIE Medical Imaging*, pp. 94142D-94142D. International Society for Optics and Photonics (2015).

Published Book chapters during the thesis

[9] **Castro-Mateos, Isaac**; Pozo, José M.; Lazary, Aron; and Frangi, Alejandro F. "3D Vertebra segmentation by feature selection active shape model." *In Recent Advances in Computational Methods and Clinical Applications for Spine Imaging*, pp. 241-245. Springer International Publishing, 2015.

[10] Pereañez, Marco; Lekadir, Karim; Hoogendoorn, Corné; **Castro-Mateos, Isaac**; and Frangi, Alejandro F. "Detailed Vertebral Segmentation Using Part-Based Decomposition and Conditional Shape Models." *In Recent Advances in Computational Methods and Clinical Applications for Spine Imaging*, pp. 95-103. Springer International Publishing, 2015.

To be published journal articles and conference

[11] **Castro-Mateos, Isaac**; Hua, Rui; Pozo, José M.; Lazary, A.; and Alejandro F. Frangi. "Intervertebral disc classification by its degree of degeneration from T2-Weighted Magnetic Resonance Images." *Accepted for publication at The European Spine Journal*, 2016.

[12] **Castro-Mateos, Isaac**; Pozo, José M.; and Frangi, Alejandro F. "Multi level Statistical Shape Model (MLSSM) with rebalancing: Application to Spine modelling." *Submitted for publication in the Med Imag Analysis*, 2015.

[13] **Castro-Mateos, Isaac**; Pozo, José M.; Lazary, Aron; and Frangi, Alejandro F. "Automatic construction of patient-specific finite-element mesh of the spine from IVDs and vertebra segmentations." *Accepted for publication in SPIE Medical Imaging. International Society for Optics and Photonics*, 2016.

Contents

List of Figures

xiv

List of Tables

Chapter 1

Introduction

1.1 Motivation

Computer-based simulations and virtual reality have been established as an important tool in the medical field [1]. They are being employed to help physicians to study diseases or conditions [2, 3], estimating outcomes of treatments [4–6], practising surgeries [7] or predicting the circumstances for some medical conditions to develop [8, 9].

An important building block of these simulations is the patient-specific anatomical model that represents the shape of the organ or anatomical region to study. These anatomical regions are commonly extracted from one or more images of the same or different modalities, and they are required to have anatomically correct geometries. An object geometry is considered as anatomically correct when it does not contain overlaps, unrealistic orientations or impossible separations between its parts.

In the literature, one of the most common type of simulations is the one employing finite element methods [10–12]. This kind of methods requires the anatomical model to be a volumetric mesh (VM). This VM is composed of different elements that commonly contain values to indicate the material properties of the studied object. Two important ingredients to compute the material properties are the intensity of the image and a label in each segmented structure that provides information of the tissue type and conditions for computing the material properties. For instance, the degree of degeneration of intervertebral discs is an indicator of its amount of water and collagen, which

influence the viscosity, resistance and other material properties.

The process of extracting the region of an image corresponding to the different tissues or structures of interest is called segmentation. In the area of biomechanical simulations, segmentations are commonly achieved by manual means [13]. Accurate and automatic medical image segmentation is an open problem, which has been tackled with multiple approaches. Such as region-based [14, 15], probability- [16–18], template- [19] or model-based approaches [20–23].

Once the structures are segmented, the labelling of different objects is a classification problem. There exist a myriad of classification algorithms [24–31] available in the literature. The most common approach requires as first step the computation of shape and/or intensity features from the object to classify.

In these two applications statistical shape models (SSM) [32] and statistical appearance models (SAM) [33] are commonly employed as a mean to encode the shape and intensity variation of objects within a selected population. In segmentation, this prior information enables the possibility of restricting the shape and intensity of objects into those of the population used to create the models. In classification, the common approach is to use the parameters extracted from the models in a standard classifier, although the SSM or SAM may be used as a classifier by itself.

In this PhD thesis, SSMs were extensively used and two new types of statistical models were proposed: The Statistical Interspace Model (SIM), which encodes information of the spatial relationship between objects (Chapter 4) and the rebalanced multi-level statistical shape model (R-MLSSM), which integrates the information of factors stratifying the population, such as of diseases, disorders or anatomical positions. In this dissertation, the term *Statistical Models* (SM) will be used to refer to the group of all the previous models.

1.2   Thesis Objectives

The goal of this PhD thesis is to design a framework based upon SM, to efficiently generate patient-specific anatomical models to be used in computer-based simulations

to allow the prediction of pathological conditions, outcome of treatment and other medical related issues.

These models require the extraction of patient-specific and anatomically correct object geometries from images. An object geometry is considered as anatomically correct when it does not contain overlaps, unrealistic orientations or impossible separations between its parts. In the case that volumetric meshes are required for the simulation, these models should be labelled according to the different grades of diseases, deformities or conditions that are relevant for the estimation of their material properties, such as the grade of fracture, which provides information about the resistance of the vertebra. The experiments were performed using human spines because of its complexity and medical relevance:

- They contain soft (intervertebral discs) and bone (vertebrae) tissues, which must be extracted from different image modalities.

- They are articulated multi-object structures, containing various intervertebral discs (IVDs) and vertebrae.

- Vertebral processes are complex to model and the inter-process space is commonly invisible with standard image resolutions.

- There exist deformities and diseases that affect the image intensity and material properties, such as IVD degeneration or vertebral fractures.

- A large population suffers from diseases and disorders related to the spine, such as scoliosis or low back pain.

The previous requirements led to the following objectives:

Development of a Segmentation Framework that extracts anatomically correct object shapes with SSMs: Current segmentation frameworks using SSM do not consider the issue of overlap between neighbouring structures. For instance, in the case of vertebra segmentation, where interprocess space may be smaller than the image resolution, overlaps are prompt to occur, resulting in shapes, which are not anatomically

correct. This issue is commonly ignored in the methodologies from the literature because current metrics, such as Dice Similarity Index or Surface-to-Surface distance, mask the effect of these artefacts. However, it is critical for the correct modelling of the biomechanical interactions.

Development of a classification method that can be integrated in the segmentation framework: Diseases, conditions and deformities that affect the material property of objects commonly contain differences in the shape and/or intensity that could be used to improve the segmentation at the same time as labelling the object. Thus, this thesis aims at not only finding a robust classification method but to embed it in the segmentation framework.

Development of an alignment method to merge articulated anatomical structures from different images: Having segmented and labeled structures from different image modalities that belong to the same anatomical object, it is necessary to align them into a single multi-object structure. In the case study, two structures are found: IVDs, extracted from T2-weighted magnetic resonance (T2 MR) images, and vertebrae, acquired from computed tomography (CT) images. This alignment process must cover two different challenges. On the one hand, it should consider that the pose of the patient in MR and CT are different, and on the other hand, the alignment results should be anatomically correct.

Part of the research presented in this thesis was developed in the context of the MySpine project [34]. The steps were integrated in a full pipeline from medical image databases to biomechanical simulations, which was used to process around 200 patients susceptible of lumbar spine surgery.

1.3 Thesis Structure

The thesis is structure into 5 main sections: Literature review of SSMs (one chapter), First objective - The segmentation framework (two chapters), Second objective - The Classification framework (two chapters), Third objective - The alignment framework (one chapter), and the Conclusions of the thesis (one chapter).

Chapter 2 presents an overview of the types of SSMs and SAMs that exist, the general principle for their creation and their main applications. In particular, it will be provided a detailed description of the two applications most relevant to this thesis: the standard segmentation method using SSMs, the Active shape model (ASM) and the procedures to classify objects using these models.

In Chapter 3, a generic segmentation method, based on ASM with a new type of feature set is presented. This strategy produces accurate segmentations and it is not computationally expensive. Its main issue is manifested when dealing with multi-object structures, such as the spine, because each object is segmented individually, which may produce overlaps and/or excessive separation between individual objects. In the case of the IVDs, this issue is never present, because of the large separation between individual objects. However, the separation between vertebral processes is rather small, allowing these issues. Thus, a new segmentation framework was developed (Chapter 4) to overcome this limitation. This method employs a novel statistical model, named statistical interspace model (SIM), to provide information about the space between neighbouring objects. This new framework produces accurate and anatomically correct segmentations, however, it requires a higher computational time. Thus, the previous framework is still preferred for IVD segmentation.

Chapter 5 introduces a method to classify IVDs according to their degree of degeneration. The method was intended to work using solely the mid-sagittal slice of a T2 MR image since this procedure is the clinical standard, and it could be employed in a context where a 3D segmentation is not available. The accuracy of this method was at the same level as that from experts on the field but more objective. The main drawback is that this classification is specific for IVDs and do not fulfil the objective of creating a framework that exploits the natural synergy between segmentation and classification. Thus, Chapter 6 introduces a new type of technique for creating models with multiple factors, such as the grade of vertebral fracture or the stage of a disease. The technique was named rebalanced Multi-level component analysis (R-MLCA) and it was used to create rebalanced multilinear SSMs (R-MLSSM). These models encode the variation in shape of an object according to different factors, allowing higher re-

construction power as well as the ability to classify objects according to these factors simultaneously.

Since IVDs and vertebrae were segmented from different image modalities, the surface meshes corresponding to these two structures are not in the same location or pose. However, these rigid and non-rigid structures form a single articulated object. Thus, Chapter 7 presents a mechanism to align structures of articulated objects extracted from different images, and to create the patient-specific mesh of the whole spine.

Chapter 8 presents a summary, the conclusions and discusses future lines of research. Finally, Appendix A provides a real case of use of the presented method in the context of the European MySpine project [34].

Chapter 2

Statistical Shape and Appearance Models

Statistical Shape models (SSMs) and Statistical Appearance Models (SAMs) were introduced by Cootes and Taylor [32] as a mean to represent the possible variations in shape and appearance of an object that belongs to a specific population. Since then, SSMs and SAMs have been successfully employed in a large number of unalike applications, such as object tracking [35], segmentation [36, 37] or visual speech recognition [38]. In general, they have been proven to be a powerful tool for image analysis [39] and SSMs are going to be the main pillar on which most of the developed algorithms are based on.

This chapter presents an overview of the types of SSMs and SAMs that exist in the literature, the different steps for their creation, and their main applications. In particular, it will be provided a detailed description of their use in segmentation and classification, which are the most relevant applications for understanding this thesis. The chapter is based on one of the articles published out of this dissertation [40].

2.1 Statistical Shape and appearance model generation

2.1.1 Shape representation

Shape parameterisation is an essential but not trivial task, commonly achieved through the use of meshes. A mesh consists of a collection of vertices at specific locations and cells defining how they are interconnected. With respect to their dimensionality, there exist three types of meshes: contours to cover 2D areas [41–44], surface meshes to describe the surface of 3D volumes [45–47], and volumetric meshes (VM) that represent not only the surface but also the interior of the object [48, 49].

Although meshes generally produce an efficient representation of objects, there exist applications where other representations are more appropriate. For instance, when level sets [20] are used, objects are represented with distance maps [50, 51]. Another type of representation is the direct intensity image within the segmented object of interest [52], which provides both shape and appearance information.

(a)　　　　　(b)　　　　　(c)
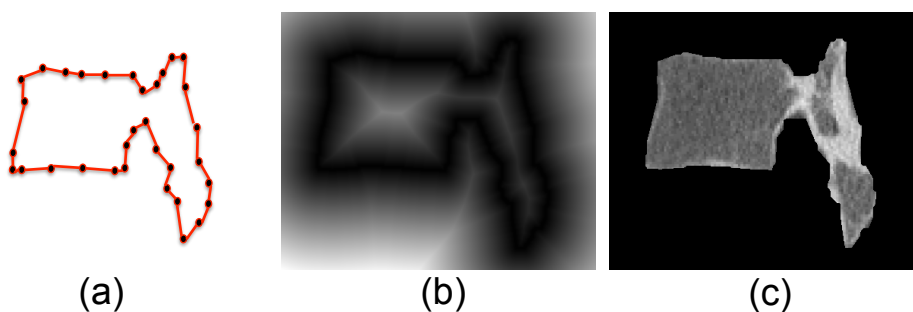
Figure 2.1: Example of the main three types of shape representation in 2D: meshes (a), distance maps (b) and segmented image intensity (c).

Other approaches for shape representation are B-splines grid points [53], Fourier surfaces [54] or medial axis [55, 56].

2.1.2 Appearance representation

The pattern of intensities in and around the object of interest is called the object appearance. Two different types of representation are found:

Intensity on the borders (IB): This type was introduced by Cootes *et al.* [32] as a mechanism to warp shapes within an image to segment the objects of interest. The segmentation framework was named Active Shape Models and it will be explained in Section 2.3.1. IB represents the intensity patterns around the boundary of an object. In its simplest form, it utilises intensity profiles along the perpendicular direction to a surface mesh or contour at each landmark location [42, 46, 57]. However, in order to improve the description of boundaries, new methods employ rectangular patches of pixel intensities around the points of interest [36, 44].

Intensity in the object (IO): This representation contains the intensity within an object. It is commonly used when the object contains a characteristic texture, for instance in face images [36, 58], or when the goal is to reconstruct a 3D shape or image volume from one or multiple 2D scans (Section 2.3.3) [47, 59–61].
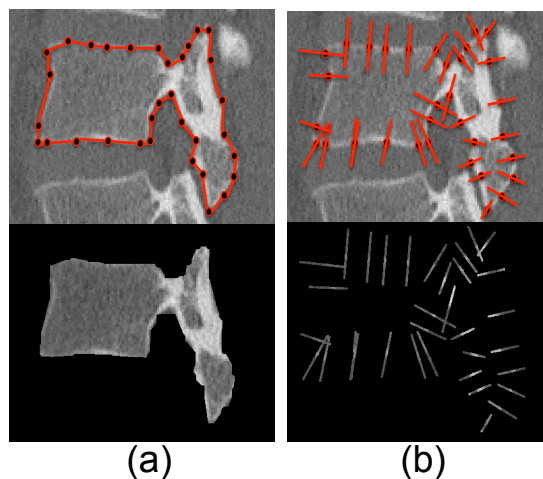
Figure 2.2: Example of the two types of intensity representation, intensity of the borders (a) and intensity inside the object (b). The whole image and the lines that represent the shape are shown on the top and the intensity that is stored at the bottom.

2.1.3   Shape and appearance correspondence

Having selected the type of representation, it is necessary to normalise the shape to a standard reference. This process ensures that each shape has a unique representation. First, all the training shapes are to be described in a consistent manner. For instance,

in the case of meshes, each shape is required to have the same number of landmarks and these landmarks must be located in the same anatomical location. The second part is the elimination of the global orientation, location and scale of each shape. This second step is commonly achieved through the generalised Procrustes alignment [62]. For the definition of the landmarks anatomical correspondence, there exist different approaches:

Manual placement: It is the most common approach for 2D images. An expert pinpoints the landmarks in the same anatomical positions at each of the training samples [42, 43, 63–66]. The immediate extension to 3D is impractical because of the difficulty of visually finding the point correspondence. However, it is feasible to select a small amount of landmarks consistently across the training set, and then, automatically distribute a fixed number of points over the segmented surface with some criterion to maintain the correspondence [67].

Mesh Deformation: A reference mesh is warped to fit each of the shapes in the training set. Subsequently, the reference shape is changed by the mean shape of the newly aligned set, and the process is iteratively repeated until convergence. For the mesh warping Free Form Deformation (FFD) [46, 68] or Thin Plate Splines (TPS) [30, 47] are the usual choices. The training samples may be of different nature, usually meshes [69] or intensity volumes [70] (binary volumes, distance maps, etc.).

Volume to volume: This procedure is fairly common in the case of 3D shapes for SAM [52], SSM [40] and SSM together with SAM [47, 61, 71, 72], but it has also been applied to 2D SAM [41]. This approach requires either a reference image [47, 61] or its segmentation [71] to be deformed to the training samples. In the case of an SSM, the transformations are subsequently applied to the mesh that represents the reference image to result in the training set surfaces. Observe that performing the registration on the segmentation volumes instead of on the intensity image provides higher accuracy but it is necessary to manually segment the whole training set, which is highly time-consuming [60].

Parameterization to parameterization: It employs a bijective map between the shapes and a reference domain [73, 74]. The most common domain is a circle in 2D, and a sphere in 3D, but the most suitable one depends on the topology of the shapes.

Population-based optimization: A common issue of previous methods is that they are biased with respect to the reference shape used to maintain the correspondence between objects. To overcome this limitation, an iterative process with reference refinement is usually applied, but it is not guaranteed that the optimal solution will be achieved. Population-based methods try to find the best parameterisation in the whole training-set at once, so that the optimal solution is attained [75, 76].

2.1.4 Dimensionality reduction

The previous step provides a set of aligned shapes with landmarks correspondence for SSM or an aligned set of intensities representing the interior of an object for the SAM. Each of which could be understood as a point in a high dimensional space. Thus, the distribution in the studied population can be described as a probability density function (pdf) in this high dimensional space. Assuming this pdf takes the form of a Gaussian distribution [32], we can use Principal Component Analysis (PCA) to attain the main axes of the cloud of points. The SSM or SAM represents each case in the population by the mean, $\bar{s}$, and a linear combination of a set of orthonormal principal components (PC), $\mathbf{\Phi}_m$, $m = 1, \ldots, M$. As a result, it is described the possible variations in shape of appearance of the population with respect to the mean

$$\hat{s}^{\text{SSM}} = \bar{s} + \boldsymbol{b}\mathbf{\Phi} \tag{2.1}$$

where $\boldsymbol{b}$ represents the so-called *SM parameters*, which gives a compact encoding of each shape. As a rule of thumb, the parameters $\boldsymbol{b}$ are limited to 3 times the standard deviation, σ_m, of each PC m, which measures their relative influence

$$-3\sigma_m \leq b_m \leq 3\sigma_m, \qquad \forall m = 1, \ldots, M.$$

The aim of this restriction is to avert shapes from deforming excessively (Fig. 2.3 and Fig. 2.4). In a 1-dimensional Gaussian the limit of 3 standard deviations means that 99.7% of the reconstruction ability is preserved. Although, in a N-dimensional Gaussian this is not longer true, it provides a good boundary for the model parameters.
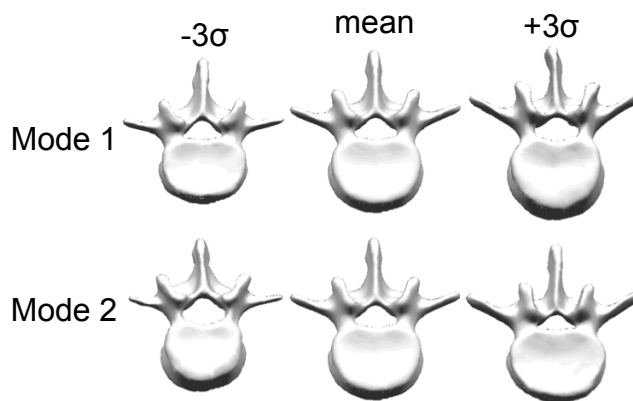
Figure 2.3: Example of the shape deformation given by the modes of variation of an SSM. The figure shows the first two modes of a model created with 30 L3 vertebrae.
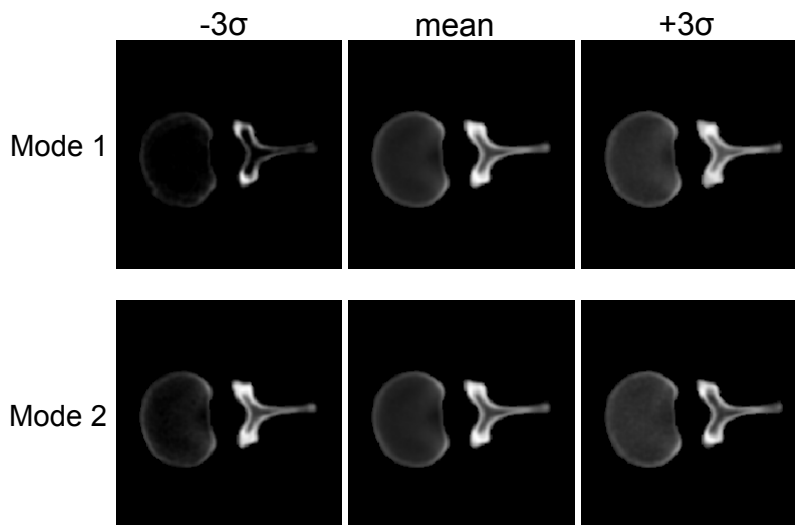
Figure 2.4: Example of the intensity deformation given by the modes of variation of an SAM. The figure shows the first two modes of a model created with 30 L3 vertebrae.

In the literature, different techniques to perform the dimensionality reduction are found. PCA is by far the most common technique, but it holds the assumption of Gaussianity. This assumption is related to the definition of the optimisation problem

that leads to PCA:

$$\underset{\Phi, \bar{s}}{\operatorname{argmin}} \|s - \bar{s} - b\Phi\|^2 \tag{2.2}$$

Three of the most common procedures were compared in the work of Fritscher *et al.* [29]. They employed PCA, independent component analysis (ICA) and locally linear embedded (LLE) to construct the models with the aim of being used to detect femur fracture. They claimed that PCA and LLE performance was superior to that of ICA at predicting the femur "peak-torque to breakaway" and its bone mineral density (BMD).

Other dimensionality reduction techniques used in medical image analysis include a combination of Gaussian distributions [76,77], multi-level component analysis (Chapter 6), maximum autocorrelation factor (MAF) [78] and minimum noise fraction (MNF) [79].

2.1.5   Combined intensity and shape models

Statistical Shape Models may be used on its own, without combining it with an SAM, to perform different applications such as the reconstruction of 3D shapes or images from one or more 2D scans [80, 81] or fracture risk estimation (FRE) [82–84]. However, the combination of both types of models is more common.

In the literature, three different techniques are employed to combine the two models.

Two independent models: The straightforward approach is to construct both models independently and use them together in the application [43, 47, 66, 83, 85]. However, this approach does not take into account the possible correlations between them.

Model of models: This is the most common approach [22, 41, 86–88]. The construction of this model requires PCA to be applied three times. As in the previous case, two independent models are constructed. Subsequently, all the cases are described with these two models and the model parameters are concatenated to be used as input of the third PCA. This approach was proposed by Cootes *et al.* [33] in the context of active appearance model (AAM).

Shape and Intensity Model: This type of SM combines both shape and intensity into one single representation. In the literature, this process is achieved through different procedures: In the InShape model [71], shapes are parameterised using an image deformation fields for x,y, and z coordinates and the appearance using the image intensity. In the model proposed by Yao *et al.* [89], a volumetric mesh (VM) is employed with shapes being represented by the location of the barycentric coordinate of each cell and intensities at each volumetric cell as a Bernstein polynomial function.

2.2 Categories of statistical models

Regardless the type of application for which SSMs and SAMs are used, there exist three categories according to the capacities they provide:

Generative models: A generative model is able to create new instances of a particular object with the same characteristics as the training population. Their main application is in the context of segmentations [42, 90–92], providing a regularisation procedure for the output shapes. They have been also employed for 3D reconstructions either from one or few 2D images [48, 61], or from neighbouring structures [43, 93] in order to estimate the missing information. In addition, they are simple but powerful tools to create an infinite number of artificial shapes with the desired characteristics to perform simulations [68].

Matching models: This category of models is able to assess the similarity between an object, or part of it, and objects from a specific population. The most common example is an intensity model of the borders to be used in a segmentation framework [45, 46, 94], but models using the intensity inside the object has been also employed [17, 95, 96].

Descriptors: The shape or appearance of an object can be described by its correspondent model parameters. Since, they usually have much less components than the original data, they may be employed to reduce the data dimensionality for compression or, more commonly, be used as features for a classifier or regressor [84, 85, 97].

These categories are not mutually exclusive, so that SM may belong to more than one category.

2.3   SSM and SAM applications

There exist a large number of different applications where SSM and SAM have been applied. In this thesis, these models have been mainly employed for segmentation and classification.

2.3.1   Segmentation

Segmentation is the process of identifying an object or region of interest in an image. The segmented object allows the subsequent extraction of clinical parameters [26, 98], or the classification of patients, organs or tissues into different categories [47, 99, 100], or even the construction of patient-specific Volumetric meshes for biomechanical simulations [101–104].

SSMs have been mainly employed as a regularisation tool for 2D and 3D segmentation, so that output shapes hold the same characteristics as the training population used to create the SSM. The segmentation process begins with a model initialisation, consisting on the translation, rotation and scaling of an initial shape, so that, it overlaps with the targeted shape as much as possible. This initialisation process may be either semi-automatic [22, 43, 63] or automatic [42, 64, 71, 94, 105, 106].

After the initialisation, the shape is deformed to match the information contained in the image. There exist different approaches using SSM and/or SAM to perform this step.

Shape and intensity border models

This framework is characterised by the iterative process of deforming a shape within an image using an intensity border model and regularising the output with an SSM. The most popular example of this type of segmentation approach is Active Shape Models (ASM) [24, 42, 43, 107]. An initial shape s is provided. Subsequently, this shape is

deformed within an image to match the object of interest. This deformation process is divided into three stages that are repeated iteratively until convergence:

1. Displace each individual landmark of the shape s following the normal direction of the surface mesh at each landmark position. This process locally optimises the fitting with respect to the SAM to obtain a new shape, s^{SAM}. The SAM employed in ASM does not use a dimensionality reduction procedure, it directly characterises the probability density function (pdf) by the mean and covariance matrix for each landmark intensity profile. The searching algorithm is based on minimising the Mahalanobis distance [32] between the extracted profile of intensities and the computed mean profile at each landmark.

2. Find the scale, rotation and translation that minimises the distance between s and s^{SAM} to get the shape s^{aligned}. This process is commonly performed using Procrustes alignment [62].

3. Project s^{aligned} into the SSM to obtain the new shape s.

$$\boldsymbol{b} = (T^{-1}(\boldsymbol{s}^{\text{aligned}}) - \overline{\boldsymbol{s}})\boldsymbol{\Phi}^{\mathrm{T}}\,,\quad \tilde{\boldsymbol{s}} = T(\overline{\boldsymbol{s}} + \boldsymbol{b}\boldsymbol{\Phi})$$

$$\tilde{b}_m = \begin{cases} -3\sigma_m & \text{if } b_m \leq -3\sigma_m \\ 3\sigma_m & \text{if } b_m \geq 3\sigma_m \qquad \forall m = 1,\ldots,M. \\ b_m & \text{otherwise} \end{cases} \tag{2.3}$$

where M is the number of modes, σ_m is the standard deviation associated to the mode m and $\boldsymbol{\Phi}$ is the matrix with all the modes. The transformation T represents a similarity transformation (scale, rotation and translation) from the mean shape of the model, $\overline{\boldsymbol{s}}$, to the shape at each iteration, $\boldsymbol{s}$.

In order to increase the speed, it is a common practice to repeat the second and third step independently until convergence, before going back to the first step.

This framework is widely used because of its simplicity and robustness. Notwithstanding, ASM suffers from several drawbacks:

- The main limitation of the SSM is the large training dataset required to build a

model with enough degrees of freedom. This issue may be overcome with two different approaches:

1. Adding a relaxation step after the convergence of the ASM to allow more degrees of freedom to the outcome of the segmentation [46, 69] (refer to Chapter 3).

2. Using the statistical model as an energy instead of as a constraining space. This means, a shape will not be projected onto the model space, it will rather be penalised when is outside of the SSM space [108, 109](refer to Chapter 4).

- The intensity models employ single profiles of intensities and assume Gaussianity. New approaches substitute these profiles with patches of intensities around the points and robust classifiers to improve the detection [44, 94, 110, 111].

- The landmark displacement does not take into account the intensity around neighbouring landmarks, which may improve the detection of object regions with non-clear boundaries (Fig. 2.5).
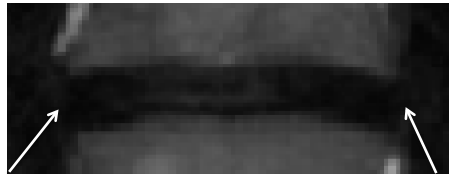
Figure 2.5: Representation of the issue that may rise when using the standard ASM. The white arrows show the unclear separation between an intervertebral disc (IVD) and a muscle, which may be predicted using the separation between the IVD and the vertebrae.

- Although ASM is robust against random outliers, it does not perform properly when a relatively large region of the image has artefacts or noise. Thus, the correct identification of those landmarks and subsequent elimination may improve the results of the segmentation. In the literature, there exist different approaches to equip ASM with a mechanism robust against outliers [96, 112–114].

Shape and appearance model

This framework employs an SAM and an SSM to perform the segmentation. The first and most common type is Active Appearance Model (AAM), introduced by Cootes *et al.* [33]. This segmentation procedure employs a model of models (Section 2.1.5). Similar to ASM, this algorithm is iteratively optimised. The searching algorithm is based on minimising the squared difference between the input image (g_{S}) and the reconstructed appearance from the model (g_{M}),

$$\text{Error} = \|\delta g\|^2, \quad \delta g = g_{\mathrm{S}} - g_{\mathrm{M}}. \tag{2.4}$$

This minimisation process is carried out by linearly relating the difference in the model parameters $\delta c = A \delta g$ with the difference between the two images δg. The most common improvement for the AAM is the technique to construct the matrix A [22, 45, 115].

Although AAM is by far the most common framework, there exist other approaches that employ different models and/or searching techniques. For instance, Fritscher *et al.* [71] employed the model InShapes (Section 2.1.5) to represent the intensity and shape, and level sets as search algorithm.

Shape model without appearance

This framework follows the same strategy as previously presented ASM. The difference lies in that the shape is deformed within the image without the use of an SAM (Section 2.1.2). For instance, in [92] an atlas-based segmentation was employed for this purpose, in [105] a graph cuts approach [116] was used and in [69] a group of trained features were employed.

2.3.2 Classification

SMs have been applied to the classification of objects into different categories following two different approaches.

Model parameters as features

The SSM or SAM is used to represent an object that has been already segmented. Then, these model parameters are used as features in a standard classifier, such as neural network, Logistic Regression or Support vector machine [24–26, 29, 30].

SSM or SAM as classifier

In this scenario the classification is based on the relationship between the shape or intensity of the object with respect to the SSM or SAM [117, 118]. The simplest approach is to create a model for each of the different classes for which the objects can be classified. For instance, if a database contains the shape of hearts with a specific pathology and healthy hearts, two models, $SSM_{Healthy}$ and $SSM_{Pathological}$, can be created one for healthy hearts and one for unhealthy ones. Then, given a new case s, to be classified, it is projected into the two models, using the method described in third step of the ASM, to obtained $s_{Pathological}$ and $s_{Healthy}$. The classification may be computed by measuring the Euclidean distance between s and $s_{Pathological}$ and between s and $s_{Healthy}$ and selecting the class with smaller distance.

In Chapter 6, it is proposed a new statistical model that contains different levels, allowing more accurate segmentations and the possibility of simultaneous classification.

2.3.3   Other applications

2D→3D reconstruction methods

SSMs and SAMs play an important role in the reconstruction of 3D shapes and intensity volumes from a single or multiple 2D scans. In this application, the models are constructed from 3D shapes and images but they are applied to patient-specific 2D images. The most common approach is to use a model of the appearance and minimise the error between the 2D scans and the digitally reconstructed radiography (DRRs) of the 3D model instance [47, 48, 59, 61, 73, 119]. DRR is a projection of a 3D volume following a specific direction to achieve a 2D image simulating the characteristics of the 2D scans. Another common strategy is to perform a mesh registration, adapting

the 3D mesh to the boundaries of the 2D images [80, 81, 120–123] using the SSM for regularisation.

Prediction

Statistical Models have been also embedded in methods to enable the prediction of diseases or deformities in patients before they actually occur. These methods commonly employ the model parameters as features in regressors to estimate the probability that a certain patient will suffer from the anomaly. Examples of this use are found for heart diseases [124, 125], vertebral fracture [52, 82–84] and osteoarthritis from tibia and femur [126].

2.4 Conclusions

Statistical Shape and Appearance models (SSMs and SAMs) encode the possible variations, in shape and appearance, of objects within a particular population. This information has been proved to be valuable in the medical imaging field. For instance, state-of-the-art methods employ model parameters to discriminate between healthy and unhealthy hearts [127, 128] or healthy and fractured bones [93, 97, 129]. In the area of segmentation, active shape models (ASM) have been extensively used owing to its high accuracy and low computational time. However, ASMs come with some inherent disadvantages such as the Gaussian assumption in the intensity model or the increment of required training samples for the SSM with the complexity of the shapes. In the following chapters of this thesis, new SSMs and other type of statistical models, together with segmentation frameworks that exploit them, are introduced to solve several of these problems. The aim is to achieve robust segmentation and classification methods to create anatomically correct patient-specific volumetric shapes for being used in biomechanical simulations.

Chapter 3

Segmentation of Intervertebral Disc (IVD) from 2D MRI sequences using Active Shape Models (ASM) with feature-based searching

This chapter introduces a general framework for segmentation using ASM with a new feature-based searching technique. The framework was tested on T2 magnetic resonance (MR) images to segment the two structures composing intervertebral discs (IVD), the annulus fibrosus and the nucleus pulposus. However, this framework is generic and it could be applied to other organs, or different image modalities as shown in [130], where vertebrae were accurately segmented from computed tomography (CT) images. However, this method segments each object independently and owing to the small separation between vertebral processes, it was found overlaps between neighbouring vertebrae. This issue led to the creation of a different segmentation framework, explained in Chapter 4.

In the case of 2D MR protocols, 3D images are created by dividing the section of a patient's body into a set of slices containing a matrix of tissue voxels. In general, the size of these voxels in the direction perpendicular to the slice is much larger than in the other two. Thus, it is a common clinical practice to acquire images for which the

slices are created following different directions. As explained in the introduction, one goal of this thesis is to provide the intensities of the images in the segmented object, since this information is a requirement to properly estimate the material properties. Thus, a fusion algorithm to combine the intensities from the different views is proposed along this chapter to decrease the size of the voxels by combining the values from the different acquisitions.

Along this chapter, it is also introduced the first labelling of IVDs. The method only discerns between two types, separating IVDs between those whose nucleus pulpous is visible in MR and those which are not. In Chapter 5, a more advanced method is proposed to label IVDs according to their degree of degeneration, which also provides enough information to assess whether the nucleus pulposus is present in the MR image or not.

In terms of improving the ASM framework, two different lines were followed. On one side the searching technique is modified from the intensity boundary model to a feature-based searching technique. On the other side, a relaxation technique is employed to provide more flexibility in the segmentation to compensate for low number of training cases.

This chapter was adapted from the publication of the author of this thesis *et al.* [69].

3.1 Motivation

The intervertebral discs (IVDs) are cartilaginous tissues responsible for the spinal movements. They lie between every two vertebral bodies (VB) to absorb and distribute the loads that the back stands. However, they usually undergo degenerative changes due to age, genetics and lifestyle [131], which are commonly associated with low back pain [132].

IVDs have two well-defined parts, the nucleus pulposus, whose water content drastically varies with the degree of degeneration, and the annulus fibrosus, of nearly constant low water content.

Magnetic resonance imaging is considered the state-of-the-art for IVD visualisa-

tion, since it is non-invasive and the soft tissue contrast is especially high [133]. Physicians base their radiological diagnosis of disc degeneration on 2D analysis of T2-weighted MR images, since this modality can measure water content correlated with the degree of degeneration (Fig. 3.1).

In order to help physicians in the understanding, diagnosis, and/or evaluation of surgical options for low back pain, biomechanical models may be employed [134,135]. In the case of the spine, a critical input is the 3D patient-specific geometries of the IVDs, which are usually achieved by manual segmentation of the medical images [13]. Therefore, an automatic method to perform IVD segmentation can greatly ease the modelling process. Segmentation of the IVDs may also be employed to extract medical information such as the height of the IVDs, which is commonly used to follow-up patients and suffer from an important inter and intra observer variability.

(a)   (b)

Figure 3.1: The IVD is presented in this figure, showing one of the most common cause of low back pain, a herniation, in (a) and its two different anatomical structures, the annulus fibrosus and nucleus pulposus, in (b).

However, disc segmentation is a difficult task, since the annuli and muscles intensities are similar. Therefore, algorithms such as region growing [136], watershed [137] or snakes [138] may leak to neighbour structures. In addition, low-resolution images can occlude thin annulus walls, leaving the nucleus and vertebra connected in the image, which might have similar intensity values. Furthermore, the intensity-levels vary between different patients and along the spine, which complicates the use of Intensity Appearance Models (IAM) [23], Fig. 3.2 shows various of these problems.

These difficulties have resulted in not much research on this field, despite the clinical relevance of the 3D segmentation of IVDs. The previous work is mainly focused on the 2D annulus fibrosus segmentation from mid-sagittal slice [16, 21, 57, 139–143]. Seifert *et al.* [144] introduced a 3D segmentation algorithm for cervical IVDs and
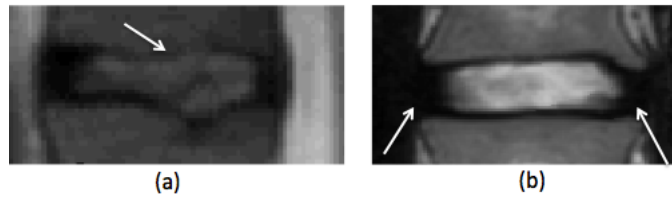
Figure 3.2: Difficulties of IVD segmentation. (a) The white arrow shows a thin annulus' wall, which may hardness the segmentation of the IVD, since the intensity of the nucleus and vertebra are similar in this case. (b) White arrows point at the intersection between the IVD and the muscle, which is not clear since the intensity of both tissues are similar.

other cervical soft tissues. Their approach is based on segmenting each MR slice independently and then, merging them to achieve the 3D segmentation. However, the evaluation of the method was performed in the 2D segmentations, and resulted in a mean error higher than a 1.5 pixels.

Recently, the author of this thesis *et al.* [23] proposed a method based on Active Shape Models (ASM) to achieve 3D segmentations. However, it was only applied to L3-L4 discs and it performed poorly on degenerated IVDs. Furthermore, it was necessary to manually pinpoint the centre of the IVDs. To solve this last problem Neubert *et al.* [145], first detected the spinal cord in order to place the initial position of the IVDs and then they were segmented using ASM. Although they reported good accuracy, the evaluation was performed on a small database of 14 healthy subjects. In general, processing diseased IVDs is substantially more challenging than healthy ones.

Another recent work based watershed approach was proposed by Chevrefils *et al.* [146] to reduce the over-segmentation of their previous work [137], although not completely.

The work of Haq *et al.* [147] is an interested case of using mechanical models for segmentation. In their paper, a simplex model is used to deform an ellipsoid mesh into the image intensities using the Newtonian motion equation to move the vertices, constrained by an internal energy to enforce smoothness. This method follows the same principal as snakes and therefore has the same weakness, which is the leaking problem to the muscles.

The use of probabilistic approaches to perform localisation and then segmentation

has been also tackled [148, 149]. These methods have two steps: First the probability of each pixel to be the centre of an IVD is computed. Second, the probability of the pixels surrounding the centres to be part of the IVD is calculated. The main issue is that this approaches employ only intensity similarity to find the boundaries. Thus, leakage is prompt to happen in the coronal direction. To solve this issue, in [149] the location of the pixels with respect to the centre was employed as an extra information. However, it is not explained how this relative distance information is used.

To the best of the knowledge of the author of this thesis, no method has been proposed to handle 3D MR segmentation of the nucleus pulposus in humans. However, there exists the work of Bechara *et al.* [150], in which the nucleus pulposus of rabbits were semi-automatically segmented. The method requires the user to draw a square around the IVD and select the best isoline that defines the nucleus.

The proposed pipeline to obtain 3D segmentation of IVD's nuclei and annuli employs T2-weighted MR images (Fig. 3.3). This type of protocol has the drawback of a large inter-slice space.

Thus, a fusion algorithm that creates high-resolution volumes (Section 3.2.1), from various acquisitions, was included by improving the work of Yao *et al.* [151].

The segmentation technique used for IVD segmentation is based on Active Shape Models (ASM). This framework employs an intensity energy explained in section 2.3.1. However, this standard procedure do not provide good results with the employed image modality. The variation of the MR intensities with respect to the patients is very different to that of a Gaussian shape.

In the literature, there are different approaches to deform a shape within the intensities as part of an ASM-based segmentation method [36, 92, 105, 152, 153]. Among these techniques, feature-based approaches has been proven to be accurate and reliable [111]. These methods are based on extracting a patch of intensities surrounding the point that is to be displaced. Subsequently, a group of features is computed, such as SIFT [153, 154], Haar-features [44] or statistics over the histogram of intensities [36, 152]. Then, a classifier [36, 152, 153] or a regressor [44, 111] is used to estimate the best position to move the point. In order to eliminate the use of a classifier

or a regressor and speed up the process, herein it is proposed a new algorithm, based only on a set of features.

The segmentation using ASM is followed by a relaxation step (Section 3.2.5) to increase the accuracy of the results based on a mesh to mesh morphing based on B-splines [155]. Although the segmentation procedure is finalised, in the case of nucleus segmentation, an additional step is required to detect whether the nucleus is present or not in the image (Section 3.2.6).

The main contributions of the research explained in this chapter are:

- An improved algorithm to fuse coronal and sagittal MR acquisitions.

- An algorithm to select the best features to segment different tissues.

- A detection step to discern whether the nucleus is present or not in an image.

- A relaxation step based on a non-rigid registration using B-Splines.
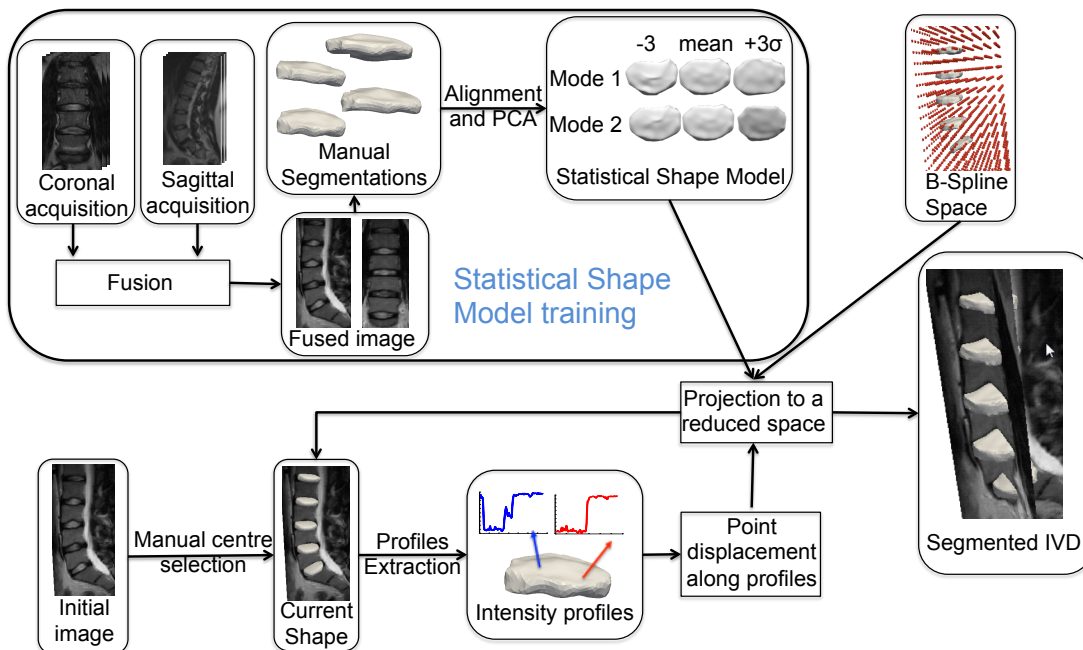
Figure 3.3: Pipeline of the method. The Statistical Shape Model (SSM) creation is depicted in the top part of the figure, whereas the Segmentation procedure is below the former.

3.2   Annulus and nucleus segmentation

3.2.1   Image Fusion

Due to the large spacing between slices in common protocols of MR images, an algorithm to fuse coronal and sagittal acquisitions was developed. The outcome is a denser volume with isotropic voxels of $0.68 \times 0.68 \times 0.68 \ mm^3$. The algorithm is based on the work of [151], who developed a fusion algorithm based on a bi-linear interpolation. The main drawback of their approach is the requirement of a linear correlation between the intensity of the input volumes, which is not the case in MR images, since they suffer from local intensity bias [156]. Thus, herein it is proposed a new non-local rescaling technique, based on the intensities of overlapping voxels (Fig. 3.4) to overcome this problem. An extension of the bi-linear interpolation technique for the case of having more than 2 images is presented in the Appendix B.

The intensity rescaling step starts by dividing the sagittal and coronal acquisitions into cubes of the size of the slice gap, centred in the intersection between the two MR image slices. For each cube, the mean value of the ratio between the overlapping voxels (sagittal over coronal) is computed (Fig. 3.5) and stored to create a matrix of weights. This matrix is used to rescale the coronal volume by multiplying the intensities inside each cube by the correspondent weight.

3.2.2   Image segmentations and ground truth.

All the manual segmentations were delineated using the fused images, presented in the previous section, since they provide clearer edges in all directions. I performed the segmentations of the 295 annuli and nuclei using the open source software ITK-SNAP [157], under an expert supervision. These segmentations were used as a ground truth (GT) for measuring the accuracy of the segmentations. In order to evaluate the intra and inter-observer variabilities, a group of 10 patients (50 nuclei and annuli) was selected (further information is provided in Section 3.4.2).
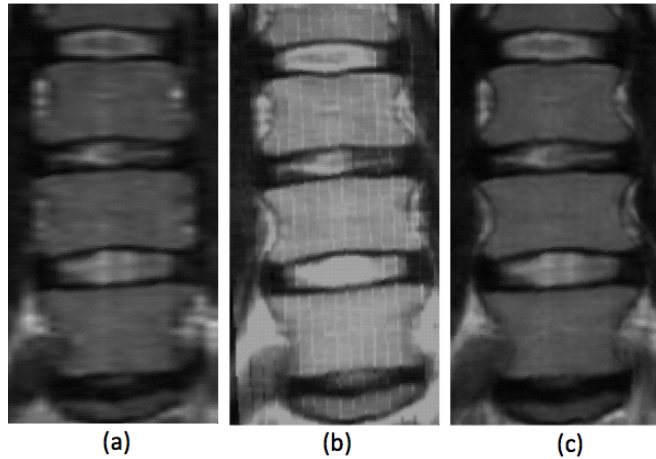
Figure 3.4: Interpolated coronal slice using different approaches. (a) From only a sagittal volume, the resolution is 0.68×4 mm^2, which makes the boundaries look blurred. (b) Image fusion algorithm without the intensity rescaling. (c) Image fusion with intensity-rescaling and bi-linear interpolation.

3.2.3 Statistical Shape Models (SSM).

SSMs were introduced in Chapter 2. These models are powerful tools to restrict the object shapes to the most likely outcome within the variability of a certain population.

For the IVDs of the lumbar spine, 10 different SSMs were built, two for each individual IVD (one for the annulus and one for the nucleus).

As common practice, the least influential modes are usually discarded, since the SSM usually contains noise. The simplest mechanism is to eliminate those eigenvectors whose eigenvalues contribution is lower than a certain threshold, commonly 5% or 10%. With the latter, it results in 21, 21, 20, 19, 16 modes from L1-L2 to L5-S1, respectively. The first two modes of variation of the L3-L4 IVD are shown in Fig. 3.6.

3.2.4 Segmentation process: ASM with feature-based searching

The segmentation process follows the ASM framework explained in Chapter 2.3.1. A mesh is deformed within the image intensity and projected onto the SSM space, iteratively until convergence. In addition, a relaxation step was added after the convergence of the ASM step, in order to allow the segmentation to be outside the SSM space, owing to a limited training set.
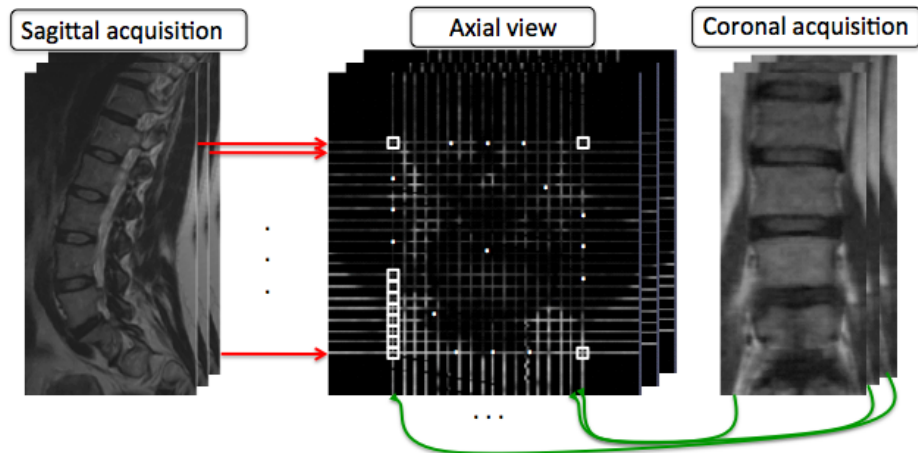
Figure 3.5: Fusion algorithm scheme. Sagittal and coronal slices are located in the same reference system. The white squares in the axial slice represents the cuboids used for the interpolation. For each cubic, a weight is computed using the mean of a vector of values. This vector contains the ratio between the sagittal and coronal voxel intensities, when they both overlap in the same spatial position.

As explained in the introduction 3.1, the standard ASM does not work properly, since the intensities in the MR images vary across the patient population and spinal position. Thus, herein it is proposed a new algorithm to compute the energy needed for the point displacement, before the SSM projection. This energy is based on the following features or sub-energies:

1. **Directional derivative along the normal profile pointing outwards**. This feature searches for changes from high to low intensity values in the image.

2. **Directional derivative along the normal profile pointing inwards.** This feature searches for changes from low to high intensity values in the image.

3. **Intensity in the profiles.** This feature searches for the minimum intensity in the profile.

4. **Opposite of the intensity profile.** This feature searches for the maximum intensity in the profile.

5. **Distance to the initial point in each iteration.** This feature serves as a spring energy, which penalises large movements.
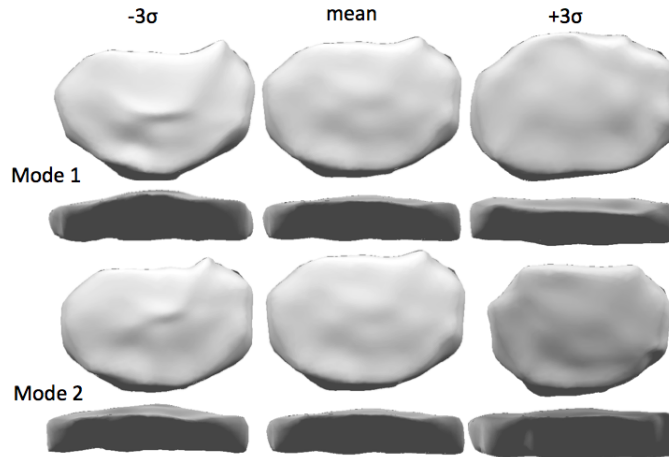
Figure 3.6: The mean shape and the first two modes of variation of the SSM, varying between -3 and $+3$ standard deviations (σ).

6. **Mahalanobis distance to the mean intensity profile.** This feature seeks the displacement that achieves the minimum mahalanobis distance between the profile and a trained mean profile [32].

The weighted average of the features is used to calculate the energy of every candidate position, which is selected as the one with the minimum energy. These weights were calculated with an algorithm that searches the values that maximise the measurements explained in Section 3.4.2.

This algorithm is divided into two stages and is optimised using a multi-resolution greedy approach to speed-up. In the first stage, the weight of each feature is individually optimised using m iterations. The first time a set of n numbers between 0 and 1 ($\frac{1}{n+1}, \frac{2}{n+1}, \cdots, \frac{n}{n+1}$) is selected. The whole training set (Section 3.4.2) is segmented using each of these n values as feature weight throughout each iteration of its optimisation. The value that provides the highest accuracy is selected for the next iteration. In the following $m-1$ iterations, the set of n numbers will range between the previous and the next values of the selected one.

In this algorithm, the error between the automatic segmentation and the GT was selected as the percentile 95 of the surface-to-surface distance. In addition, the values for m and n were selected as a trade-off between speed and accuracy, $n = 4$ and $m = 3$. This values provide an error below 1.6%, higher accuracy does not provide

---

Algorithm 1 Features and weight selection

 1: - i represents each feature.
 2: - j represents each possible weight for feature i.
 3: - n number of possible weights for the features.
 4: - $selection\{i\} \leftarrow$ true in all positions. It contains the selected features.
 5: - $BW\{i\} \leftarrow$ the best weight for each feature
 6: - $BCI \leftarrow$ Minimum error between the automatic segmentation and the GT
 7: between segmented and ground truth meshes.
 8: - $CW\{i\} \leftarrow$ current value of the weights for the features.
 9: **for** iteration from 0 to 1 **do**
10:    - $IP\{i\} \leftarrow 0$ initial position for each feature.
11:    - $EP\{i\} \leftarrow 1$ end position for each feature.
12:    **for** Each scale m **do**
13:       **for** each feature i **do**
14:          $CW\{i\} \leftarrow BW\{i\}$ Copy best weights to the current weights.
15:          $step \leftarrow \frac{EP(i)-IP(i)}{n+1}$
16:          **if** selection(i) == true **then**
17:             **for** j = 1 to n **do**
18:                $CW(i) \leftarrow IP(i) + j * step$
19:                Compute the segmentation of the training set
20:                using features when selection == true, and weights = CW.
21:                $CI \leftarrow$ Percentil 95 of the surface-to-surface distance
22:                between segmented and ground truth meshes.
23:                **if** $CI < BCI$ **then**
24:                   $BCI \leftarrow CI$
25:                   $BW(i) \leftarrow CW(i)$
26:                   $IP(i) \leftarrow CW(i) - step$
27:                   $EP(i) \leftarrow CW(i) + step$
28:    **for** each feature **do**
29:       **if** $BW(i) < 0.05$ **then**
30:          $selection[i] \leftarrow false$

---

visual difference in the segmentations.

Once, the whole set of weights is achieved, they are sorted and normalised. Then, an accumulative summation is performed and weights, whose values are over 0.95, meaning their contribution is smaller than 5%, are removed and the process is repeated with only the selected features.

The algorithm selected three features for the annulus, the directional derivative pointing outwards, the intensity in the profile, and the distance from the current position. Therefore, the cost function to minimise in each profile is:

$$\mathbf{p}_i^{new} = \mathrm{argmin}(\alpha I(\mathbf{v}_i) + \beta \hat{\mathbf{n}}(\mathbf{s}) \cdot \nabla I(\mathbf{v}_i) + \gamma E(\mathbf{v}_i, \mathbf{p}_i)) \tag{3.1}$$

Where $\mathbf{p}_i$ is the old position of the mesh point i and $\mathbf{p}_i^{new}$ is the new one, $\mathbf{v}_i$ is a vector, whose values are the global positions along the normal direction of the surface mesh at point $\mathbf{p}_i$, I is the image intensity and n is the direction of $\mathbf{p}_i$ from inside to outside the IVD. $E(\mathbf{u}, \mathbf{v})$ represents the Euclidean distance between $\mathbf{u}$ and $\mathbf{v}$, $\mathbf{u} \cdot \mathbf{v}$ is the inner product. The trained weights were α, β and γ .

In the case of the nucleus segmentation, the algorithm did not select the Euclidean distance and the directional derivative was selected pointing inwards instead of outwards.

Having displaced all the points of the mesh, a shape $\mathbf{s}$ is created and is then projected on the SSM space as explained in Chapter 2.3.1.

3.2.5 Relaxation step

The use of SSMs has the drawback of requiring a large training shapes to achieve a model with enough degrees of freedom. To overcome this limitation, in this thesis it is proposed to use a relaxation step in order to improve the segmentation result of those IVDs whose shape is out of the SSM generalisation ability. This step is similar to the one proposed in [46], but using B-splines instead of a connected graph smoothed by an optimal graph-searching algorithm.

This relaxation step follows the same procedure as the above-mentioned segmentation algorithm. However, instead of projecting the shape into the SSM space, it is

projected into the B-splines space, whose degree of freedom is higher.

The number of steps was set up to two for the annulus and six for the nucleus, because further iterations did not improve the results on the training set.

3.2.6   Nucleus detection

Having segmented nucleus and annulus, it is necessary to verify whether the nucleus exists or the statistical model created a shape, when no boundaries were found (Fig. 3.7). The classification between nucleus and no-nucleus was computed by calculating the ratio of the mean intensity inside the nucleus and that inside the annulus. When this value was greater than a threshold, it was considered to be a real nucleus and discarded otherwise.

$$\frac{Nucleus\_Intensity - Annulus\_Intensity}{Nucleus\_Intensity} > threshold \tag{3.2}$$

| (a) | (b) | (c) | (d) | (e) |
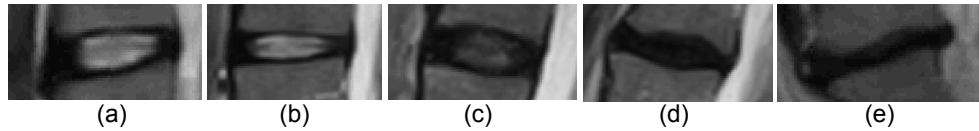
Figure 3.7: Example of the five different degrees of IVD degeneration, I to V going from (a) to (e). The degree of degeneration is related to the nucleus intensity.

The threshold was visually selected by choosing a point in the elbow region of the ROC curve. Equation 3.2 was used, selecting thresholds from 0 to 1, with a step of 0.05. Plotting Sensitivity and Specificity with different thresholds gave an area under the curve (aROC) of 0.98 (Fig. 3.8).

$$Specificity = \frac{FP}{FP + TN} \quad Sensitivity = \frac{TP}{TP + FN} \tag{3.3}$$

TP, FP, FN and TN stand for true positive, false positive, false negative and true negative, respectively.
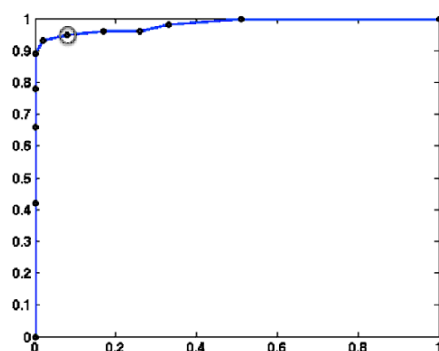
Figure 3.8: ROC of the nucleus detection. The black points represent the obtained values with a defined threshold, which goes from 0 to 1 and with a step of 0.05 . The points at (0,0) and (1,1) were extrapolations, since there was no threshold giving such values. The grey circle represents the selected threshold (value = 0.2).

3.3 Data

The employed database consists of T2-weighted MR coronal and sagittal acquisitions of 59 human lumbar spines. 30 of them were collected using an open 0.4T MR machine (Hitachi, Twinsburg, OH) at the National Center for Spinal Disorders (NCSD) located in Budapest, Hungary. The remaining 29 images were acquired with a 1.5T MR machine from the CETIR Grup Medic (Barcelona, Spain). Patients were 33 males and 26 females with a mean age of 40 (age interval: 27-62 years). Those patients were selected for participating in the European MySpine project [34]. This project required patients with low back pain (LBP), but without having diseases or deformities that highly alter the normal shape of the spine, such as high degree of scoliosis. The study design received approval of the institutional review board and written informed consent was retrieved from all subjects.

All the images have a resolution of $0.68{\times}0.68\ mm^2$ and a spacing between slices of 4.0 mm or 4.4 mm when collected from NCSD or CETIR, respectively.

Pfirrmann classification [158] was employed to group the IVDs by their degree of degeneration (grades I to V). The total number of discs was 295 and the number per degree of degeneration and position is presented in Table 3.1.

Table 3.1: number of IVDs per position and degree of degeneration.

Lumbar	Degree of degeneration				
segments	I	II	III	IV	V
L1-L2	5	23	29	2	0
L2-L3	5	25	24	5	0
L3-L4	12	18	20	9	0
L4-L5	6	7	21	23	2
L5-S1	2	9	18	21	9
Sum	**30**	**81**	**113**	**60**	**11**

3.4 Results

3.4.1 Implementation details

The proposed framework employs:

- the weights for the annulus features: $1.0mm/in$ for the directional gradient, $0.5in^{-1}$ for the intensity and $0.3mm^{-1}$ for the distance feature.

- the weights for the nucleus: $1.0mm/in$ for the directional gradient, $0.4in^{-1}$ for the intensity of nucleus features.

- two SSMs per IVD, one for the Annulus and one for the nucleus. Each of them with 1200 landmarks.

- the number of modes for each SSM was selected as the number that keeps 95% of the total variation. This results in 21, 21, 20, 19, 16 for the annuli and 26, 24, 22, 19, 18 for the nuclei.

- a B-Splines grid of $10 \times 8 \times 6$ points.

- The criteria to stop the segmentation was that 99% of the landmarks do not move more than 0.2 times the size of a voxel in the direction of the normal at the specific landmark. This criteria resulted in 10 to 15 iterations. In addition, the maximum number of iterations were set to 20.

- The size of the profiles was set individually for each landmark p of the mesh. In the first iteration, it was set to 15 voxels in the direction pointing outwards and

min$(15, a)$ voxels pointing inwards. The value a is half of the number of voxels from p to the intersection of the mesh and a line following the normal direction of the mesh at p. In the last iteration, they were set to 4 voxels inwards and 4 outwards.

- The number of resolutions was kept to one, since the initialisation already locates the IVDs in a good location.

- The step size for the relaxation step was 3 voxels inwards and outwards.

where the unit in represents the unit of the image intensity.

3.4.2   Evaluation of the method

Evaluation metrics.

Dice Similarity Index (DSI) [159] between the segmented shapes and ground truths were computed to evaluate all the experiments.

$$DSI = \frac{2 \times (GT \cap SM)}{GT + SM} \times 100\% \qquad (3.4)$$

Equation 3.4 defines the DSI measurement, where GT represents the Ground Truth and SM stands for the Segmented Mesh.

In addition, the surface-to-surface distance from the segmented shape to the GT was employed for the evaluation. The mean absolute value (MASD) and the percentile 95 (95-p) were computed from this measurement, as well as the Hausdorff distance, which represents the maximum surface-to-surface distance.

The set of 59 patients was divided into two sub-groups, a training set (29 patients) for the features, weights (Section 3.2.4) and the threshold selection (Section 3.2.6) and a testing sets (30 patients) for the evaluation of the algorithm. Then, leave-one-out tests were performed over the testing set. For each IVD in the testing set, an SSM was built with all the cases, in both the training and testing sets, except the case being evaluated.

In addition, the MASD and 95-p were computed for the reconstructed IVD and ground truth. A reconstruction is defined as the best instance of an SSM for a particular

ground truth. This measurement provides the best result that the SSM is capable to produce and therefore, segmentations using only an SSM are upper bounded to this value.

Inter- and intra-observer variabilities.

The intra- and inter-observer variabilities provide an estimation of the ground-truth reliability. Due to the amount of time that a 3D manual segmentation requires, the evaluation of these two parameters was performed in a sub-set composed of 5 patients from each hospital (set A1). The same expert that segmented the 295 annuli and nuclei segmented the subset of 50 annuli and nuclei once more (set A2). And other two clinical experts segmented the same 10 patients (set B and set C). For each measure, presented in Section 3.4.2, the intra-observer variability was calculated using the set A1 as ground truth and set A2 as the segmented version, and vice versa and then, taking their mean. The inter-observer variability was attained by following the same procedure with set A1, set B and set C. Then, all the possible combinations among them were computed and the result was the average.

The computation of the inter- and intra-observer variabilities requires the selection of the most adequate sub-group of patients. The selection criterion was the group of patients that best represents the distribution of disc degeneration in each spine segment across the population. The search of this group was performed employing a forward sequential feature extraction algorithm [160].

Experiments to evaluate each algorithm component.

In order to evaluate the performance of each part of this framework, the accuracy measures from Section 3.4.2 were computed in the following versions of the algorithm:

1. *Complete pipeline:* The measurements for this evaluation were computed in the testing dataset using the fused volume, the set of trained features and the relaxation steps.

2. *Complete pipeline except fusion:* The fused image was substituted by the sagittal

volume, because it provides better visualisation than the coronal acquisition.

3. *Complete pipeline except the relaxation step:* The relaxation step was not performed.

4. *Complete pipeline without the SSM:* The mesh shape was every time projected into the same B-spline space as in the relaxation step.

5. *Complete pipeline without the trained features:* The Intensity appearance model proposed by [32] was used instead of the trained features.

The first experiment was compared to the other four using a Two-Sample t-test.

3.4.3   Quantitative and Qualitative Evaluation of the method

The accuracy of the segmentation in the complete pipeline (first experiment), for both annulus and nucleus, is presented in Table 3.2. Fig. 3.9 presents a comparison among all the experiments presented in Section 3.4.2, using the measures introduced in Section 3.4.2. These experiments were performed for both the annulus and nucleus. However, only the results of the annulus are shown in the figure, since the performance of the algorithm in both anatomical structures follow the same pattern with respect to the dataset. Therefore, conclusions extracted from the results of the annulus segmentation can be applied to that of the nucleus.

In addition, Fig. 3.10 presents examples of the segmentations with the whole framework.

Table 3.3 shows the reconstruction error, which is the error of the best possible outcomes using the SSM with respect to the ground truth.

Table 3.4 presents the inter- and intra-observer variability of the manual segmentations.

Table 3.5 presents the sensitivity and specificity of the classification between the existence or non-existence of the nucleus in the MR image.

Table 3.2: Accuracy of the IVD (annulus and nucleus) segmentation per degree of degeneration (I to V) with the full pipeline. DSI stands for Dice Similarity Index, MASD is the mean absolute surface-to-surface distance, 95-p is the percentile 95 of the surface-to-surface distance and Hausdorff is the Hausdorff distance.

Structure	Error measure	I	II	III	IV	V	Global
	Mean DSI	88.5%	89%	89.4%	86.4%	82%	88.4%
	2xSTD of DSI	9.1%	5.7%	4.6%	7.4%	12%	7.2%
Annulus	MASD (mm)	0.72	0.66	0.64	0.7	0.68	0.68
	95-p(mm)	1.96	1.82	1.73	1.9	1.87	1.84
	Hausdorff(mm)	5.24	4.4	4.3	4.71	5.57	4.63
	Mean DSI	74.8%	82.5%	83.9%	-	-	77.9%
	2xSTD of DSI	23.8%	24.3%	27.4%	-	-	32%
Nucleus	Mean ND (mm)	1.55	1.67	2.11	-	-	1.88
	95-p (mm)	5.47	5.78	7.44	-	-	6.63
	Hausdorff(mm)	9.05	9.44	9.63	-	-	8.31

Table 3.3: Annulus fibrosus reconstruction error per degree of degeneration. This table shows the average errors across the testing dataset, between the best possible outcome of the SSM for a particular IVD, and its ground truth.

Error measure	I	II	III	IV	V	Global
MASD (mm)	0.48	0.52	0.53	0.57	0.65	0.55
95-p (mm)	1.25	1.35	1.40	1.51	1.76	1.46
Hausdorff(mm)	2.77	3.18	3.18	3.36	4.2	3.34

Table 3.4: Intra and inter-observer variability of the ground truth of the annuli and nuclei.

Error measure	Annulus		Nucleus	
	Intra	Inter	Intra	Inter
Mean DSI	95.1%	85.4%	93.1%	79.3%
2 x STD of DSI	6.4%	8.6%	7.2%	30.8%
MASD (mm)	0.08	1.14	0.22	1.81
95-p (mm)	0.4	3.17	0.6	3.77
Hausdorff(mm)	2.6	5.7	3.8	7.1

(a)   (b)
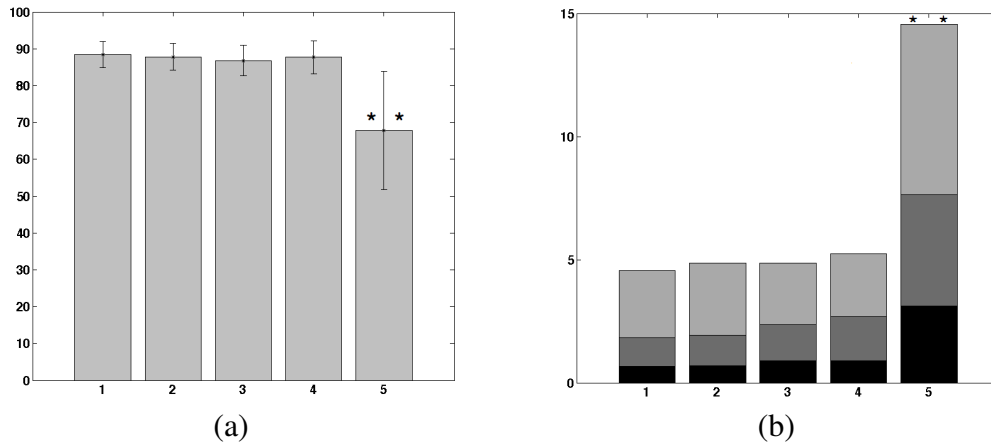
Figure 3.9: Experiments of the evaluation of each component of the algorithm. The abscissae correspond to different experiments. They are organised in the same order as they were explained in Section 3.4.2. The two asterisks over the last experiments shows the t-test comparing with the results from the complete pipeline provides a $p < 0.01$. The rest of the experiments were correlated.(a) Mean DSI as a bar diagram and the standard deviation represented as black line. (b) Mean surface-to-surface distance (black), the 95-percentil (dark grey) and the mean Hausdorff distance (light grey). Note that distances are in millimetres, where the DSI measurements are in percentages.

Table 3.5: Detection rate of the IVD nuclei by visual inspection provided by three experts and the proposed automatic approach. The gold standard was defined as the consensus detection by the three experts using major voting.

Measure	Observers			Automatic method
	First	**Second**	**Third**	
Sensitivity	71.43%	76.19%	80.95%	92.1%
Specificity	8.51%	2.27%	5.84%	3.12%

3.4.4 Computational Cost

The results were obtained using a PC with Intel(R) Xeon CPU E5620 at 2.40 Ghz with 8 GB of RAM and running a 64-bit Windows 7 operating system. All the code was written in C++ using the libraries from the Insight Toolkit [157] for mesh and image basic manipulation. The averaging elapsed time was 61 seconds per patient.

3.5 Discussion

Five different measures were computed for an evaluative purpose: the mean and the approximate 95% confident interval of the DSI, the mean absolute surface-to-surface
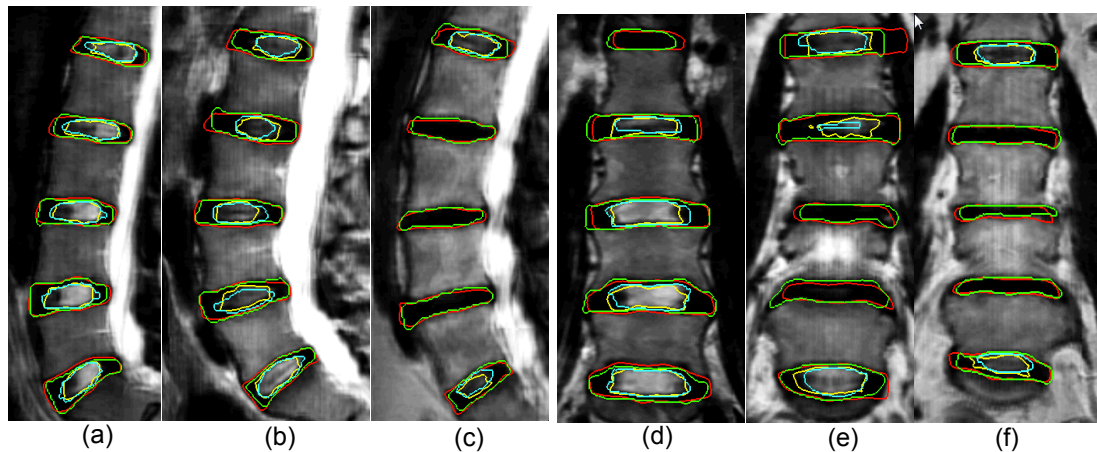
Figure 3.10: The figure shows the results of the algorithm as well as the ground truth for the annulus and nucleus segmentation in three different patients and in two different slices, mid-sagittal (a),(b),(c) and mid-coronal (d),(e),(f). The discs degeneration, from L1-L2 to L5-S1 are 3 3 3 3 5, 3 4 4 4 3, and 3 3 2 2 2, from left to right. The segmented annulus is drawn in red, whereas the ground-truth, in green, the segmented nucleus is in yellow and the ground-truth, in light blue.

distance (MASD), the percentile 95 (95-p) and the Hausdorff distance. The 95% confident interval of the DSI was approximated as the mean $\pm 2 \times$ STD (the Standard Deviation).

The first experiment (first bar in Fig. 3.9) shows the accuracy of the complete pipeline. The above-mentioned measurements of this experiment are presented in Table 3.2, which shows that the proposed method is stable with respect to the degree of degeneration. It is worth mentioning that, since DSI depends on the volume of the objects and the degree V means the IVD collapsed, one voxel difference between the ground truth and the segmented IVD implies a reduction of this measure larger than when the IVD has less degree of degeneration. On the other hand, the surface-to-surface distance does not have this effect as it is shown in the table. This global accuracy is also presented in the first bar of Fig. 3.9.

The second experiment (second bar in Fig. 3.9) was performed to evaluate whether the trained SSM contains enough information to avoid the fusion step during segmentation. The algorithm was applied on images built from sagittal acquisitions instead of using fused images. In both cases, however, the SSM was built from manual segmentations of fused images. Since, a Student t-test over the results on the first and

second experiments showed no statistical difference and no clear visual differences were found, it was concluded that fused images does not introduce significant improvement in the segmentation procedure. However, this step is essential to extract the correct intensities of the MR images and with that compute the material properties for the models.

The segmentation accuracy without the relaxation step (Section 3.2.5) is shown in the third column of Fig. 3.9. Although the difference in accuracy is not statistically significant, this step is important in some cases. For instance, in Fig. 3.11, the output of the statistical model (white contour) does not cover small deformations, which usually occur in high degenerated discs or in those with a peculiar shape. The used database contains around 10% of cases with these characteristics and only 5% of the points in each shape belong to these deformations. Therefore, this problem does not significantly influence the over-all evaluation but it matters for attaining highly accurate results.
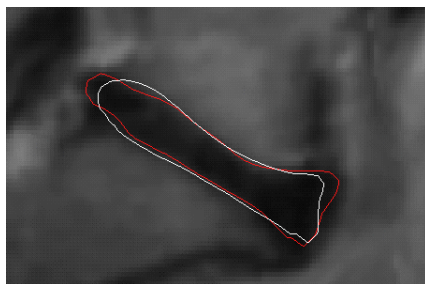
Figure 3.11: Segmentation result with two B-Spline relaxation steps (red contour) and without (white contour).

Notwithstanding, the employment of B-Spline to smooth the segmentation cannot overrule the SSM step, as it is demonstrated in the fourth experiment (fourth bar in Fig. 3.9). B-splines ensures highly detailed segmentation by allowing more flexibility in the deformations. However, without SSM, some segmentations leak into the neighbouring structures (Fig. 3.12) attaining lower accuracy in these cases. A segmentation was considered to have a leakage problem only when the size of the leakage was larger than the half of the height of a standard IVD. From visualisation, it was confirmed that non-accurate segmentations due to leaking problems were reduced around 7 times

by using the SSM. Therefore, the best performances were obtained by allowing small deformations with B-splines after the segmentation with the SSM converged.
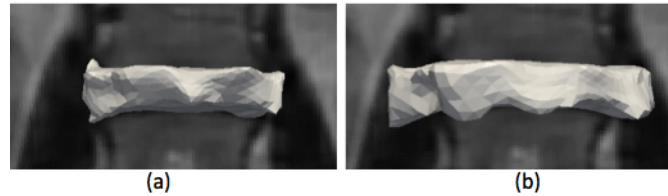
Figure 3.12: The use of the statistical model allows the method to properly recover the shape of the IVD (a). However, when it is not used the segmentation leaks to the muscle structure (b).

The last experiment presented in Section 3.4.2, was performed to evaluate the importance of the trained features. From the last bars in Fig. 3.9, it can be inferred that the use of these features has the main contribution to the high accuracy of the results. This conclusion is also evident in Table 3.3, since the magnitude of the reconstruction errors (Section 3.4.2) is similar to those obtained with the proposed method. As aforementioned, the large errors given by the Hausdorff distance were due to herniations, protrutions and other deformations, as well as less common shapes that were faded away in the trained SSM due to their low rate of occurrence.

A qualitative evaluation of the segmentation is presented in Fig. 3.10, which contains the sagittal and coronal views of three different patients with different types of degenerations and shapes. This figure also shows the nucleus segmentation, whose quantitative evaluation is presented in Table 3.2. This table presents the results using the complete framework, where it may be observed lower accuracy than in the case of the annulus, mainly due to the intensity variability and difficulty to find the borders of the nucleus. Notwithstanding, the results are proved to be accurate, since the inter-observer variability (Table 3.4) is close in magnitude to the results obtained using the automatic method. In the case of the annulus, the segmentation error was lower than the inter-observer variability.

Furthermore, the evaluation of the threshold selection for the nucleus existence (Section 3.2.6) is compared with the inter-observer variability of 3 experts. The gold standard was selected to be the most voted value (exist or not) for each nucleus and

this was compared with the three experts' evaluation as well as the automatic method (Table 3.5).

If the image resolution is considered, the performance of the proposed method is higher than those in the literature [145–147, 149]. However, the database employed by [146] contains patients with scoliosis, and therefore, it is more difficult to achieve high accuracy. On the contrary, [145] used only healthy subjects for the experiments, thus did not tackle IVD deformities. This information is summarised in Table 3.6.

Table 3.6: Comparison with state-of-the-art methods. Healthy and unhealthy represents a database with cases of all degeneration grades.

Authors	Error Measures		Type of	Image
	DSI	MASD	database	resolution(mm^3)
Chevrefils *et al.* [146]	77%	-	Scoliotic	$1 \times 1 \times 1$
Neubert *et al.* [145]	89%	0.55 mm	Healthy	$0.34 \times 0.34 \times 1$
Chen *et al.* [149]	86%	1.3 mm	Healthy and unhealthy	$1.25 \times 1.25 \times 2$
Haq *et al.* [147]	-	0.61 mm	Healthy and unhealthy	$0.5 \times 0.5 \times 0.9$
Proposed Method	88%	0.68 mm	Healthy and unhealthy	$0.68 \times 0.68 \times 4$

3.5.1 Limitations

One limitation of the presented method is the need of manual intervention for selecting the centre of the IVDs in the mid-sagittal view. To overcome this problem, any automatic IVD centre detection algorithm may be used [27, 28, 161, 162].

Another important limitation of the proposed method when used in multi-object structures such as vertebrae is that each object has its own SSM. Thus, when these objects are too close to each other overlaps may occur. Furthermore, the shape information that each object contains about its neighbours is lost with the current strategy. All these issues are handled with the framework that is presented in Chapter 4.

3.6 Conclusions and Future Work

This chapter focuses on the segmentation of 3D intervertebral discs in T2-weighted MR images, which is the best modality for visualizing IVDs. However, the segmentation method may be applied to any other type of object. The method starts by merging

coronal and sagittal MR acquisitions to achieve a dense volume, three trained features
and a statistical model were used for the segmentation stage and then, a relaxation step
based on B-splines was applied. It was evidenced that the use of trained features pro-
vides the highest increase of accuracy among all the components of this method with
respect to the standard ASM. On the contrary, the segmentation of volumetric data ob-
tained via multi-view fusion introduced little improvement compared to only sagittal
view. However, it is important to employ fusion to improve the image quality for man-
ual segmentation, based on which the SSM was built. This statistical model contains
the relationship between different parts of the IVDs and therefore, it was key to reduc-
ing the chance of the mesh leaking into neighbouring structures, but at the cost of a loss
in accuracy. This last drawback was overcome with the relaxation step, which allows
uncommon shapes, such as protrusions, or rare bumps, to be segmented. In the over-
all, this method is ready to be used in a clinical environment to create patient-specific
models for any type of medical applications.

Several lines of research may be followed to further improve this method. First, the
addition of new features, which could be trained with the same procedure introduced in
Section 3.2.4. The second area of research is the extension to a multi-object approach
in order to take into account the relationship between objects, since the shape and
pose of the different IVDs are correlated. A novel framework that follows this idea
is presented in the following chapter (Chapter 4). Finally, if the inter-slice spacing is
really large, one could resource to SSM fitting strategies, as that presented in [121],
that deals with sparse data. Unfortunately, since the material content of the IVDs is
related to the intensity of the MR images, this line of research will not be followed
along this thesis.

Chapter 4

Statistical Interspace Model (SIM) and its application to articulated 3D Spine Segmentation from CT data enforcing correct spinal geometry

In the previous chapter (Chapter 3) was introduced a segmentation framework that follows the strategy of ASM. The method modifies the standard intensity model, used to warp the mesh, for a feature-based searching technique. This method also includes a relaxation step to allow shapes to be outside the SSM variational space. Although it is a generic framework that provides accurate vertebra segmentation [130], the results did not fulfil all the properties required to be used in biomechanical simulations. The main issues were overlaps between vertebral processes and excessive separation between IVDs and vertebrae, which are translated into unrealistic geometries. In this chapter, a new segmentation framework is introduced to solve these issues. The proposed method is based on combining the shape information encoded in the SSM and a newly proposed Statistical Interspace Models (SIM). The latter includes the knowledge about the space between objects, interconnecting pairs of vertebrae.

In terms of solving drawbacks of the ASM, the proposed framework studies the use of SSM as an energy, so that shapes are not forced to remain in the SSM space. This

results in more flexibility in the segmentation that compensates for a low number of training cases. In addition, this framework allows pathological cases to be accurately segmented with SSMs trained with healthy cases.

This chapter was adapted from the publication of the author of this thesis *et al.* [109].

4.1   Motivation

Statistical Shape Models (SSM) [32] are commonly employed to extract the shape characteristics of a certain population. However, the direct use of such models to characterise multi-object or complex structures requires a large training dataset to properly represent new cases. The reason is that not only the shape of each individual substructure must be modelled, but also the relative positions and orientations among all of them. A possible solution is to use an individual SSM per object. However, this strategy ignores the inter-relationships between them, which can involve both shape and pose, especially for the neighbour structures. This problem may be solved by the use of conditional or hierarchical models [93, 163] that contain information about the shape inter-relationship between objects. However, these approaches do not specifically model the variability of the regions and relative positions between near-contact structures in neighbour objects. This is reflected by the appearance of:

- Overlaps.

- Excessive separation of neighbouring structures.

- Unrealistic orientations between neighbouring objects.

To solve these issues, this chapter introduces a new statistical model coined statistical interspace model (SIM), introduced in Section 4.4, embedded into a new segmentation framework, Section 4.5. SIM directly addresses the neighboring relationship between regions in different objects (or even in the same) of a multi-object structure by learning the statistical distribution of the interspace between them. SIM completely avoids overlaps, and imposes soft constrains on the acceptable poses and shapes.

This model may be applied in different applications concerning segmentation, registration, reconstruction, etc. For example, it may be employed to model the interspace between the two hemisphere of the brain, to restrain the separation between articulated bones, to control the relative position of the annulus and the nucleus of the Intervertebral discs (IVDs) or to maintain under control the separation between the two lungs to achieve realistic configurations, among possible applications.

As proof of concept, the proposed framework was tested on vertebra segmentation, since they are complex bodies (Fig. 4.1) that form a multi-object structure when combined to constitute the vertebral column. The aim is not only to provide high accurate segmentations but also to handle the problem of inter-process or vertebral body overlap (Fig. 4.2) as well as to avert unrealistic configurations. This issue is important for a range of application such as patient-specific biomechanical modeling [164, 165] or computer-assisted spine surgery [166]. For biomechanical models the correct definition of the processes and its correct geometry are essentials to perform realistic simulations; even high accurate segmentation will not be acceptable, if they have overlaps. In spinal fusion surgery, the correct delineation of processes and correct definition of the interspace between them is crucial for the precise placement of the screws.

The remaining of the chapter is structured as followed. Section 4.2 aims at providing a literature review of methods that employ overlap control or could be used for this purpose. Section 4.3 introduces the type of shape parameterisations that will be used along this chapter. These shapes will have an important role in each of the energies that will be used in the segmentation framework (Section 4.5). The SIM is introduced in Section 4.4, where its construction procedure is depicted. The results of the method applied in the segmentation of vertebrae is presented in Section 4.7. The last two sections are the Discussion and conclusions of the method applied to vertebra segmentation.

4.2 Background

4.2.1 Zero Overlap Segmentation Methods

Overlap between objects may be avoided by the use of multi-label strategy classification, where each image pixel or voxel only has one value [167, 168]. These methods, however, do not necessarily employ the information of the relative position between objects and therefore, the vertebral inter-process space might be wrongly segmented.

Another general methodology that produces zero overlap segmentations is labels propagation methods [19, 169], which performs the segmentation by warping a previously segmented image (source) into the space of the to-be-segmented image (target). This approach is generally employed with several sources and the results are combined to increase the accuracy. However, small regions such as the inter-process vertebral space might be ruled out in an image-to-image registration and a special treatment must be employed. In addition, these methods are usually computationally expensive. The same issues may be applied to level set segmentation frameworks [18, 170].

4.2.2 Vertebra Segmentation Methods

The segmentation of vertebrae is an important first stage for many applications as previously explained. Thus, there is a vast literature of segmentation from X-rays and Dual-energy X-ray Absorptiometry (DXA) images [42, 63, 87, 90, 93, 94, 171], from CT images [105, 170, 172–180], and from MR images [145, 181, 182]. However, this section focuses on the methods that directly or indirectly address the vertebral overlap.

Shen *et al.* [183] proposed a method to avert vertebrae from leaking to other structures using information extracted from detected planes between vertebrae. This information was included in a level-set framework. Kim *et al.* [184] employed a 3D fence to create a wall between the articular processes of the vertebrae in order to be able to segment a vertebra using region growing. These two methods reduce the overlap between vertebrae by estimating the separation between them. However, they do not employ any prior information based on the training population, which could greatly improve the performance.
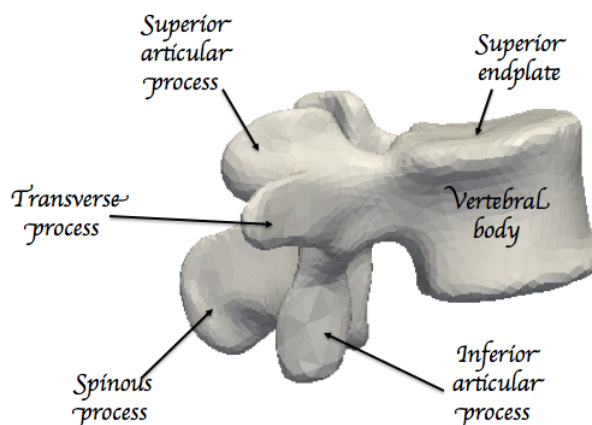
Figure 4.1: Anatomy of a human vertebra.

Prior information to avoid vertebral intersection may be acquired by constructing an SSM of the full spine as a single object. However, as mentioned earlier this model would require a large training dataset to achieve sufficient degrees of freedom. Although, it is possible the addition of relaxation steps, based on Active Contour Models [42] or Free Form Deformations [46], the segmentation will commonly leak into neighboring structures or will be deformed more than required when the best fit of the SSM do not closely resemble the real shape.

A more elegant solution was proposed by Kindler *et al.* [185]. They designed a vertebral segmentation algorithm based on a statistical pose model (SPM) of the spine, following the work of Boisvert *et al.* [186]. In this framework, shapes are deformed by minimising an energy based on the image gradient and penalised by the distance to the pose given by the SPM. Since, inter-process overlap is reduced but not completely avoided, the authors added a new energy term that penalises the overlap between vertebrae. However, it still does not prevent them completely. The author of this thesis' assumption is that in doing so the accuracy would decrease due to the SPM excessively restricting the possible outcomes. An analogous strategy to avoid overlaps and maintain under control the distance between structures was proposed in [187]. The approach was based on a modified spring energy employed in a mesh-to-mesh registration framework tested on wrist bones. A similar approach as using the SPM was proposed by Kadoury *et al.* [188], in which the relationship between the individual
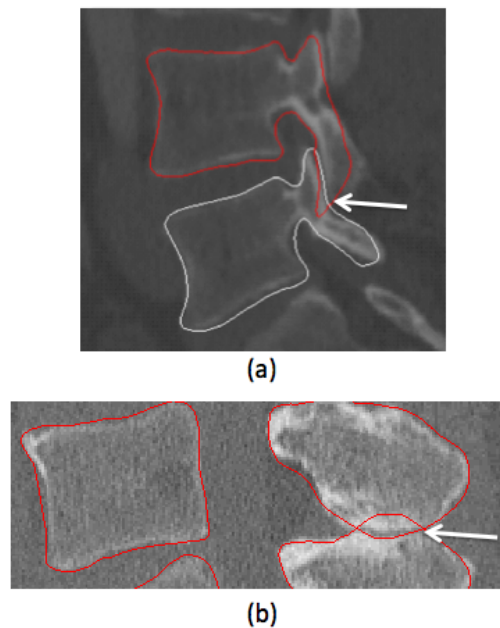
Figure 4.2: The overlap in the vertebral process is a common problem in vertebral segmentation, mainly in the articular processes (a) where the separation is rather small but it can also happen in the spinous process as shown in (b).

shape variations are correlated to the global deformations with a series of rigid transformations and embedded into a Markov random field segmentation framework.

In [189] a model of the full spine was employed. However, the relative rotations and translations given by the spine articulated movements were removed and a SPM was trained for that purpose. Even though, this approach still requires a larger training dataset. This method was extended to MR images [190].

In an earlier work [130], the author of this thesis *et al.* proposed a segmentation strategy for vertebral segmentation. The process employs an Active Shape Model approach [32], with a novel set of trained features for the shape to image adaptation step to partially address the overlap problem.

A multilabel strategy for vertebra segmentation was proposed by Forsberg [191]. As explained before, this technique does not allow overlaps, but has other issues. In order to avoid the processes leaking to to the ribs, and to eliminate wrong rotations and distance between vertebral bodies, the method initialises the position based on detecting the IVD and the spinal cord. Nevertheless, this method does not handle the

issue of two processes collapsing to each other.

4.3 Parameterisation of the Shapes

4.3.1 Point Correspondence

The point correspondence represents the idea that shapes are described by the same number of landmarks, s_p, $p = 1, \ldots, P$, and those landmarks are located in the same anatomical position.

The complete set of points concatenated in a $3 \times P$ matrix will be denoted as S, assuming 3D shapes.

This concept is essential to build SSMs and SIMs. In this work, the point correspondence was achieved by an iterative registration approach, based on B-splines.

This procedure began deforming a template mesh to all the shape meshes of the training set. Thereafter, the mean shape at each spinal position was computed. Subsequently, the template mesh was changed by the mean shape and the process was iteratively repeated until the convergence of the means. The template mesh was created by smoothing and decimating a selected L3 vertebra and the ground-truth meshes were obtained using Marching cubes [192] in the binary masks achieved through manual segmentation.

4.3.2 Unconstrained Shape Instance

An unconstrained shape instance is created by the independent displacement of the landmarks that represents the shape. In the proposed segmentation framework, this type of shape instance is used only for the fitting to the image (S^{I}), analogously to the usual ASM segmentation [32] (Section 4.5.3).

4.3.3 Constrained Shape Instance by the Use of Statistical Shape Models (SSM)

An SSM describes the variability of a shape within a selected population. In general, apart from the point correspondence, the pose and scale of the cases are removed by aligning them to a reference shape with a similarity transformation. This normalisation

is performed by generalised Procrustes alignment, which generates the mean shape, $\overline{\boldsymbol{S}}$, simultaneously with the aligned shapes.

Each aligned shape may be considered as being a sample from a $3P$ probability density function (pdf). Assuming this pdf takes the form of a Gaussian distribution [32], Principal Component Analysis (PCA) can be used to attain the main axes of the cloud of points. The SSM represents new shapes by the mean, $\overline{\boldsymbol{S}}$, and a linear combination of a set of orthonormal principal components (PC), $\boldsymbol{\Phi}_m, m = 1, \ldots, M$.

$$\hat{\boldsymbol{S}}^{\text{SSM}} = \overline{\boldsymbol{S}} + \sum_{m=1}^{M} b_m \boldsymbol{\Phi}_m \tag{4.1}$$

where the coefficients b_m are called the *SSM parameters* and the relative influence of each PC is given by its corresponding standard deviations, σ_m. In addition, the b_m parameters are limited to 3 times σ_m,

$$-3\sigma_m \leq b_m \leq 3\sigma_m, \qquad \forall m = 1, \ldots, M.$$

New instances, including pose and scaling, may be attained by applying a similarity transformation to the shape $\hat{\boldsymbol{S}}^{\text{SSM}}$:

$$\boldsymbol{S}^{\text{SSM}} = a\boldsymbol{R}\hat{\boldsymbol{S}}^{\text{SSM}} + \boldsymbol{c}. \tag{4.2}$$

Thus, the instance is a function of the SSM parameters, b_m, a scaling factor, a, a translation vector $\boldsymbol{c}$, and a rotation matrix, $\boldsymbol{R}$.

For multiple objects, each with an individual SSM and similarity transformation, the model is:

$$\hat{\boldsymbol{S}}_v^{\text{SSM}} = \overline{\boldsymbol{S}}_v + \sum_{m=1}^{M} b_{v,m} \boldsymbol{\Phi}_{v,m} \qquad \text{and} \qquad \boldsymbol{S}_v^{\text{SSM}} = a_v \boldsymbol{R}_v \hat{\boldsymbol{S}}_v^{\text{SSM}} + \boldsymbol{c}_v, \tag{4.3}$$

where the index v runs along the set of objects, $v = 1, \ldots, V$.

4.3.4   Constrained Shape Instance by the Use of B-splines

In addition to the previous instances, it was also considered, $\boldsymbol{S}_v^{\mathrm{B}}$, which are given by smooth B-spline transformation from any chosen reference shape, $\boldsymbol{S}_v^0$, parameterised by displacements, $\boldsymbol{z}_{v,f}$, at a grid of control points, $f = 1, \ldots, F$. Each point in $\boldsymbol{S}_v^{\mathrm{B}}$ is then located at

$$\boldsymbol{s}_{v,p}^{\mathrm{B}} = \boldsymbol{s}_{v,p}^0 + \sum_{f=1}^{F} B_f\big(\boldsymbol{s}_{v,p}^0\big)\,\boldsymbol{z}_{v,f} \tag{4.4}$$

where the B_f are the B-spline weights.

The output of the segmentation will be a B-spline instance. The advantage of this type of shape instance is twofold. First, it allows more flexibility than that of the SSM. In fact, this additional flexibility is required for the incorporation of the SIM into the segmentation framework, otherwise the SIM would restrict a large region of the SSM parameters values as incompatible. Second, the use of a B-spline instance ensures smooth segmentations, in contrast with the unconstrained type, that would require an extra regularisation term [193].

4.4   Statistical Interspace Model (SIM)

For an articulated multi-object structure, individual SSMs together with an SPM provide a complete set of parameters to generate instances of this object. However, using only these two models does not prevent unrealistic configurations, including overlaps, excessive separation between objects or unnatural orientations of neigbouring substructures. In the spine, for example, this affects the vertebral processes, which can intersect between them. Thus, low signal or high noise within the image intensity may lead to incorrect segmentations including these artefacts.

A way to partially overcome these limitations is by the use of spring models, which are employed to maintain deformations under control by penalising large distance to a reference position. For instance, the approach of Klinder *et al.* [185] employs this type of model as part of the energy problem to handle vertebral overlaps.

However, the drawback of spring models for this purpose is twofold. First, they

cannot guarantee zero-overlap. In fact, the only reduce the amount of overlapped volume. Second, they do not model the statistical variation in size of the separation in the population.

An elegant solution to handle this limitation is to model the interspace between the objects. Therefore, the change in variation of an object O^1 affects the interspace between this object and its neighbour O^2, which produces O^2 to change in shape. In order to model the interspace between object it was employed the relative position vector between landmarks of neighbouring objects. Consider two points (o_d^1, o_d^2) from two different objects or from the same one. The relative position vector $\boldsymbol{\delta}_d$ is a vector that starts in o_d^1 and finishes in o_d^2.

Therefore, the first step to construct the SIM is to select the points $\boldsymbol{s}_d$ with $d = 1...D$ being an index running along all the points for which the SIM is going to be computed. In the mean shape, for each landmark $\boldsymbol{s}_d$, it is necessary to find the closest landmark that belongs to the object that is sharing the interspace with. These pair of landmark connections are propagated across all the training set and the relative position vector between them are employed for the SIM construction.

4.4.1   Individual Point Reference Frame

The computation of $\boldsymbol{\delta}_d$ requires a reference frame $(\hat{\boldsymbol{g}}_d^1, \hat{\boldsymbol{g}}_d^2, \hat{\boldsymbol{g}}_d^3)$ that is irrespective to the object shape and pose (Fig. 4.3). The reason for this is to measure vectors that go from one landmark to another and not only their magnitude.

In this work, it is proposed for $\hat{\boldsymbol{g}}_d^3$ to be the normal vector of the object surface at point $\boldsymbol{s}_d$. For all cases, an edge is selected in the triangular mesh from $\boldsymbol{s}_d$ to a neighbour point, defining the vector $\boldsymbol{t}$. The second vector is obtained by projecting $\boldsymbol{t}$ in the perpendicular plane given by $\hat{\boldsymbol{g}}_d^3$:

$$\boldsymbol{g}_d^2 = \boldsymbol{t} - (\boldsymbol{t} \cdot \hat{\boldsymbol{g}}_d^3)\hat{\boldsymbol{g}}_d^3 \,, \qquad \hat{\boldsymbol{g}}_d^2 = \frac{\boldsymbol{g}_d^2}{\|\boldsymbol{g}_d^2\|} \tag{4.5}$$

And $\hat{\boldsymbol{g}}_d^1$ is their cross product $\hat{\boldsymbol{g}}_d^1 = \hat{\boldsymbol{g}}_d^2 \times \hat{\boldsymbol{g}}_d^3$.

Having the reference frame $(\hat{\boldsymbol{g}}_d^1, \hat{\boldsymbol{g}}_d^2, \hat{\boldsymbol{g}}_d^3)$ allows us to define the relative position

vector between the different pair of points, in a coherent way among all the sample cases. Thus, the local frame provides local relative position correspondence, analogous to the point correspondence required for the landmarks in the SSM.
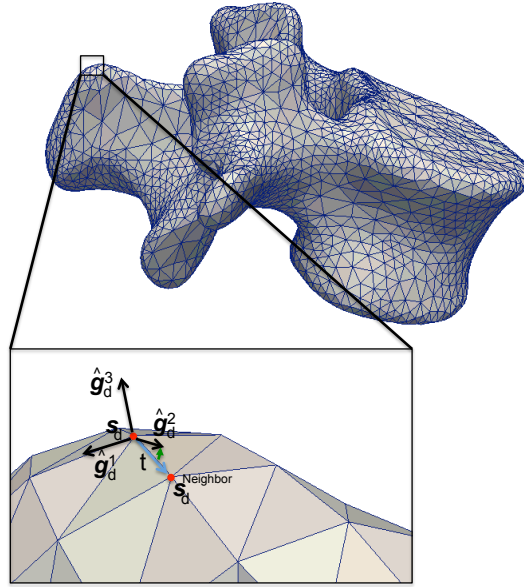
Figure 4.3: Description of the local reference system for the point s_d. The vector t goes from s_d to a previously selected neighbor ($s_d^{\text{Neighbour}}$). The vector $\hat{g}_d^3$ is the normal of the object surface at point s_d, whereas $\hat{g}_d^2$ is obtained by projecting t onto the surface tangent plane perpendicularly to $\hat{g}_d^3$. Finally, $\hat{g}_d^1$ is the cross product of $\hat{g}_d^2$ and $\hat{g}_d^3$.

4.4.2 Separation Between Magnitude and Directional Vector

Having computed the relative position vector $\boldsymbol{\delta}_d$ for each landmark s_d in the SIM, a statistical interspace model might be created in the same fashion as the standard SSM. However, this approach would assume a Gaussian distribution (linear approach) on the relative position vectors of x, y and z. Since, a Gaussian shape is symmetric with respect to its mean position, the consequence of this assumption is that negative distances are allowed, which results in the overlaps and other unrealistic geometries.

Thus, it is necessary to find a non-linear representation that properly models $\boldsymbol{\delta_d}$. Since, the aim is to control the magnitude and orientation of $\boldsymbol{\delta_d}$, a proper representation was the separation of $\boldsymbol{\delta_d}$ into its magnitude γ_d and a unit vector $\boldsymbol{\omega}_d$ that represents the orientation.

$$\boldsymbol{\delta}_d = \gamma_d \boldsymbol{\omega}_d \tag{4.6}$$

This separation maps $\mathbb{R}^3 \to \mathbb{R}^+ \otimes S^2$. Thus, both factors $\mathbb{R}^+$ and S^2 are manifolds.

In particular, R^+ is a Lie group for the real product, which endows it with a natural Riemannian geometry. Therefore, the tangent space of the magnitude is the natural logarithm of real positive numbers. The implication of using such model in an energy-driven segmentation is that the gap between the objects cannot be zero. Thus, two landmarks from different objects cannot share the same position. However, two objects could touch each other or even have an overlap with only this energy, which represents the logarithm of the distance between the points. This energy tries to maintain the points close to any position in the surface of a sphere with radius equal to the mean distance between the landmarks that were used for training the model.

The directional vector was modelled as the space S^2, which can be seen as a unitary sphere when embedded into a Euclidean space. In this case, the tangent space used for computing all the measurements, was selected as the tangent space at the centre position of the training samples in S^2. This implies that it was considered the arc-lengths from each training sample to the mean vector, to belong to a Gaussian distribution. The addition of this model ensures that each pair of points is closely aligned to the direction given by the mean vector. However, this energy does not guaranteed a zero overlap in the segmentation process, since it measures the arc-length between two points in S^2, whose maximum value is π. Notwithstanding, an overlap implies rotations close to π degrees which will increase the energy substantially. Although, it was not found any overlap in the experiments, a solution to a possible one is employing the same idea as in Active Shape Model (ASM) [32], where deformations were restricted to a maximum of $\pm 3 \times$ the standard deviation, in their case given by the eigenvalues. Another solution, is to extend the values so that π represents the infinity.

The separation between magnitude and unitary vector was tested by different Gaussianity tests. To prove that magnitude samples lie in a log-gaussian distribution, the "Lilliefors' composite goodness-of-fit test" [194] and the "Jarque-Bera hypothesis test of composite normality" [195] were employed using as input the logarithm of the dis-

tances. Both of them could not reject the null hypothesis of the data being normally distributed at the 5% significance level. In the case of the unitary vector, it is assumed that the data in the tangent space at the mean position behaves as Gaussian. Since, this is a 2-dimensional distribution, the same tests were not available. Thus, it was employed the test "Henze-Zirkler's Multivariate Normality Test" [196], which could not reject the null hypothesis of the data being normally distributed at the 5% significance level.

Observe that SIM is not a generative model, meaning it cannot create an instance of the objects by itself. However, when it is employed with an SSM (or SSM and SPM) prevents impossible configurations and geometries in the instances.

4.4.3 Mean and Covariance Computations

In order to model the interspace between objects, the following four statistics are required: The mean of ω in S^2 ($\overline{\omega}_d$), the covariance matrix of ω in $T_{\overline{\omega}}(S^2)$ ($\boldsymbol{C}_d$), the mean magnitude ($\overline{\gamma}_d$) and the variance of the magnitude l_d.

In order to compute the mean and covariance in a non-euclidean manifold, it was adopted the methodology proposed by Fletcher *et al.* [197] to compute the Principal Geodesic Analysis (PGA). Their method assumes that the tangent space at the mean position of all the samples (μ) behaves as an Euclidean space. In this proposed method, the mentioned samples are going to be the individual magnitude (γ) and the individual directional vectors ($\boldsymbol{\omega}$) of each $\boldsymbol{\delta}_d$. Thus, $\mu = \{\overline{\omega}, \overline{\gamma}\}$ and it is defined as:

$$\mu = \operatorname*{argmin}_{u} \sum_{q} D(u_v, u)^2 \tag{4.7}$$

where D denotes the geodesic distance between two points in the manifold. The subindex v runs along the different cases in the dataset. In this context, u would be either γ_d or $\boldsymbol{\omega}_d$.

The intrinsic mean (μ) was computed following the approach proposed by Fletcher *et al.* [197]. The process begins by selecting a random sample as the mean (μ) and projecting all the samples to the tangent space at this point ($T_\mu(M)$). In this space the

mean of the projected samples (κ) is computed and transformed back to S^2 ($Exp_\mu(\kappa)$) to obtain the new μ. This process is repeated until convergence.

Since the magnitude belongs to the Lie group $\mathbb{R}^+$, the distance function is defined as:

$$D(\gamma_d^1, \gamma_d^2) = \log\frac{\gamma_d^1}{\gamma_d^2} \tag{4.8}$$

However, since this is a 1-dimensional problem, $\overline{\gamma}$ and l_d can be analytically computed as the standard mean and variance of all the log-magnitudes [198].

For two directions, the geodesic distance in S^2 is given by the arc length between them:

$$D(\boldsymbol{\omega}_d^1, \boldsymbol{\omega}_d^2) = \mathrm{acos}(\boldsymbol{\omega}_d^1 \cdot \boldsymbol{\omega}_d^2) \tag{4.9}$$

where $\boldsymbol{\omega}_d^1 \cdot \boldsymbol{\omega}_d^2$ is the dot product of $\boldsymbol{\omega}_d^1$ and $\boldsymbol{\omega}_d^2$.

For the sphere S^2, it is necessary to define the manifold logarithm that projects a sample in S^2 into the tangent space, $T_{\overline{\omega}}S^2$. This operation requires two orthonormal vectors ($\hat{\boldsymbol{h}}^1, \hat{\boldsymbol{h}}^2$) to $\overline{\omega}$. Their orientation in the tangent plane is irrelevant, but they need to be consistent across the training dataset. The reference frame ($\hat{\boldsymbol{h}}^1, \hat{\boldsymbol{h}}^2, \hat{\boldsymbol{h}}^3$) is then defined as the frame that results after rotating ($\hat{\boldsymbol{g}}^1, \hat{\boldsymbol{g}}^2, \hat{\boldsymbol{g}}^3$) so that $\hat{\boldsymbol{h}}^3$ coincides with $\overline{\omega}$. The logarithm is then given by:

$$\mathrm{Log}_{\overline{\omega}}(\hat{\boldsymbol{q}}) = \left(\hat{\boldsymbol{q}} \cdot \hat{\boldsymbol{h}}^1 \frac{\alpha}{\sin(\alpha)}, \hat{\boldsymbol{q}} \cdot \hat{\boldsymbol{h}}^2 \frac{\alpha}{\sin(\alpha)} \right) \tag{4.10}$$
$$\text{with} \qquad \alpha = \mathrm{acos}(\hat{\boldsymbol{q}} \cdot \overline{\omega})$$

Observe that by identifying $T_{\overline{\omega}}S^2$ as the tangent plane to S^2 embedded in R^3, the output of the logarithm is the projection of $\hat{\boldsymbol{q}}$ into $T_{\overline{\omega}}S^2$ rescaled so that its length is equal to α (Fig. 4.4).

Once each sample point in S^2 has been identified with its logarithm in the tangent space, the usual sample covariance matrix can be computed as that of an Euclidean space.
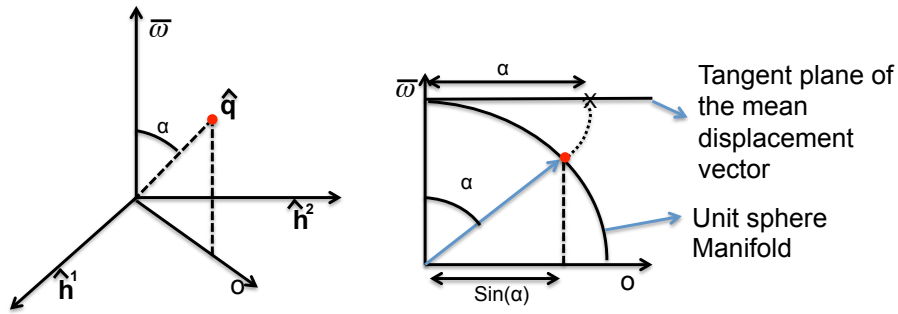
Figure 4.4: Description of the projection of a point $\hat{q}$ that belongs to the S^2 manifold to $T_{\overline{\omega}}(S^2)$. The plane defined by the vectors $\hat{h}^1$ and $\hat{h}^2$ is parallel to $T_{\overline{\omega}}(S^2)$. Then, $\text{Log}_{\overline{\omega}}(\hat{q})$ is the orthogonal projection of $\hat{q}$ to $T_{\overline{\omega}}(S^2)$, rescaled to have the angle α as length, instead of $\sin \alpha$.

4.5 Segmentation Framework

4.5.1 Initialisation

As commonly required in segmentation procedures, the proposed framework needs a rough initialisation of the shape in the image. For a multi-object structure, this may be performed by locating each individual object independently or with some constrains. For the application to vertebral segmentation, it was applied the same initialisation method as in [130]. The mean shape of each vertebra, $\overline{S}_v$, is individually aligned to the image by means of a similarity transformation. This transformation is based on the approximate intervertebral discs (IVD) centre points that were manually pinpointed in the image.

During the training step, the upper and lower endplate middle landmarks, of the mean meshes at each vertebral position, were selected. These two points were employed to calculate the centre of the vertebral body (VB), c^1 and the directional vector from the lower to the upper endplate, u^1, of each initial vertebra.

In the segmentation phase, the IVD centres in the image were manually selected. These points define the centre of the VB, c^2, in the image and a new vector that goes from the lower IVD to the upper one in each vertebra u^2. Then, a translation vector is given by the difference between c^2 and c^1, the scaling factor (e) is given by a scaled

ratio of the magnitudes of $\boldsymbol{u}^2$ and $\boldsymbol{u}^1$ and the rotation matrix ($\boldsymbol{R}^{\text{o}}$) was computed using the Rodrigues' rotation formula [186]:

$$e = k\frac{\|\boldsymbol{u}^2\|}{\|\boldsymbol{u}^1\|} \tag{4.11}$$

$$\boldsymbol{R}^{\text{o}} = \boldsymbol{U} + \boldsymbol{B} + \frac{\boldsymbol{B}\boldsymbol{B}}{1 + \hat{\boldsymbol{u}}^1 \cdot \hat{\boldsymbol{u}}^2} \text{ and } \boldsymbol{B} = \hat{\boldsymbol{u}}^1\hat{\boldsymbol{u}}^{2,T} - \hat{\boldsymbol{u}}^2\hat{\boldsymbol{u}}^{1,T} \tag{4.12}$$

where U is the identity matrix and the scaling factor k ($k = 0.9$) was used to compensate the difference between the real height of the VB and the distance between two consecutive IVD centres.

4.5.2   Statistical Shape Model Energy

The statistical shape model energy is commonly expressed as the squared Euclidean distance between the closest shape that can be represented with the SSM, $\boldsymbol{S}^{\text{SSM}}$, and the segmentation result, in this case $\boldsymbol{S}^{\text{B}}$.

$$E^{\text{SSM}}(\boldsymbol{S}^{\text{B}}, \boldsymbol{S}^{\text{SSM}}) = \frac{1}{2}\sum_{v,p} \|\boldsymbol{s}_{v,p}^{\text{B}} - \boldsymbol{s}_{v,p}^{\text{SSM}}\|^2 \tag{4.13}$$

where the squared distance is summed up for all points and objects.

4.5.3   Image Energy

The image energy is computed for each landmark independently following same strategy as explained in the previous chapter (Chapter 3.2.4). Thus, the resultant shape $\boldsymbol{S}^{\text{I}}$ is an unconstrained shape instance (Section 4.3.2). This image energy is based on the oriented derivative from high to low intensity and the intensity itself, whose parameters were obtained using the training database, explained in Section 4.6. Thus, the energy function for these features is:

$$\text{E}_{v,p}^{\text{I}}(\boldsymbol{S}^{\text{I}}, \text{I}) = (w^1 I(\boldsymbol{s}_{v,p}^{\text{I}}) + w^2(\hat{\boldsymbol{n}} \cdot \nabla I(\boldsymbol{s}_{v,p}^{\text{I}}))) \tag{4.14}$$

where $\hat{\boldsymbol{n}}$ is the normal direction at point $\boldsymbol{s}_{v,p}^{\text{B}}$ from inside to outside the mesh, I is

the image intensity.

The image energy has a second component that relates the result segmentation shape S^{B} and S^{I}:

$$E^{\mathrm{I\text{-}B}}(S^{\mathrm{B}}, S^{\mathrm{I}}) = \frac{1}{2} \sum_{v,p} \| s^{\mathrm{B}}_{v,p} - s^{\mathrm{I}}_{v,p} \|^2 \tag{4.15}$$

4.5.4   Statistical Interspace Model Energy

Having computed the SIM model for a group of objects means that for each relative position vector $\boldsymbol{\delta}_d$ there exist a $\overline{\gamma}_d$, l_d, $\overline{\boldsymbol{\omega}}_d$ and C_d (Section 4.4). Hence, the energy of a new $\boldsymbol{\delta}_d$ is achieved by:

$$E^{\mathrm{SIM}} = \frac{P}{2D} \sum_d \boldsymbol{\epsilon}_d C_d^{-1} \boldsymbol{\epsilon}_d^T + \log\left(\frac{\gamma_d}{\overline{\gamma}_d}\right)^2 l_d^{-1} \tag{4.16}$$

$$\text{with} \quad \boldsymbol{\delta}_d = \gamma_d \boldsymbol{\omega}_d \quad \text{and} \quad \boldsymbol{\epsilon}_d = \mathrm{Log}_{\overline{\boldsymbol{\omega}}}(\boldsymbol{\omega}_d)$$

The coefficient $\frac{P}{2D}$ is used to compensate the difference in the number of points between E^{SIM} and the rest of energies. The value P is the total number of landmarks in the whole structure and D is the number of relative position vectors (pair of points) in the structure that employs the SIM.

4.5.5   Segmentation Problem

The segmentation algorithm is based on minimising a linear combination of the previously presented energies:

$$S^{\mathrm{B}} = \operatorname*{argmin}_{S^{\mathrm{B}}} \min_{S^{\mathrm{I}}, S^{\mathrm{SSM}}} E(S^{\mathrm{B}}, S^{\mathrm{I}}, S^{\mathrm{SSM}}, I) \quad \text{where} \tag{4.17}$$

$$E(S^{\mathrm{B}}, I, S^{\mathrm{I}}, S^{\mathrm{SSM}}) = E^{\mathrm{I}}(S^{\mathrm{I}}, I) + w^{\mathrm{B\text{-}I}} E^{\mathrm{B\text{-}I}}(S^{\mathrm{B}}, S^{\mathrm{I}}) \tag{4.18}$$

$$+ w^{\mathrm{SSM}} E^{\mathrm{SSM}}(S^{\mathrm{B}}, S^{\mathrm{SSM}}) + w^{\mathrm{SIM}} E^{\mathrm{SIM}}(S^{\mathrm{B}})$$

Each of the shapes represents an instance of all the objects that composed the multi-object structure. I denotes the image to be segmented, which is a constant for the energy minimisation. S^{B} is the output segmentation, whereas S^{I} and S^{SSM} are auxiliary

shapes. Nevertheless, all three shapes must be optimised to minimise the energy, even though only S^{B} is of interest.

4.5.6   Optimisation

In order to solve the aforementioned problem, it is proposed an alternating optimisation technique, where each of the three shapes involved S^{B}, S^{I}, and S^{SSM} are iteratively optimised in turns.

Shape Initialisation

The mean shape of each object, $\overline{S}_v$, is scaled, translated and rotated (similarity transformation) according to some strategy (Section 4.5.1), attaining S_0. This provides the initialisation for the three shapes: $S^{\mathrm{I}} = S^{\mathrm{B}} = S^{\mathrm{SSM}} = S_0$.

Alternating Optimisation

Having initialised the three shapes, they are optimised as follows:

1. Only two energies involve S^{I}. Thus, this optimisation only needs to minimise the terms

$$E^{\mathrm{I}}(S^{\mathrm{I}}, I) + E^{\mathrm{B\text{-}I}}(S^{\mathrm{B}}, S^{\mathrm{I}}), \qquad (4.19)$$

   since the others are constant. This optimisation is performed at each landmark independently, following the typical strategy used in ASM. Observe that because the optimisation is alternating between shapes, at each iteration the shape S^{I} is obtained by displacing the landmarks of the S^{B} from the previous step and not the previous S^{I}.

2. **Optimisation of S^{SSM}.** The only term involving S^{SSM} is

$$E^{\mathrm{SSM}}(S^{\mathrm{B}}, S^{\mathrm{SSM}}) \qquad (4.20)$$

   The shape S^{SSM} contains two type of parameters: the similarity transformation of the shape and the SSM parameters for the PCs. These two sets are optimised also

alternating:

(a) **Exact optimisation of similarity transformation.** Fixing the SSM parameters allows the optimisation of the similarity transformation by a single algebraic operation using Procrustes.

(b) **Exact optimisation of the SSM parameters.** Fixing the similarity transformation allows E^{SSM} to be optimised in the SSM parameters by projecting the shape into the PC basis.

These two operations can be repeated several times until convergence of the full $\boldsymbol{S}^{\text{SSM}}$ optimisation.

3. **Gradient descent step for the shape $\boldsymbol{S}^{\text{B}}$.** This shape involves three terms of the energy:

$$w^{\text{I-B}} E^{\text{I-B}}(\boldsymbol{S}^{\text{B}}, \boldsymbol{S}^{\text{I}}) + w^{\text{SSM}} E^{\text{SSM}}(\boldsymbol{S}^{\text{B}}, \boldsymbol{S}^{\text{SSM}}) + w^{\text{SIM}} E^{\text{SIM}}(\boldsymbol{S}^{\text{B}}) \qquad (4.21)$$

The optimisation is achieved through a gradient step procedure. The number of iterations in the gradient step was reduced to a maximum of 5 iterations, since the full optimisation process is repeated iteratively until the convergence of the $\boldsymbol{S}^{\text{B}}$.

The shape $\boldsymbol{S}^{\text{B}}$ is a linear function of the control point displacements, $\boldsymbol{z}_{v,f}$, as was shown in (4.4). The gradient involved in the optimisation of the energy with respect to $\boldsymbol{S}^{\text{B}}$ is given by the derivatives

$$\frac{\partial E}{\partial \boldsymbol{z}_{v,f}} = \sum_p \frac{\partial \boldsymbol{s}_{v,p}^{\text{B}}}{\partial \boldsymbol{z}_{v,f}} \cdot \frac{\partial E}{\partial \boldsymbol{s}_{v,p}^{\text{B}}} = \sum_p B_f(\boldsymbol{s}_{v,p}^0) \frac{\partial E}{\partial \boldsymbol{s}_{v,p}^{\text{B}}} \qquad (4.22)$$

where

$$\frac{\partial E}{\partial \boldsymbol{s}_{v,p}^{\text{B}}} = w^{\text{SSM}} \frac{\partial E^{\text{SSM}}}{\partial \boldsymbol{s}_{v,p}^{\text{B}}} + w^{\text{I-B}} \frac{\partial E^{\text{I-B}}}{\partial \boldsymbol{s}_{v,p}^{\text{B}}} + w^{\text{SIM}} \frac{\partial E^{\text{SIM}}}{\partial \boldsymbol{s}_{v,p}^{\text{B}}}. \qquad (4.23)$$

The derivatives of the first two energies are simply

$$\frac{\partial E^{\text{SSM}}}{\partial \boldsymbol{s}_{v,p}^{\text{B}}} = \boldsymbol{s}_{v,p}^{\text{B}} - \boldsymbol{s}_{v,p}^{\text{SSM}} \qquad \text{and} \qquad \frac{\partial E^{\text{I-B}}}{\partial \boldsymbol{s}_{v,p}^{\text{B}}} = \boldsymbol{s}_{v,p}^{\text{B}} - \boldsymbol{s}_{v,p}^{\text{I}}. \qquad (4.24)$$

The derivatives of the E^{SIM} are

$$\frac{\partial E^{\mathrm{SIM}}}{\partial \boldsymbol{s}_{v,p}^{\mathrm{B}}} = \sum_d \frac{\partial \boldsymbol{s}_{v,p}^{\mathrm{B}}}{\partial \boldsymbol{\delta}_d} \frac{\partial E^{\mathrm{SIM}}}{\partial \boldsymbol{\delta}_d} \tag{4.25}$$

where $\partial \boldsymbol{s}_{v,p}^{\mathrm{B}}/\partial \boldsymbol{\delta}_d$ is a signed selector, whose value is -1 if the landmark $\boldsymbol{s}_p$ is the origin of the relative position vector $\boldsymbol{\delta}_d$, +1 if it is the end of $\boldsymbol{\delta}_d$, and 0 if it is not contain in the SIM. The second factor can be computed from (4.16):

$$\begin{aligned}
\frac{\partial E^{\mathrm{SIM}}}{\partial \boldsymbol{\delta}_d} = \frac{P}{2D} \Bigg[& \left(\frac{\boldsymbol{I}}{\gamma_d} - \frac{\boldsymbol{\delta}_d^{\mathrm{T}} \boldsymbol{\delta}_d}{\gamma_d{}^3} \right) \boldsymbol{R}_d^{\mathrm{h}} \boldsymbol{R}_d^{\mathrm{g}} \frac{\partial \boldsymbol{\epsilon}_d}{\partial \hat{\boldsymbol{\omega}}_d} \boldsymbol{C}_d{}^{-1} \boldsymbol{\epsilon}_d{}^{\mathrm{T}} \\
& + \frac{\boldsymbol{\delta}_d}{\gamma_d{}^2} L_d{}^{-1} \log \frac{\gamma_d}{\bar{\gamma}_d} \Bigg]
\end{aligned} \tag{4.26}$$

where

$$\frac{\partial \boldsymbol{\epsilon}_d}{\partial \hat{\boldsymbol{\omega}}_d} = \frac{\alpha}{\sin \alpha} \begin{pmatrix} 1 & 0 \\ 0 & 1 \\ \beta \epsilon_{d,1} & \beta \epsilon_{d,2} \end{pmatrix} \quad \text{with} \quad \beta = \frac{\cos \alpha}{\alpha \sin \alpha} - \frac{1}{\alpha^2}, \tag{4.27}$$

and $\epsilon_{d,1}$, $\epsilon_{d,2}$ denote the components of $\boldsymbol{\epsilon}_d$. The rotation matrices $\boldsymbol{R}_d^{\mathrm{g}}$ and $\boldsymbol{R}_d^{\mathrm{h}}$, transform the world coordinate system to the individual reference system $(\hat{\boldsymbol{g}}^1, \hat{\boldsymbol{g}}^2, \hat{\boldsymbol{g}}^3)$, and from this reference frame to $(\hat{\boldsymbol{h}}^1, \hat{\boldsymbol{h}}^2, \hat{\boldsymbol{h}}^3)$, respectively (Section 4.4.3). Both matrices and both $(\hat{\boldsymbol{g}}^1, \hat{\boldsymbol{g}}^2, \hat{\boldsymbol{g}}^3)$ and $(\hat{\boldsymbol{h}}^1, \hat{\boldsymbol{h}}^2, \hat{\boldsymbol{h}}^3)$ must be recomputed at each iteration.

4.6 Data

Three datasets were employed for the validation of the proposed segmentation framework.

4.6.1 Dataset 1: Lumbar Spine of Healthy Subjects

It is composed of 30 CT scans from patients suffering from low back, collected at the National Center for spinal disorders (Budapest, Hungary). Patients were 13 males and 17 females with a mean age of 40 (age interval: 27-62 years). Those patients were selected for participating in the European Commission funded MySpine project [34].

Image resolution: Axial in-plane resolution of 0.608×0.608 mm^2 with a spacing between slices of 0.625 mm.

Training and testing division: This dataset was divided into a testing set, compound of 25 CT images, and a training set of 5 for the feature training [130]. The SSM and SIM were evaluated in a leave-one-out manner. Therefore, for each vertebra in the testing set a model of 29 vertebrae was employed.

Ground-truth information: The ground truth meshes were manually created using the open source software ITK-SNAP [157].

4.6.2 Dataset 2: Lumbar Spine of Pathological Subjects

This database belonged to the spine web [199] and it was collected for vertebral detection purposes (DataSet 3 in the webpage). Thus, images did not have ground-truth, the resolution and image quality was poor, and it contains a large variation of diseases and regions of the spine. Ten images were selected from this database following the criterion of ensuring that the whole lumbar region was in the image and that patients show high degree of scoliosis. In addition, 4 out of the 10 images contain at least one fracture and 3 of them contain calcifications.

Image resolution: The axial in-plane resolution was 0.35×0.35 with a spacing between slices of 2.5mm.

Training and testing division: The whole dataset was used as testing using the training information from Dataset 1. The features remained the same as in Dataset 1 and the SSM and SIM were constructed with the 30 cases from Dataset 1.

Ground-truth information: The ground truth meshes were manually created using the open source software ITK-SNAP [157].

4.6.3 Dataset 3: Thoracic and Lumbar Spine of Healthy Subjects

This database consists of 15 thoracic and lumbar CT scans used in the MICCAI challenge 2014 "Computational Methods and Clinical Applications for Spine Imaging -

Spine and Vertebrae Segmentation" [200]. This dataset is held in the spineWeb [199] as Dataset 2.

Image resolution: Images have an axial in-plane resolution of 0.5×0.5 and a spacing between slices of 1.0mm.

Training and testing division: The MICCAI challenge organisers arranged a group of 10 cases for training purposes and 5 for the testing stage. Thus, features, SIM and SSM were trained with 10 cases.

Ground-truth information: The ground truth meshes were provided by the organisers. However, the training set was corrected to increase its accuracy. The testing remained the same for benchmarking purposes and owing to its higher quality.

4.7 Results

4.7.1 Implementation details

The proposed framework employs an optimisation algorithm with four different energies to acquire the segmentation (Section 4.5.6). In the experiments the weights were kept to 1 for practical reasons, since the framework is not very sensitive to these values. Notwithstanding, other applications may require a further optimisation of the weights.

The second parameter is the number of grid points for the B-splines shape instance (Section 4.3.4). In the experiments, it was shown that set of values ranging from $5 \times 10 \times 10$ to $15 \times 30 \times 30$ per vertebra performed equally well. Smaller values did not have enough flexibility and results lacked accuracy and larger values allowed non-smooth shapes. For the experiments, the smallest grid was employed, $5 \times 10 \times 10$, meaning an averaged spacing of $9.3 \times 9.75 \times 8.25 mm^3$.

Other parameters are:

- The number of landmarks in each vertebra was 4000.

- An SSM per vertebra was employed.

- The number of modes for each SSM was selected as the number that keeps 95% of the total variation. This results in 10,10,10,10,11 when trained with Dataset 1 and 8 from T1-T9 and 7 from T10-L5 when using Dataset 3.

- The weight of the features involving E^{I} were 0.5 mm/in for the directional derivative and $0.3in^{-1}$ for the intensity, where the unit in represents the unit of the image intensity.

- The criteria to stop the segmentation was that 99% of the landmarks do not move more than 0.2 times the size of a voxel in the direction of the normal at the specific landmark. This criteria resulted in 5 to 20 iterations. In addition, the maximum number of iterations were set to 30.

- The size of the profiles was set individually for each landmark p of the mesh. In the first iteration, it was set to 20 voxels in the direction pointing outwards and $\min(20, a)$ voxels pointing inwards. The value a is half of the number of voxels from p to the intersection of the mesh and a line following the normal direction of the mesh at p. In the last iteration, they were set to 4 voxels inwards and 4 outwards.

- The number of resolutions was kept to one, since the initialisation already locates the IVDs in a good location.

4.7.2 Evaluation Metrics

The segmentations were evaluated in two different manners. First, the accuracy was measured using Dice Similarity Index (DSI) [159] between the segmented shapes and ground truths the surface-to-surface distance from the segmented shape to the ground truth. It was computed the mean absolute surface distance (MASD), 95-percentil (95-p) and the maximum or Hausdorff distance (HD).

Second, the overlap between the different vertebrae across the spine was measured. The employed metric for this purpose was the mean intersection volume in voxels and mm^3 in the lumbar and thoracic spine, separately, for each Dataset.

The training databases were employed to create the features, weights, SSM and SIM as explained in Section 4.6.

4.7.3   Quantitative Evaluation of the Method

The attained accuracy measurements for the three datasets are presented in Tables 4.1, 4.2 and 4.3. Each table contains the values with and without the use of the SIM in order to evaluate its importance.

Results show that the SIM increases the accuracy of the segmentations. The reason is that the SIM controls the relative distances of the vertebral bodies and spinous process, allowing the method to find better edges in the global optimisation. In addition, Table 4.4 presents the overlap between adjacent vertebrae in number of voxels and in volume, for all the databases with and without the proposed SIM. It can be seen from the results that the proposed approach eliminates completely the overlap between processes. For all the datasets and vertebrae, it was not encountered a single case of overlap between the structures, which shows the robustness of the SIM. In contrast, the segmentations without this model induce significant overlap, in average over $25mm^3$ per vertebra in healthy spines going beyond $125mm^3$ in pathological cases. The better definition of the inter-vertebral relative positions also translates in an overall improvement of the segmentation accuracy as shown in Tables 4.1, 4.2 and 4.3.

Table 4.1: Vertebra segmentation accuracy in Dataset 1 (healthy lumbar spine) with and without SIM

SIM	Error measure	L1	L2	L3	L4	L5	Global
	Mean DSI(%)	93.3	93.7	93.6	93.6	93.8	93.8
	2xSTD of DSI(%)	3.2	3.2	3.3	3.2	3.2	3.2
No	MASD(mm)	0.5	0.49	0.48	0.50	0.56	0.51
	95-p(mm)	1.11	1.09	1.09	1.09	1.24	1.10
	HD(mm)	4.4	4.3	4.7	4.8	5.6	4.8
	Mean DSI(%)	94.7	95.1	94.9	94.8	93.7	94.8
	2xSTD of DSI(%)	1.8	1.7	1.8	2.1	4.5	2.8
Yes	MASD(mm)	0.48	0.46	0.48	0.47	0.52	0.48
	95-p(mm)	1.02	0.99	0.98	1.03	1.19	1.03
	HD(mm)	4.1	4.1	4.3	4.4	5.2	4.5

Table 4.2: Vertebra segmentation accuracy in Dataset 2 (pathologic lumbar spine) with and without SIM

SIM	Error measure	L1	L2	L3	L4	L5	Global
No	Mean DSI(%)	84.6	83.5	83.3	84.8	85.9	84.4
	2xSTD of DSI(%)	7.4	13.1	6.8	5.5	2.8	7.8
	MASD(mm)	1.36	1.5	1.6	1.41	1.31	1.44
	95-p(mm)	3.9	4.5	4.8	4.1	3.6	4.2
	HD(mm)	8.6	10.4	12.4	10.8	7.2	9.9
Yes	Mean DSI(%)	88.2	87.9	87.3	89.5	88.1	88.2
	2xSTD of DSI(%)	4.7	7.3	7.8	3.5	4.5	5.9
	MASD(mm)	0.94	0.99	1.0	0.89	1.06	0.98
	95-p(mm)	2.48	2.64	2.83	2.33	2.94	2.65
	HD(mm)	5.2	6.0	7.1	6.2	6.3	6.2

Table 4.3: Vertebra segmentation accuracy in Dataset 3 (healthy thoracic and lumbar spine) with and without SIM.

SIM	Error measure	T1	T2	T3	T4	T5	T6	T7	T8	T9	T10
No	Mean DSI(%)	86.9	88.2	86.4	89.1	90.9	89.7	89.4	90.3	91.5	90.2
	2xSTD of DSI(%)	1.2	4.2	3.7	2.9	1.1	2.5	0.5	2.0	0.8	2.1
	MASD(mm)	1.52	0.54	0.63	0.53	0.46	0.54	0.58	0.54	0.53	0.69
	95-p(mm)	2.3	1.51	1.76	1.42	1.16	1.44	1.49	1.43	1.34	2.0
	HD(mm)	6.1	5.2	5.3	4.0	5.0	5.0	4.7	4.1	4.3	5.0
Yes	Mean DSI(%)	86.2	87.8	86.6	89.2	91.4	89.6	89.9	90.9	91.1	91.0
	2xSTD of DSI(%)	2.6	4.3	4.3	1.2	0.7	3.3	1.9	1.7	1.7	2.3
	MASD(mm)	0.72	0.58	0.6	0.51	0.43	0.52	0.55	0.52	0.55	0.59
	95-p(mm)	2.1	1.5	1.68	1.37	1.08	1.38	1.45	1.33	1.45	1.59
	HD(mm)	6.0	4.9	5.5	4.1	5.8	5.0	4.8	3.9	4.9	4.8

SIM	Error measure	T11	T12	L1	L2	L3	L4	L5	Lumbar	Thoracic
No	Mean DSI(%)	90.6	91.6	91.6	92.5	92.3	92.4	91.8	92.1	89.6
	2xSTD of DSI(%)	2.5	2.0	2.2	1.6	1.8	1.7	1.9	1.7	5.2
	MASD(mm)	0.72	0.63	0.69	0.52	0.54	0.59	0.61	0.57	0.66
	95-p(mm)	1.93	1.75	1.49	1.28	1.31	1.48	1.47	1.39	1.66
	HD(mm)	4.8	4.5	5.8	3.8	5.2	4.7	4.7	4.8	4.8
Yes	Mean DSI(%)	91.3	91.3	91.9	93.0	92.9	92.9	92.8	92.7	89.7
	2xSTD of DSI(%)	1.9	2.9	0.6	2.5	2.8	2.2	2.6	2.2	4.2
	MASD(mm)	0.62	0.69	0.50	0.47	0.50	0.50	0.50	0.49	0.58
	95-p(mm)	1.73	1.93	1.31	1.23	1.31	1.29	1.28	1.28	1.56
	HD(mm)	4.4	5.0	5.9	4.1	6.0	4.7	3.9	4.8	4.8

4.7.4   Visual Results

A qualitative evaluation is presented in Figures 4.5, 4.6 and 4.7. Figures 4.5 and 4.7 show the segmentation and ground-truth contours, superimposed to a sagittal and coronal slices of one patient from the Dataset 1 and another from the Dataset 3, respectively. On the other hand, figure 4.6 does not contain the ground-truth contour. It shows the segmentation of a patient from the Dataset 2 with and without the SIM, in order to

Table 4.4: Mean inter-process overlap in voxels and in cubic millimeters for the case of using SIM and without for all the databases.

Spine position	Mean Number of voxels		Mean Volume (mm^3)	
	No SIM	With SIM	No SIM	With SIM
D1: L1 - L5	897.2	0	200.26	0
D2: L1 - L5	2554.9	0	574.8	0
D3: T1 - T12	530	0	132.5	0
D3: L1 - L5	0	0	0	0

D1: Dataset 1 - Only Lumbar vertebrae of healthy subjects.
D2: Dataset 2 - Only lumbar vertebrae of pathological cases.
D3: Dataset 3 - Thoracic and lumbar vertebrae of healthy subjects.

visualise the improvement given by this model. This patient contains a fracture in the L4, which produces the spinous processes of the L3, L4 and L5 to collide. The use of the SIM maintains the separation between these processes under control ensuring not only zero-overlap but also high accuracy. Furthermore, the endplates of these three vertebrae are close to each other leading to overlaps when the SIM is not employed.

(a)   (b)
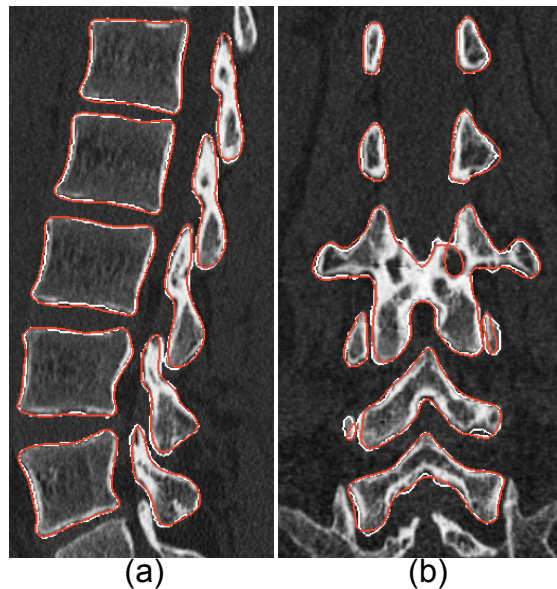
Figure 4.5: Segmentation slices in sagittal and coronal view of one patient CT scan from the Dataset 1. The red contour represents the segmentation and the white contour the ground truth. Check online colour version for better visualisation.
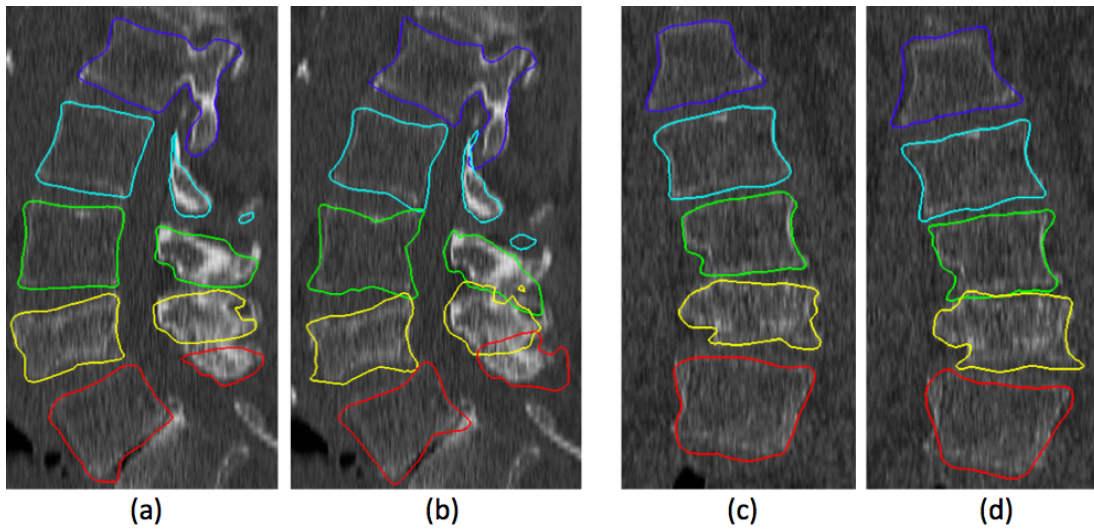
Figure 4.6: Segmentation slices in sagittal and coronal view of one patient CT scan from the Dataset 2. Figures (a) and (c) represent the segmentation using the SIM and figures (b) and (d) without the SIM. It shows that the spinous processes of the L3, L4 and L5 vertebrae merged together because the L4 is fractured. This issue produces large errors and overlaps when the SIM is not employed.

4.7.5 Sensitivity to the Initialization

As explained in Section 4.5.1, the segmentation process requires the centre location of the IVDs. In order to test the sensitivity to this manual input, various patient CT images were segmented pinpointing the centre in different positions within the IVD region. However, the evaluation measures resulted in similar results all the time with and without the SIM. The main difference was the location of overlap regions. An example of large overlap due to a complicated initialisation is presented in Fig. 4.8. The segmentation without using the SIM deforms the L1 vertebra unnaturally, allowing more overlap than in a normal setting, where the SIM still prevent the overlap and maintain the same accuracy than when the initial positions are closer to the real IVD centres.

4.7.6 Comparison with the State-of-the-art

Although image resolution, type of database or the CT machine can influence the performance of different techniques, Table 4.5 presents a comparison of the accuracy
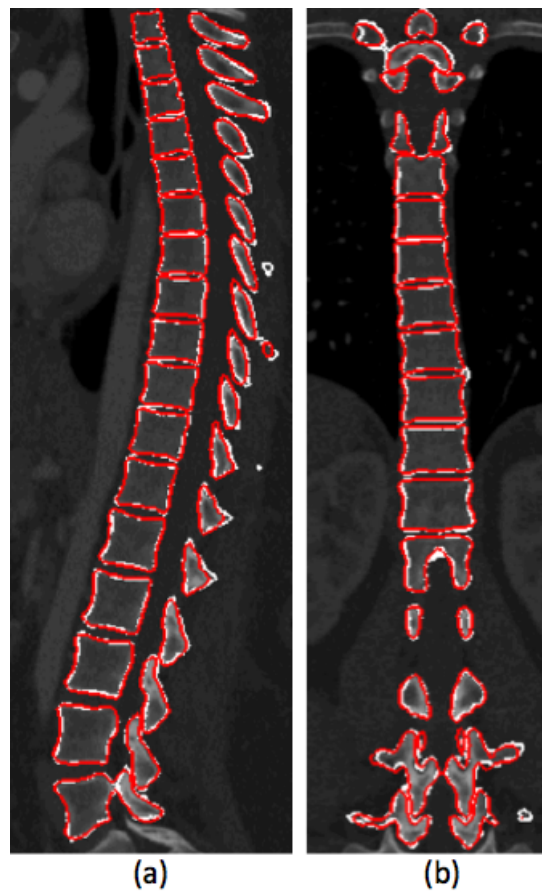
Figure 4.7: Segmentation slices in sagittal and coronal view of one patient CT scan from the Dataset 3. The red contour represents the segmentation and the white contour the ground truth. Check online colour version for better visualisation.

between the state-of-the-art methods. In this table, the shown accuracy was obtained using CT images and evaluating the performance of the segmentation in the whole vertebra (VB + processes). The Dataset 2 was the only one employed for this comparison, since various state-of-the-art methods were tested in pathological cases. Therefore, the accuracy measurements from all the methods presented in Table 4.5 are only from the Lumbar region. An important difference with the results shown in Table 4.2 is that the SSMs and SIMs were created in a leave-one-out fashion using solely the Dataset 2 instead of being computed from the Dataset 1. It can be seen that the proposed technique compares favourably to the existing studies on the topic, while ensuring extra robustness to extract non-overlapping and anatomically meaningful segmentations of the vertebrae.
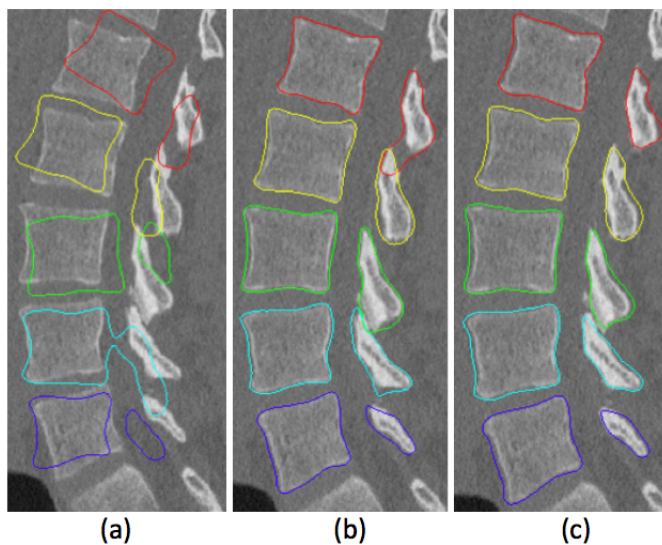
Figure 4.8: Improvement obtained by employing the SIM in the segmentation scheme with a bad initialisation. The image a) is the initial shape, the image b) is the segmentation without using the SIM and the image c) is when the SIM is employed. The main difference is the correction of the process in the L1.

In addition, Table 4.6 presents a comparison of the results of the methods participating in the MICCAI Challenge 2014 on spine imaging [200]. The dataset used for this challenge (Dataset 3) included healthy subjects only, without evident vertebral pathologies. Thus, the incorporation of the SIM does not improve greatly the mean accuracy (see Section 4.8). Its main contribution is the reduction of large errors, which may be measured by the 95 percentile, Hausdorff (maximum) distance, or by specific-purpose measures as the overlapping volume. However, only mean measures (mean DSI and MASD) were computed in the Challenge. The issue of only using this type of measures is appreciated in Table 4.6, where the MASD and mean DSI of the proposed method are less accurate than those using the methodology from Chapter 3 [130], but the 95 percentile and Hausdorff distance are clearly improved. This effect is also observed when comparing the results with those of the method proposed by Korez *et al.* [201], since they provided additional measurements for the training set. The reported MASD (0.35) and mean DSI (93.1) were better than ours (mean DSI of 90.8, MASD of 0.52), but their Hausdorff distance (5.73mm) was not as accurate (ours: 4.6mm). Another example is the method introduced in [170] (Table 4.5), which has a better DSI than

Table 4.5: Comparison of the State of the Art Methods

Study	Image resolution	DSI (%)		Surface error (mm)			
		Mean	STD[1]	MASD[2]	MPSD[3]	95-p[4]	HD[5]
Weese *et al.* [175]	$0.48 \times 0.48 \times (0.72 - 2)mm^3$			0.93			6.14
Kadoury *et al.* [188]	$0.8 \times 0.8 \times (1 - 2)mm^3$			2.8 ± 1.9			
Rasoulian *et al.* [189]	$0.6 \times 0.6 \times 0.6mm^3$ to $0.9 \times 0.9 \times 3.2mm^3$			1.38		3.8	8.91
Klinder *et al.* [185]	0.32×0.32 - $0.98 \times 0.98mm^2$ thickness: $0.8 - 2.8$				$0.73 - 0.79$		
Huang *et al.* [170]	$1.0 \times 1.0 \times 1.5mm^3$	94	2				10.06 ± 1.71
Proposed method	$0.35 \times 0.35 \times 2.5mm^3$	90	5.1	0.82	0.78	2.1	5.5

[1]: standard deviation, [2]: mean absolute surface distance, [3]: mean point to surface distance, [4]: percentile 95 of the surface to surface distance, [5]: Hausdorff distance.

ours but the Hausdorff distance is almost double. For future reference, it was added the 95 percentile and Hausdorff distance in the table.

Table 4.6: Comparison of the Methods That Used the Dataset 3

Study	DSI (%)		Surface error (mm)		
	Mean	STD[1]	MASD[2]	95-p[3]	HD[4]
Forsberg *et al.* [191]	92		0.47		
Seitel *et al.* [190]	87		1.1		
Hammernik *et al.* [202]	95		0.38		
Korez *et al.* [201]	95		0.37		
Castro-Mateos *et al.* [130]	93	4.1	0.55	1.52	6.2
Proposed Method	91	3.4	0.55	1.47	4.8

[1]: standard deviation, [2]: mean absolute surface distance, [3]: percentile 95 of the surface to surface distance, [4]: Hausdorff distance.

4.8   Discussion

Herein a new model (SIM) that represents the interspace between objects in a multi-object structure has been presented. It was tested in the segmentation of the lumbar and thoracic spine, demonstrating its effectiveness to avoid segmentations with unnatural geometries, such as overlaps, that may cause simulations to result in unrealistic outcomes, even when the global accuracy is high.

Since normal metrics do not take into account this overlap effect, it was explicitly

measured the overlap with and without the use of the SIM, showing that this model completely avert overlaps.

However, As mentioned in Section 4.4, the SIM does not guaranteed zero overlap mathematically speaking. However, the likelihood of happening is so small that it never occurred in the experiments. The main difference with other approaches is the employment of a model of the interspace between objects to guarantee that the shapes are not deformed in an unnatural manner as well as decreasing the likelihood of overlapping to almost 0. For instance, the probability of having an infinitesimal overlap is equally likely with or without the energy that blocks overlaps introduced in [185]. In contrast, this probability is much smaller when employing the SIM.

In addition, this model partially controls the possible configurations of the segmentation by restricting the shape of the separation between the objects. This is similar to Statistical Pose Models [186], however less restricted. As shown in Tables 4.1, 4.2 and 4.3, the accuracy of the results does not change greatly by the addition of the SIM when segmenting healthy subjects. In general, the segmentation depends on the intensity, the SSM and the SIM energies. In the case of healthy subjects, the SSM contained enough flexibility to accommodate the shapes with a small error and the borders of the images were clear enough for the intensity energy to drive the shape to the right positions. Thus, the SIM did not influence the resultant shape in a great manner. However, in the case of pathological cases, the SSM energy tried to deform the shape to be similar to the closest healthy vertebra within its scope, which could have large differences. In addition, the borders were not clear and the intensity energy failed at finding the correct borders. Under these circumstances the SIM had a great impact at controlling the separation between the vertebral bodies and processes to find the most realistic shape. Observe that there are two factors for unclear borders: the first one is due to the pathology and not to the image quality (collision of vertebrae, decalcification, etc...), the second is due to the image protocol (voxel size, windows type, etc...). Dataset 1 and 3 did not have any issues whereas dataset 2 contain unclear borders due to both factors, large voxel size, fractures, etc...

The SIM and the SSM restrict the possible shapes of the segmentation. However,

the intensity energy is the only one that deforms the shape within the image. The method employed in this framework is based on the selection of a group of features (Chapter 3) that was proven to be accurate in the case of dataset 1 [130]. However, it may happen that other energies provide more accurate results for other datasets. Since, this energy is interchangeable for any other while maintaining the same framework with the SSM and SIM, it could be possible to use one of the proposed energies from the methods in Table 4.6 to improve the border detection.

4.8.1 Limitations

The proposed method requires the manual selection of the IVDs centre. To overcome this limitation an automatic centre detection, such as the one proposed by [91], may be employed. Another issue of the method is that an SIM is created to model the variations of the space between two surfaces. Therefore, the external objects in the structure, which are vertebrae T1 and L5 in the thoracic and lumbar spine, may over-segment to external structures that are not considered in the model (Fig. 4.9). A feasible solution may be to include a part of objects that are outside the structure, vertebrae C6, S1, to model the interspace.

4.8.2 Computational Cost

The experiment were run using a PC with Intel(R) Xeon CPU E5620 at 2.40 Ghz with 8 GB of RAM and running a 64-bit Windows 8.1 operating system. All the code was written in C++ using the libraries from the Insight Toolkit [157] for basic manipulation of mesh and images. The proposed framework requires around 50 seconds per vertebra to perform the segmentation and only 1 second to initialise all the vertebra after manually selecting the centre of the IVDs. In contrast, the standard Active Shape Model [32] or the methodology from Chapter 3 [130] only requires 15 seconds per vertebra. The reason for the increase to 50 seconds is that the proposed framework employs a steepest gradient descent algorithm to do the optimisation because it does not have a closed-form solution. Observe that by removing the SIM but maintaining the same segmentation framework the process requires 49 seconds, it is only around
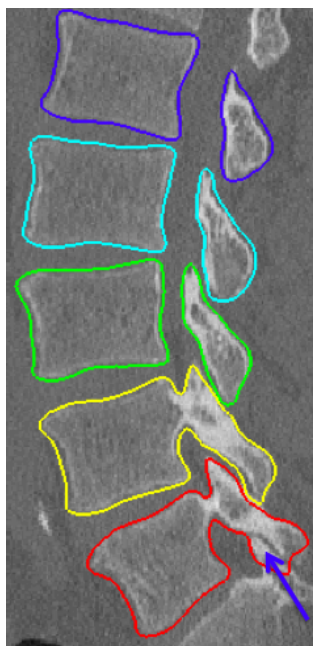
Figure 4.9: The SIM requires two surfaces in order to model the space between them. Therefore, in the low spine segmentation paradigm the L1 and L5 may leak into their top and bottom vertebra, respectively. In this figure, this issue is shown with a blue arrow in the L5.

1s faster per vertebra.

4.9 Conclusions

In this chapter, it was introduced the statistical interspace model (SIM), embedded in a framework for segmenting a multi-object structure. This method was tested on three databases of CT images of the spine. The SIM was employed to avoid the overlap in the vertebral and spinous processes and to maintain the correct separation between vertebral bodies.

The results show that SIM not only prevent vertebral overlaps but also increases the accuracy of the segmentation by maintaining the relative position of the vertebral bodies and the spinous processes. This control was found to be necessary in pathological cases, where vertebral bodies and/or spinous processes collapse with neighbouring structures.

Furthermore, the proposed framework is not restricted to vertebra segmentation, it

could be applied to other anatomical parts such as intervertebral disc (IVD), knees, heart or any other multi-object structure, where the control of the relative position among the individual objects is required to restrict rotations, translation and/or to prevent overlap between different tissues. However, as mentioned at the beginning of Chapter 3 the SIM does not provide a greater improvement in the case of segmenting IVDs, since their separation is large enough to avoid overlaps and excessive separation. Thus, the higher computational time of this framework makes it less appealing for IVD segmentation than the previously introduced ASM with feature-based searching (Chapter 3.2.4).

Chapter 5

Prediction of the degree of degeneration of IVDs

The previous two chapters were dedicated to the study of segmentation frameworks to provide anatomical models from medical images. The current and following chapter deal with the labelling of the structures according to some medical conditions, which are able to alter their material properties. In particular, this chapter provides a method to classify IVDs according to their degree of degeneration. This degenerative process induces a reduction of the IVD water content and a variation of the amount and type of its collagen. Therefore, the automatic detection of the IVD degeneration grade is essential for the proper computation of the material properties of the IVDs.

The proposed method extracts a set of designed shape and intensity features from the segmentation of IVDs to train a neural network. Although, this method may be used in 2D or 3D, it was decided to employ the mid-sagittal MR image solely and use 2D segmentations of IVDs. The reason behind this choice was that the examination of the central T2 MR slice is the medical standard for evaluating IVD degeneration. This process allows this approach to be used in the case of having MR images with one or few number of slices. The segmentation was performed with a simplification of the method proposed in Chapter 4. In this simplification, the SIM model was not used, the SSM was changed by a geometrical energy and the B-splines parameterisation was substituted by the internal energy of the snakes [138]. The first simplification

was performed to remove the need of training exploiting that the IVD shape in 2D is closely related to an ellipse. The second simplification was used to speed up the process, by allowing the method to be optimised using a greedy approach instead of gradient descent. Observe that this segmentation approach may be explained using the snakes framework by using as external energy the image energy presented in Chapter 4.

This chapter is adapted from two previous publications [31, 57].

5.1   Motivation

Intervertebral disc (IVD) degeneration or Degenerative Disc Disease (DDD) is associated with genetic and environmental factors [203]. In addition, It is believed that many IVD disorders are due to mechanical origins producing, in many cases, changes in the IVD morphology and histology [204]. Thus, the quantification of the degeneration is a common parameter, used to estimate the material properties of the IVDs in order to perform biomechanical and mechanobiological simulation of the spinal conditions and treatments [205].

Since the biological process of IVD degeneration and its clinical consequences are still unclear in many details, there have been some studies to correlate DDD with other disorders, such as low back pain [132, 206] or osteoarthritis of the facet joint [207].

These studies are often performed with the recruitment of hundreds or even thousands of subjects. In the everyday clinical practice, the follow-up of disc degeneration, in a given patient, may be important in understanding the progress of the patient's symptoms. In addition, the manual classification of disc degeneration suffers from a relatively high intra- and inter-observer variability. Therefore, a reliable method for the automated classification of IVD degeneration would be a very helpful and time saving tool.

In clinical routine, clinicians base their diagnosis of disc degeneration on 2D analysis of Magnetic Resonance (MR) images. The most common view for this purpose is the mid Sagittal slice, since most of the herniations occur close to the spinal cord,

because of the curved shape of the spine.

In the literature, different grading system has been proposed [158, 208–210]. In this article, the Pfirrmann grading system [158] was selected because it is widely used in clinical practice and most of the methods performing automatic classification of IVD degeneration use this grading system. This criterion divides the degeneration into five degrees as depicted in Fig. 5.1.
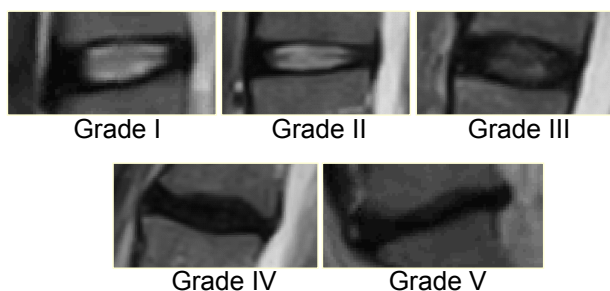
Figure 5.1: Example of the five degrees of degeneration from (a) to (e).

Herewith it is presented a quasi-automatic 2D segmentation method of intervertebral discs on mid-Sagittal slice, which is further employed to extract a set of shape and intensity features that are used for evaluating the degree of degeneration of IVDs.

As previously mentioned, the most common medical procedure to evaluate the degeneration of the IVDs is the examination of the mid-sagittal slice of T2 MR image. Thus, to allow the method to be used when only this slice is present, it was decided to use solely the information from this 2D image to compute the classification. The direct implication of this decision was that the segmentation was required to be performed in 2D images. Although the same framework explained in Chapter 3 or 4 may be used, the SSM needed to be recomputed. However, the shape of an IVD in 2D is close to that of an ellipse and an important feature for the proper detection of the degree of IVD degeneration is the ration between the width and the height of the IVD in 2D, which coincides with the long and short axis of an ellipse. These two arguments led to the development of a segmentation method that employs a geometrical energy based on an ellipse to provide the prior information that in previous chapters had been obtained using SSMs. This approach avoids the need of training allowing the method to be

reimplemented in other institutions that do not have a training database.

5.2 Methodology

The proposed method requires an initial selection of the centre of the IVD, which is used to initialise an elliptical contour that is deformed using a variation of active contour models [211] and further improved using Fuzzy C-means [212]. The classification of the degree of degeneration is based on eight features: the short axis over the long axis of the interpolated ellipse of the segmentation, the mean and standard deviation of the intensity of the IVD's nucleus after applying fuzzy logic in two different manners and the ratio of the intensity inside and outside the nucleus in the original image and after the two different fuzzy clustering. The classification is performed using a Neural Network [213] trained with these eight features. The validation of the method was carried out on a database of 240 Lumbar IVDs, from 48 different patients.

5.2.1 Intervertebral disc segmentation

Background

Early work on 2D segmentation of the mid-saggital slice was carried out by Chwialkowski *et al.* [139] and Roberts *et al.* [140].

More recently, Ruiqiong *et al.* [141] developed an automatic segmentation method based on a edge detection algorithm within a small windows, which was slid along the left side of the previously segmented spinal cord, however the results were not accurate. A watershed approach was proposed by Chevrefils *et al.* [142], the main disadvantage was the over-segmentation. An atlas-based 2D segmentation method was developed by Michopoulou *et al.* [21], in which a combination of ASM and Fuzzy C-means was employed to segment the IVDs. Its drawback is the need for a manual rigid registration and large data training for the statistical model. A recent work published by Ayed *et al.* [16] carried out the segmentation using Graph Cuts, the method was completely automatic but the results were not highly accurate. A different methodology was proposed by Law *et al.* [143]. Their approach was based on anisotropic oriented flux,

which provides highly accurate results. However, it employs a large number of steps, which harden the extension of the algorithm to other body tissues.

Initialisation

This method assumes that a rough centre position of the IVD is provided. From the centre, three lines are thrown at 0, 25 and 50 degrees and the point within every line with a maximum intensity is selected. If the intensity of any of the points is much lower than the other two, it is erased. Then, the point with the minimum distance to the centre is selected as the position of the marrow. Afterwards, a square, centred in the manual point, with double size of the distance from the centre to the marrow is cropped out as the Region of Interest (ROI).

Having selected the ROI, the contour of the IVD is initialised as a 60-point ellipse, which was placed in its centre with a vertical axis of $0.2 \times$ size of the ROI and the horizontal axis of $0.4 \times$ size of the ROI.

Active contour model

Active contour models or Snakes are energy minimising and deformable splines, closed or open, which adapt to contours by means of different constraints. In general, the equation of the snake's energy can be written as :

$$E_{\text{Snake}} = \int E_{\text{internal}}(v(s)) + E_{\text{image}}(v(s)) + E_{\text{aux}}(v(s))ds \qquad (5.1)$$

where $v(s)$ describes the position of the control point s in the image. Greedy algorithms [214] are commonly used to adapt the snakes to the object of interest, by displacing every point in the contour within a neighbourhood inside the image, in an iterative manner. In the proposed method, the neighbourhood of a point s was chosen to be a line, whose direction is the normal to the curve at s. The three energies were computed using this intensity profile, and the pixel with the minimum value was selected as the new position for that point.

The internal Energy is usually described as:

$$E_{\text{internal}} = \frac{1}{2} \left(\alpha(s) \left\| \frac{\mathrm{d}\boldsymbol{v}(s)}{\mathrm{d}s} \right\|^2 + \beta(s) \left\| \frac{\mathrm{d}^2\boldsymbol{v}(s)}{\mathrm{d}s} \right\|^2 \right) \tag{5.2}$$

The first part of the energy maintains the distance of the control points with similar length, whereas the second term penalises sharp curvature. α and β are the weights, which may be updated during the process in order to increase or decrease their values, when the energy is too high or low, respectively. Since the new positions are along the normal direction of the curve at the control points, the α was set to 0 in the experiments. On the other hand, β is modified with the following equation.

$$\beta(s) = \begin{cases} 1.2\,\beta(s) & \text{if } E_{\text{internal}} > 2\beta_0 \text{ and } \beta(s) < 4\beta_0 \\ \beta(s)/1.2 & \text{if } E_{\text{internal}} < \beta_0/2 \text{ and } \beta(s) > \beta_0/4 \\ \beta(s) & \text{otherwise} \end{cases} \tag{5.3}$$

The image energy usually involves the gradient on the neighbourhood of the pixel. In this approach, it was used a directional derivative for an energy that finds its minimum in changes from low to high intensities:

$$E_{\text{image}} = \gamma(s)\,\hat{\boldsymbol{n}}(s)\cdot\nabla I(\boldsymbol{v}(s)) = \gamma(s)\frac{\partial I(s,p)}{\partial p}, \qquad \text{where} \quad I(s,p) \equiv I\left(\boldsymbol{v}(s) + p\cdot\hat{\boldsymbol{n}}(s)\right) \tag{5.4}$$

p is the position along the normal direction $\hat{n}(s)$ at $\boldsymbol{v}(s)$, pointing outwards of the contour. The weight of the external energy $\gamma(s)$ is computed using the following equation:

$$\gamma(s) = \gamma_0 \times \left(1 + \frac{\left.\dfrac{\partial I(s,p)}{\partial p}\right|_{p=p_{\text{selected}}}}{\max(I(s,p)) - \min(I(s,p))} \right) \tag{5.5}$$

where the value of γ_0 was set to 4.

As explained in the introduction, a new energy (geometrical energy) was added into the proposed segmentation framework in order to achieve similar results to those obtained with SSM but without the need of training. In order to compute this new energy, a simplified geometrical shape (based on the knowledge on the target object)

must be fitted to the control points of the snake. Then, a distance map image is created by filling every pixel with its distance to the border of the aforementioned geometrical shape. In the case of IVDs, the selected geometrical shape was an ellipse.

Since the purpose is to maintain the contour close to a geometrical form in shape but allowing small deformations, the distance map is exponentiated with a value ρ as follows:

$$E_{\text{aux}} = \rho^{\text{Distance Map}(\boldsymbol{v}(s))} \tag{5.6}$$

where ρ was selected as 1.25. Thus, small distances have little influence but large ones are prohibited. Observe, that this energy could employ an SSM in the same manner as the ellipse fitting is used.

Fuzzy logic

A usual problem when dealing with an active contour model is to ensure that the selected number of points is large enough to obtain a properly segmented shape, but small enough to maintain a sufficiently large distance between the points to avoid fake internal energies. In the proposed method, the number of points was reduced when the distance between them was inadequate but it was never increased. Therefore, in order to deal with a segmentation that has insufficient detail, fuzzy C-means was employed to create an image with the probability of each pixel belonging to the IVD. This post-processing technique assesses every point in the contour by means of the largest decrease in probability and allows a movement of up to two pixels normal to the contour to acquire a more accurate shape (Fig. 5.2).

5.2.2 Classification of the degree of degeneration

The study addressed in this section aims to classify the IVDs into healthy (Grade I and II), low-level degeneration (Grade III), high-level degeneration (Grade IV) and collapsed space (Grade V). There exist two different components that are to be optimised: features and classifier.

(a)	(b)
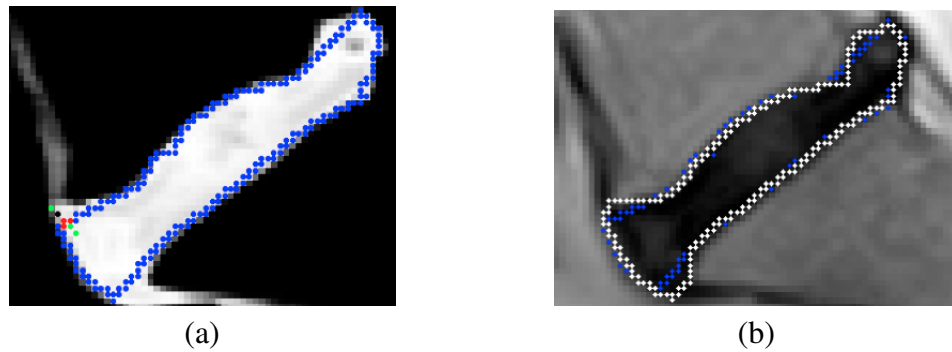
Figure 5.2: (a) The searching algorithm is shown, where the red dots are the points in search and their neighbours, the blue ones are the predicted contour by the snake, the green dots are the searching line and the black one the new best position. The background is the fuzzy classification. (b) The original image is shown in the background and the output from Snakes (in blue) and the final result with Fuzzy Logic (in white) are superimposed.

Grades I and II were merged due to the large inter-variability found among the three experts. Furthermore, the database contains a small number of cases hindering the classification between these two grades. Nevertheless, these grades are considered to be healthy, and in general, it is rare to find IVDs of grade I in adults, since IVDs undergo the degeneration process with age.

Background

Despite of the clinical significance of the classification of the intervertebral discs, most of the methods in the literature only consider healthy and unhealthy discs [139, 215–219]. This separation corresponds to the difference between degrees I, II and III, IV, V in the Pfirrmann classification.

In contrast, Lootus *et al.* [220], proposed a method to perform a three level classification of the IVD by using a ± 1 precision. Thus, neighbour grades are considered to be the same. Their approach extracts the IVD region using a vertebral body segmentation approach. Subsequently, a group of features is extracted from the IVD region and the degeneration grade is estimated using a regression model. A recent work, developed by Ruiz-España *et al.* [221], produces a full classification of the IVDs using the intensity across the height of the IVD. Although, these intensities are well suited

as features, they are not decisive on their own.

In addition, previous methods do not provide a detailed evaluation of the performance, hindering the comparisons with their approaches. In contrast, we present a comprehensive evaluation, specifying the results by different IVD positions and degeneration degrees.

Features

In his article [158], Pfirrmann classified the degree of degeneration into five categories employing the following information (Pfirrmann's features):

P1: Signal intensity in the nucleus.

P2: Homogeneity of the intensity. Is there any cracks or dark spots in the nucleus?

P3: Distinction of the nucleus and annulus.

P4: Height of the IVD.

In this article, a set of eight features was employed to classify the IVDs in an attempt to emulate the idea behind Pfirrmann's rationale.

Three images were employed to compute the proposed set of features.

- **Image A:** Original T2-weighted image.

- **Image B:** Image as a result of a fuzzy clustering, considering only the segmented region of the studied IVD.

- **Image C:** Image as a result of a fuzzy clustering, considering the whole ROI for the studied IVD as explained in section 5.2.1.

In both derived images B and C, the fuzzy clustering method created an image with the probability that a pixel belonged to the darkest cluster within the segmentation area. The number of clusters was manually selected as 2, since the classification should separate between annulus and nucleus. A fuzzy clustering considering only the segmented region, Image B (Fig. 5.3 - b), allows a large intensity separation between the nucleus and annulus, providing information between grade 3 and 4. On the other hand, the use

of the whole ROI , image C (Fig. 5.3 - c), provides large intensity separation between annulus and nucleus when the grade are 1 or 2, and permits the integration of spots and cracks information that improve the separation between grade 2 and 3.

In addition, a region A within the IVD to roughly represent the nucleus was defined. This region was described as an ellipse with a short axis of $0.9 \times b$ and a long axis $1.5 \times b$ (red ellipse in the images in Fig. 5.3).

The eight features and their correlation with the Pfirrmann's features are depicted in Table 5.1.

Table 5.1: Description of the eight features used for the classification of the IVD according to their degeneration grade. The third column provides the Pfirrmann's feature that is being explained. The flatness of the IVD was computed as the ratio between the short axis (b) and long axis (a) of the fitted ellipse to the IVD segmentation.

Features	Explanation	Pfirrmann's features
Feature 1 (F_1)	MIA of image B	P1
Feature 2 (F_2)	MIA of image C	P1
Feature 3 (F_3)	SDA of image B	P2
Feature 4 (F_4)	SDA of image C	P2
Feature 5 (F_5)	RIA of image A	P3
Feature 6 (F_6)	RIA of image B	P3
Feature 7 (F_7)	RIA of image C	P3
Feature 8 (F_8)	Flatness of the IVD	P4

MIA: Mean intensity in region A.
SDA: Standard deviation of the intensities in the region A.
RIA: Ratio between the mean intensity in region A and the mean intensity in the whole IVD except region A.

The Classifier

Although the selection of the set of features is the most important information to perform proper classifications, the classifier may also influence the accuracy of the results. In this work, the classifier was selected by comparing the sensitivity that different classifiers achieved on the training set.

Table 5.2 shows the sensitivity of the IVD classification according to their degree of degeneration, employing different classifiers and parameters. The results, shown in
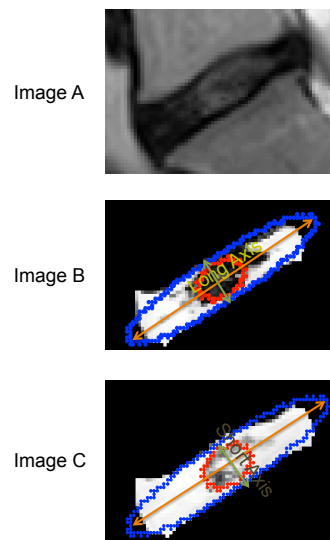
Figure 5.3: Representation of the eight features for the classification of the IVD image (a). The first and third features are the mean and variance intensity of the pixels within the small ellipse (region A) in image (b) and the second and fourth ones are the same values in image (c). The next three features are the ratios between the intensity in the small ellipse and the intensities in the segmented area but the small ellipse, in images (a), (b) and (c). The last feature is the long axis divided by the short axis of the large ellipse

the table, are organised according to the sensitivity that was achieved in the training set. The classifiers and their parameters are:

- **NN-1:** Neural network (NN) with a random initialisation. This classifier contained 1 hidden layer with 12 neurons.

- **Ad:** Adaboost with 10 iterations.

- **SVM-1:** Support Vector machine with a polynomial of order 3.

- **LR:** Logistic Regression with a polynomia of order 3.

- **SVM-2:** Support Vector machine with Gaussian radial bases.

- **NN-2:** Neural network (NN) with Swarm optimization. This classifier contained 1 hidden layer with 12 neurons.

The parameters, such the order of the polynomial or the number of iterations of adaboost. Since a separation between training and validation set would result in a low

number of cases, the training of these parameters was performed in a leave-one-out manner. When training a Neural network, the training set was divided into a validation set of 15%, and training set of 85% to avoid over-fitting.

Table 5.2: Sensitivity obtained with different Classifiers.

Classifiers	NN-1	Ad	SVM-1	LR	SVM-2	NN-2
Sensitivity	0.86	0.89	0.90	0.90	0.90	0.91

Although the performance of the classifiers is not very different, the NN-2 was selected.

5.3 Data

A database of T2-weighted MR images of 240 human low back intervertebral discs, using an open MR machine of 0.4 Tesla (Hitachi, Twinsburg, Ohio) was collected at the National Center for Spinal Disorders (Budapest, Hungary). All the images have a resolution of 0.68x0.68 mm^2.

Patients were 25 males and 23 females with a mean age of 44 (age interval: 27-62 years). Those patients were selected for participating in the European MySpine project, which had received approval of the institutional review board as well as a written informed consent from all subjects.

Using Pfirrmann's classification (grades I to V) to group the IVDs according to their degree of degeneration led to table 5.3.

Table 5.3: Degeneration Grade in the Dataset

Degeneration Grade	I	II	III	IV	V
Discs in L1-L2 positions	0	14	30	3	1
Discs in L2-L3 positions	0	21	21	6	0
Discs in L3-L4 positions	5	17	17	7	2
Discs in L4-L5 positions	4	10	13	17	4
Discs in L5-S1 positions	2	6	19	9	12
Discs per degeneration	11	68	100	42	19

5.4 Results

5.4.1 Implementation details

In the proposed scenario, there are two main group of parameters involving segmentation and classification. The segmentation is based on a Snake framework that contains the four parameters (α, β, γ, and ρ) introduced in Sec. 5.2.1. Although these weights are optimised with the algorithm, their initial value influences the speed and convergence. In our experiments, their values were:

- α: 0.

- β: 3

- γ: 4

- ρ: 1.25.

The classification parameters are the selection of the classifier and specific values in the feature computation. The selected classifier was Neural Network with Swarm optimisation [213]. The classifier employed one hidden layer and 12 neurons.

5.4.2 Evaluation of the method

The evaluation of the segmentation was performed by using two standard measures, Dice Similarity Index (DSI) between the segmented disc (SD) and its ground truth (GT), and Root Mean Square Error (RMSE) between the contours of the SD and the GT. The GT was created by an expert using ITK-SNAP [222].

$$DSI = \frac{2 \times (GT \cap SD)}{GT + SD} \times 100\% \tag{5.7}$$

$$RMSE = \sqrt{\frac{1}{M} \sum_{i=1}^{M} \|SD_i - GT_i\|^2} \tag{5.8}$$

where, M was the total number of pixels surrounding the segmented shape, SD_i are the points in the segmented Disc and GT_i the points in the Ground truth.

To evaluate the accuracy of the classification algorithm, three experts manually labelled the cohort of 240 IVDs and the most voted value for each IVD was selected as the ground truth. For the creation of the ground-truth, the experts were allowed to look through the different slices of the same image. However, in the case of the automatic method, the mid-sagittal slice was the only input.

This dataset was divided into a training and validation set (140 IVDs) and testing set (100 IVDs). This division was performed automatically, trying to preserve the same relative quantity of the five different type of degeneration at each lumbar position using the method implemented in [69].

The inter-observer variability was computed as the mean of the specificity and sensitivity of each observer compared to the ground truth. In order to evaluate the performance of the proposed automatic method, its specificity and sensitivity were also computed against the ground-truth and compared with the inter-observer variability,

$$\text{Specificity} = \frac{\text{TN}}{\text{TN + FP}}, \qquad \text{Sensitivity} = \frac{\text{TP}}{\text{TP + FN}} \qquad (5.9)$$

where TP, TN, FP and FN are the number of true positives, true negatives, false positives and false negative, respectively. In addition, their 95% confidence interval (CI) was computed. This CI was computed assuming a Gaussian approximation of the binomial distribution (mean $\pm$ 2$\times$standard deviation), since it is a common approach that can be used for benchmarking.

$$\text{Var(Spe)} = \frac{\text{Spe(1-Spe)}}{\text{TN+FP}}, \quad \text{Var(Sen)} = \frac{\text{Sen(1-Sen)}}{\text{TP+FN}} \qquad (5.10)$$

Observe that when the number of samples is small or the Sensitivity or specificity is close to 0 or 1, this approximation fails. Thus, a Wilson confidence interval (WCI) was also employed, this interval has better coverage than the 'exact' interval (Clopper-Pearson interval) and it does not have any Bayesian influence (Jeffrey interval) [223].

Furthermore, we employed the score test [224] to measure the similarity between the inter-observer variability and our results, since this test has been proved to be the most powerful test when the tested values are close to each other.

5.4.3 Segmentation results

The quantification of the segmentation results is presented in Table 5.4. Several typical examples of segmentation performed on discs with each type of degeneration are shown in Fig. 5.4.

Table 5.4: Accuracy of the segmentation. SD stands for standard deviation and CI for confidence interval.

Degeneration Grade	I	II	III	IV	V	Global
Mean DSI	90.9%	92.5%	92.6%	90.2%	87.5%	91.7%
2 x SD of DSI	4.7%	4.5%	3.5%	7.0%	7.5%	5.6%
Mean RMSE (mm)	0.97	0.78	0.75	0.97	0.91	0.82
95% CI(mm)	1.08	0.82	1.09	1.81	1.69	1.36

Comparison with the state of the art

Table 5.5 presents a comparison with the state-of-the-art methods. The proposed segmentation method achieves comparable or more accurate results than those in the state-of-the-art. In fact, only the method of Law *et al.* [143] has slightly better DSI values, but their RMSE was clearly higher.

Table 5.5: Comparison with state-of-the-art methods

Type of Measurement	DSI All IVDs	DSI Degenerated IVDs	DSI Non-degenerated IVDs	RMSE All IVDs in (mm)
Michopoulou [21]	-	87.4%	91.7%	-
Ayed [16]	88%	-	-	2.73
Law [143]	92.04%	-	-	0.98
Proposed Method	91.73%	91.37%	92.21%	0.82

5.4.4 Classification results

Table 5.6 presents both the Gaussian approximation of the CI (GCI) of the sensitivity (sen) and specificity (spe), as well as the respective WCI obtained from the testing set (Section 5.4.2). Observe that the confidence intervals for the global specificity were

not computed since these intervals are only valid for binomial distributions and the global specificity is a multinomial distribution.

In order to compare the inter-observer variability and the results from the proposed method, the score test was used. The p-values obtained with this test were always above 0.97, meaning that is not possible to ensure that both values are not equal.

Table 5.6: Accuracy of the classification, by measuring the specificity (spe) and sensitivity (sen) $\pm$ 2 standard deviations and the Wilson confidence interval (WCI). The ground truth was selected as the most voted value of each IVD among the three experts manual labelling. The accuracy of these experts is shown in the observers' rows (Ob). The automatic method (AM) required a training set of 140 IVDs and the result was assessed with a testing set of 100 IVDs.

Degeneration Grade	I & II	III	IV	V	Global
GCI Sen Ob.	81.3%±8.0%	85.0%±6.4%	90.0%±7.9%	100%±0%	85.2%±4.6%
GCI Spe Ob.	94.8%±3.0%	92.7%±3.9%	94.2%±2.9%	97.8%±1.7%	94.4%
GCI Sen AM	87.5% ± 11.7%	85.7%±10.8%	83.3%±17.6%	100%±0%	87.3%±4.4%
GCI Spe AM	93.1% ± 6.0%	88.3% ±8.3%	97.7%±3.2%	100%±0%	95.5%
WCI Sen Ob.	72.3% - 87.8%	77.6% - 90.1%	80.1% - 96.0%	86.2% - 100%	79.3% - 89.6%
WCI Spe Ob.	91.1% - 97.1%	88.0% - 95.7%	90.6% - 96.4%	95.5% - 99.0%	-
WCI Sen AM	71.9% - 95.0%	72.2% - 93.3%	60.8% - 94.2%	67.6% - 100%	78.2% - 93.9%
WCI Spe AM	84.8% - 97.0%	77.8% - 94.2%	91.9% - 99.4%	96.2% - 100.0%	-

In order to provide the relative influence of each feature, Table 5.7 presents the sensitivity and specificity of each feature together with the eighth feature. Observe that at least two features are necessary to train the classifier and since the eighth feature only provides meaningful information for the separation between the fifth degree and the rest, it was considered the most appropriate for this test.

Table 5.7: Comparison of the classification power of each individual feature together with the eighth feature.

Degeneration Grade	I & II	III	IV	V	Global
Sen/Spe F_1 & F_8	68/91%	81/72%	75/93%	75/100%	75/90%
Sen/Spe F_2 & F_8	0/100%	17/92%	25/93%	100/100%	50/75%
Sen/Spe F_3 & F_8	81/87%	77/79%	63/95%	100/100%	78/92%
Sen/Spe F_4 & F_8	0/100%	14/84%	25/80%%	50/96%	43/69%
Sen/Spe F_5 & F_8	36/73%	65/51%	75/90%	50/100%	55/78%
Sen/Spe F_6 & F_8	0/100%	84/100%	38/71%	0/100%	41/68%
Sen/Spe F_7 & F_8	72/81%	70/73%	50/95%	75/100%	70/88%
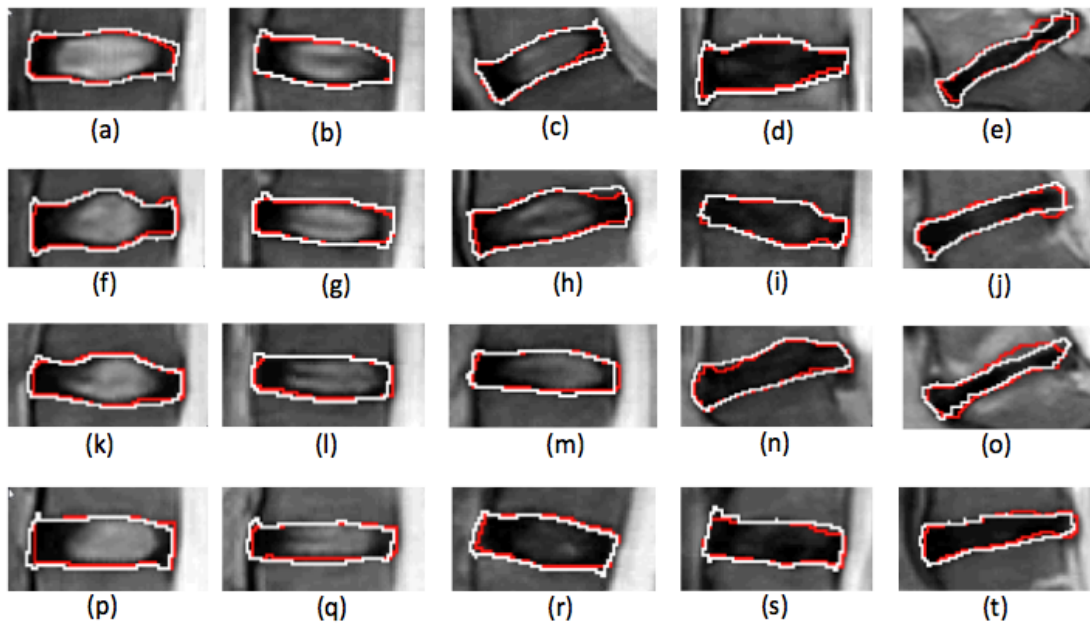
Figure 5.4: Examples of segmentation of all the degrees of degenerations, the red contour is given by the algorithm and the white one is the Ground Truth. Every row contains a different degree of degeneration, the column starting with (a) is Grade I (b) is Grade II (c) is Grade III (d) is Grade IV and (e) is Grade V. Herniations can be observed in (e) and (j). Setting parameters: $\alpha = 0, \beta = 3, \gamma = 4, \rho = 1.25$

5.4.5 Computational time

The algorithm was tested in a Windows 7, 64-bit computer with Intel(R) quad-core Xeon CPU E5620 at 2.40 Ghz with 8 GB of RAM. All the code was written in MAT-LAB and the averaging elapsed time was 1.13 seconds per disc.

5.5 Discussion

The aim of this study is twofold. On the one hand, a new method for IVDs segmentation, which could be extended to other anatomical parts such vertebral bodies, livers, bladders, etc. was proposed. On the other hand, a method to classify IVDs by the degree of the degeneration was presented, which could help physician to focus on problematic IVDs. This classification plays a key role, together with the IVD segmentation, for automatically detecting spinal diseases, as well as for patient-specific

predictive systems to treat various spinal pathologies [225].

5.5.1 Discussion of the segmentation algorithm

The segmentation method relies on snakes. It employs a new term, the geometrical energy, in order to control disc border leakage to neighbouring edges, which could not be controlled only with internal energy (Fig. 5.5). The method also employs a fuzzy clustering step to improve the accuracy in contour details, which were smoothed due to the distance on the snake control points.
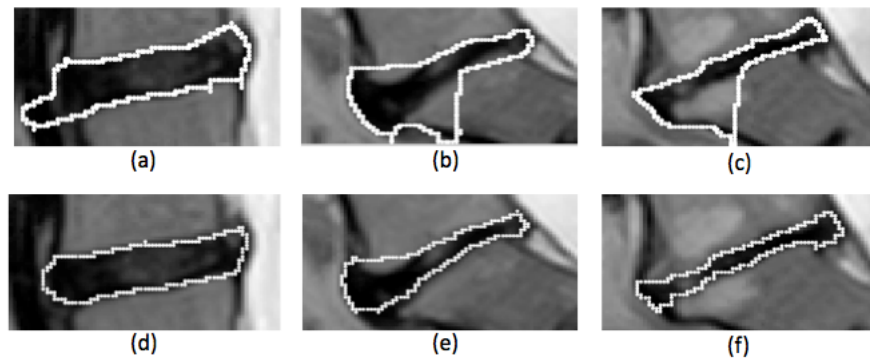
Figure 5.5: Segmentations (a) to (c) were obtained cancelling the elliptical distance map contribution with the setting parameters presented along this work ($\alpha = 0, \beta = 3, \gamma = 4, \rho = 0$), (d) to (f) were achieved by using the distance map ($\rho = 1.25$)

The mean DSI goes from 87.5% to 92.6% of accuracy with a global mean value of 91.73% (Table 5.4). Therefore, the method was found to be accurate and stable with respect to the type of degeneration. It is important to remark that degree of degeneration 5 means the disc collapsed, thus reducing its area. Therefore, a pixel of variation has a higher impact on the DSI in this sort of IVDs than in the ones with lower degree. A standard measure, which does not suffer this problem, is the RMSE of the points of the segmented shape to the ground truth contour. As it is shown in Table 5.4, the RMSE remains stable across the different degrees of degeneration. A qualitative evaluation is presented in Fig. 5.4, it can be appreciated that the ground truth and the automatic segmentation overlap in most of the contours.

Furthermore, the proposed method achieves similar results to those of the state-of-the-art (Table 5.5) with a less complex algorithm that can be easily extended to

other anatomical parts as shown in Fig. 5.6. This figure illustrates the segmentation of vertebrae in MR and CT using the same weights as for IVDs. However, the distance map was changed to a rectangular shape and the oriented derivative was modified to find the maximum in a high to low intensity jump.

Another extension of this method is to employ statistical shape models when the shape cannot be expressed in a geometrical manner. The ellipse or square fitting should be replaced by the projection into the SSM space and the same technique may be employed. Observe, that by using this methodology, the results are more robust to all the previously mentioned drawbacks of ASM (Chapter 2), such as large training sets. In fact, only an affine transformation over the average shape could replace the SSM projection on this framework.
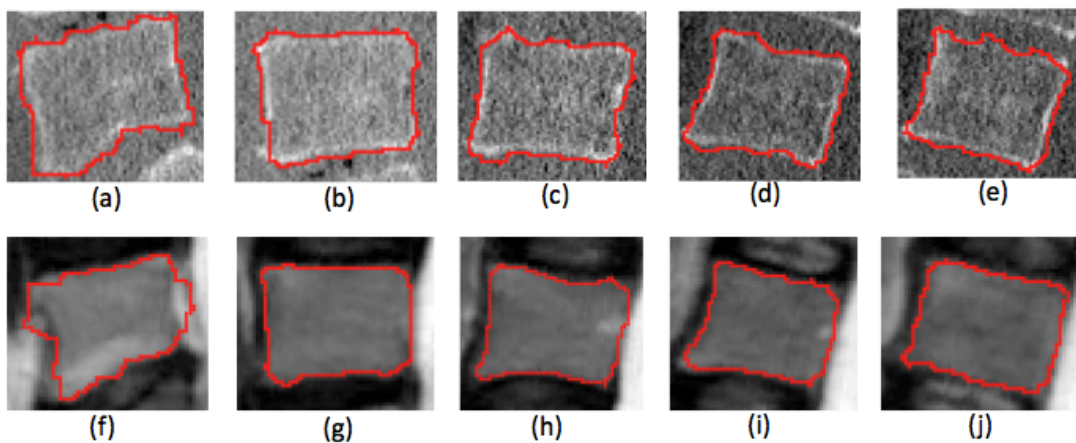
Figure 5.6: Automatic segmentation of vertebrae (in red) L1 to L5 in CT (a)-(e) and L1 to L5 in MR (f)-(j) of the same patient using an square distance map with $\alpha = 0, \beta = 3, \gamma = 4, \rho = 1.25$

5.5.2 Discussion of the classification

The results of the classification of the degeneration are presented in Table 5.6. These results can be considered accurate enough since the inter-observer specificity and sensitivity are in the same range as those achieved with the proposed algorithm. Moreover, the inter-observer variability and the results from the proposed method were compared using the score test. The p-values obtained with this test were always above 0.97,

meaning that is not possible to ensure that both values are not equal. However, the WCI intervals were rather wide, reviling that the number of cases is small.

In overall, the proposed method achieved accurate results with no subjectivity. And, although the CI ranges are wide, showing that more cases are required, the lowest value of all of the intervals is still above 60%, which proves its reliability. Notice that the observers' interval are narrower than the automatic method because they were obtained using the whole dataset instead of the testing set. The robustness of the classifier was also proved by checking that it always kept the error within ± 1, meaning that if the real degeneration grade was 3, it never chose 1 or 5.

The selection of the classifier was based on their performance in the training dataset. Observe that the difference given by initialising the optimisation with the Swarm optimisation is due to using a gradient-based optimiser. In particular, the optimisation technique used for the NN was stochastic gradient descent. This technique has the drawback of getting stuck in local minima. Thus, the swarm optimisation decreases the likelihood of this to happen by initialising the optimisation search close to the global minima. However, employing other optimisers such the quasi-Newton may also solve this issue.

Observe, that the current method for classification does not require highly accurate segmentation, because the type of features are statistics over a normalized intensity and the region of the nucleus position is an ellipse approximation. Furthermore, this type of features is robust against different type of MRI machines and resolutions. Since, the current database did not have images from different machines, this robustness was evaluated by reducing the in-plane resolution of all the images to be $1.5mm \times 1.5mm$ and running all the experiments. Although the segmentation slightly changed (Fig. 5.7), the classification remained exactly the same.

5.5.3 Limitations

A limitation of the method is the need of user interaction for selecting the centre of an ellipse. This step could be automatised by detecting the centre of the intervertebral disc using one of the methods in the literature [27, 28, 161, 162].
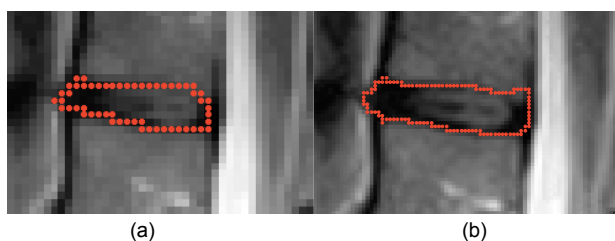
Figure 5.7: Comparison of the Snake segmentation with Low (a) and normal resolution (b).

Another limitation is the low number of cases, which implied large confidence intervals in the classification results. Although, this issue hinders the evaluation of the method, the minimum values of the confidence intervals were not extremely low (above 60%).

In addition, the type of grading system could be considered as a limitation of the method. Pfirrmann degeneration grading has been extensively used in research and requires the standard T2-weighted MR image. The main drawback is the selection of a gold standard for evaluating the classification methods, which are commonly subjective because of the vague definition of the different degrees of degeneration. In order to solve this issue, the gold standard was selected as the most voted value of the classification provided by 3 experts. However, there exist new grading systems that define the degrees in a different manner in an attempt to be more objective and they could be a choice for future research work [209, 210].

The last limitation is the image modality. Although, there exist correlation between other type of image modalities, such as T1-ρ or T2*, and the Pfirrman's grading system [226, 227], the standard T2-weighted was employed because of its direct relationship, since Pfirrmann was inspired from this modality. In addition, T2-weighted is still the standard modality in many hospitals.

5.6 Conclusions

This chapter presents an automatic and accurate method to classify the IVD's degeneration based on the ellipticity of the IVD and the intensity in the nucleus pulposus.

This information was extracted from a previous segmentation of the intervertebral disc using Active Contour models and Fuzzy C-means.

This method opens the way to a better quantification of the IVD degeneration that could help physicians in large-scale population studies and also in the automation of patient-specific techniques used in personalised medicine. Moreover, the proposed automatic IVD segmentation method provides numerical information about the biological and biomechanical features of the tissue even when these correlations with the MR signals are not fully understood.

Chapter 6

Rebalanced Multi level Component Analysis (R-MLCA):

In this chapter, we address the following casualty dilemma: The classification of an object tends to be more precise when its proper segmentation is provided. But, on the other hand, the segmentation of an object is more accurate when having extra information that can be computed with a classification method, such as the stage of a disease. Thus, an important objective of this thesis is to be able to create a framework that exploits the commonality between classification and segmentation in order to provide a better performance for both applications. In the literature, there exist a group of methods to perform this tasks using multi-linear techniques. However, they do not have all the properties that are desired, as it will be mentioned in the Motivation. Therefore, this chapter provides with the mathematical base of a new type of multi-linear technique, the rebalanced multi-linear component analysis (R-MLCA). This technique permits the creation of SSMs and SAMs with multiple factors, such as the stage of a disease or the inter-subject variability. This information is employed to achieve different levels of modes of variation. For instance, assume an SSM is going to be created using the R-MLCA with a database of vertebrae in different spinal positions and with different stage of scoliosis. The first level would comprise the modes of variation corresponding to changes in the spinal position, the second one would comprise the modes of variation corresponding to the additional differences in disease stage, and the third one

would encode the inter-subject variability.

R-MLCA allows SSMs and SAMs to achieve more accurate segmentations and the possibility to classify the segmented objects according to these factors.

6.1   Motivation

Statistical shape models (SSM) and Statistical appearance models (SAM) were developed to incorporate knowledge on the statistical variability of shape and appearance of the object of interest into image analysis [32]. This type of models provides information on the normal variability of a population. It also allows the generation of new object instances (s) that resemble the studied ones through the linear combination of a group of modes of variation ($\mathbf{\Phi}$) and the mean across the population ($\bar{s}$):

$$s = \bar{s} + b\mathbf{\Phi} \tag{6.1}$$

These models only consider one factor, which is usually the cross-subject variability. Thus, when facing hierarchical, or nested, data structures, SSMs and SAMs do not consider the different factors on which the data is dependent. This drawback is evident in applications of different areas, such as: **Cardiac modelling** where it may be necessary to model the variability stemming from both subject and cardiac phase. **Brain modelling** in which it might be interested to obtain the variation across subjects, ageing, and a specific disease or disorder, such as dementia, in order to compute the factor risk of developing such disorder. **Bone modelling** where it could be desirable a model that depends on the variability across subjects, degree of osteoporosis and ageing, so that the relationship age and osteoporosis for specific patients is encoded.

The generation of an SSM or SAM involves generally a dimensionality reduction of the original object descriptors to a reduced number of principal modes. For this purpose Principal Component Analysis (PCA) is commonly used, because it contains a series of properties that are desirable for the method and the obtained modes. In the case of a Multi-linear SSM or SAM, it would be appealing to achieve equivalent properties:

1. **Robustness to unbalanced and missing data:** The construction of models with different factors requires a database stratified according to their factor values. The method should be robust against unevenly distributed data among these groups or even missing groups.

2. **Orthogonality and independence:** The model should ensure orthonormality between the modes of each factor and independence between the different factors.

3. **Close-form solution:** The extraction of the modes of variation as well as the reconstruction procedure of a given object should have a close-form solution.

4. **Optimal truncation:** The selection of a subgroup of modes of variation (Φ) from the model should yield the best lower multilinear rank approximate [228]. This is an important property that enables the truncation of Φ by removing the least significant modes, typically considered noise.

In the literature, the multilinear models have been described in a multiplicative manner, so that the modes of variation (Φ) are stored in a tensor of order L+1, being L the number of factors. The reconstructed object is thus expressed as

$$s = \Phi \times_2 \boldsymbol{b}_{f_1} \cdots \times_{L+1} \boldsymbol{b}_{f_L} \tag{6.2}$$

where $\boldsymbol{b}_{f_a}$ are the model parameters of each factor $a = 1 \ldots L$. These models are constructed using a tensor-based learning technique on the data, such as high order singular value decomposition (HOSVD) ([229], [230]), multilinear subspace analysis with missing values (M^2SA) [231], bayesian tensor decomposition (BTD) [232] or simultaneous tensor decomposition and completion (STDC) [168], among others.

However, none of these methods simultaneously guarantees the four desired properties. Thus, different extensions have been proposed in the recent years to solve specific issues. For instance, in the case of bilinear models, Mpiperis *et al.* [193] proposed an extension of the HOSVD technique to handle the case of missing and unbalanced data. Vlasic *et al.* [233] dealt with the missing data issue by formulating the problem into a probabilistic framework that was solved using probabilistic PCA (PPCA). Another solution for the case of bilinear models and when one factor is periodic was proposed

by Figueras *et al.* [234], where the bilinear coefficients were approximated by Fourier functions allowing the recovery of missing temporal phases in the cardiac cycle.

Lecron *et al.* [235] proposed to employ an additive method, based on Multi-level component analysis (MLCA) [236], which handles all the previous properties. However, the method was only formulated for a bilinear case, and with a notation too specific to their particular problem. A more systematic reformulation of their method for multilinear models would be introduced in section 6.2. In addition, they did not provide any method to reconstruct or classify new input shapes.

In addition, the method proposed by Lecron *et al.*does not handle an important issue. In many databases the distribution of cases with different combination of factors may not be a faithful representation of their distribution in the real population. A sample scenario is having two datasets of human spines, one with thoracic and lumbar vertebrae and another with only lumbar ones. If not correctly addressed, the model rising from the two databases together will give more importance to the lumbar vertebrae, since there are more available cases.

A straightforward solution is to use only a balanced subsample. But this would produce a reduction of the statistical significance of the estimated model. In general, the available data is scarce and expensive, and there could be even cases with missing combination of factors in the sample. The formulation of MLCA employed by [235] ignores this effect. Its direct application to an unbalanced data would introduce some bias, giving more relevance to some factor values, not justified by their abundance in the population.

Herein, the MLCA is revised, taking into consideration that the distribution of cases into different factors in the training dataset may not properly represent their real distribution in the population (Section 6.2.1). For clarity, the new method is named rebalanced MLCA (R-MLCA). Although, both methods coincide for balanced datasets it is shown that the R-MLCA improves the performance of the original MLCA for unbalanced ones. This technique was used to create rebalanced multi-level statistical shape models (R-MLSSM). In addition, the derivation of a method to reconstruct unseen shapes depending on the available information (Section 6.2.4) and a classification

algorithm that employs the R-MLSSM, embedded in a Bayesian framework (Section 6.2.5), are provided. In order to evaluate the model and both the reconstruction and classification methods, it was compared the reconstruction error and the specificity and sensitivity of the classification between the R-MLSSM and the standard SSM in different experiments (Section 6.3). The results of these experiments are shown in Section 6.4. Lastly, the discussion and conclusions are in Section 6.5 and 6.6.

6.2 Method

6.2.1 Multi-linear model construction

This section introduces the rebalanced MLCA and its use to build statistical shape and appearance models. For simplicity, we will refer only to shape models, named rebalanced multi-level SSM (R-MLSSM), along the paper as all experiments have been carried out on shapes.

Consider a dataset of K cases, each of them, $i \in [1, K]$ described by a N-dimensional vector $\boldsymbol{s}_i$. For point distribution models, $N = d \times P$, where d is the dimension of the space, and P the number of points.

The cases are also classified according to a set of factors $\{f_1, f_2, \ldots, f_L\}$, with each f_a taking q_a different values. Thus, each case i is also described by a vector of factor values, $\{(f_1(i), \ldots, f_L(i)\}$. These factors are organized hierarchically in L levels. Each level a is formed by all factors included in the previous level, $a - 1$, and the factor a. Thus, we will denote by $F_a = \{f_1, f_2, \cdots, f_a\}$ the factor values involved in the hierarchy level a. In general, the last hierarchy level L denotes the patient variability within each group. Therefore, this last hierarchy level contains individual objects and it will be treated differently in various steps of the derivation of the R-MLCA.

Let us define the set of all cases that are used to create the model as $\mathcal{C}$. Then, for each F_a, its corresponding subset of cases is denoted $\mathcal{C}_{F_a} = \{i \in \mathcal{C} | F_a(i) = F_a\}$, with cardinality $K_{F_a} = n(\mathcal{C}_{F_a})$. If $F_0 = 0$ is considered, then $\mathcal{C}_{F_0} = \mathcal{C}$ and $K_{F_0} = K$.

Note that it is not required that all the combinations of factor values are covered by

the cases, and that more than one case may have the same combination.

The multi level SSM (MLSSM) represents each case $\boldsymbol{s}_i$ as:

$$
\begin{aligned}
\boldsymbol{s}_i &= \boldsymbol{\phi}^{(0)} + \boldsymbol{b}_{F_1(i)}^{(1)} \boldsymbol{\Phi}^{(1)} + \boldsymbol{b}_{F_2(i)}^{(2)} \boldsymbol{\Phi}^{(2)} + \cdots + \boldsymbol{b}_{F_L(i)}^{(L)} \boldsymbol{\Phi}^{(L)} + \boldsymbol{e}_i \\
&= \sum_a \boldsymbol{b}_{F_a(i)}^{(a)} \boldsymbol{\Phi}^{(a)} + \boldsymbol{e}_i = \tilde{\boldsymbol{s}}_i + \boldsymbol{e}_i \\
&\text{with} \quad \boldsymbol{b}_{F_0(i)}^{(0)} = 1 \quad \text{and} \quad \boldsymbol{\Phi}^{(0)} = \boldsymbol{\phi}^{(0)}
\end{aligned} \tag{6.3}
$$

where $\tilde{\boldsymbol{s}}_i$ are the instances of the model, $\boldsymbol{\phi}^{(0)}$ is a constant vector, the matrices $\boldsymbol{\Phi}^{(a)}$ are formed by the modes of variation corresponding to each level a, and $\boldsymbol{b}_{F_a(i)}^{(a)}$ are the corresponding model parameters, which only depend on the factors associated to its level, $F_a(i) = \{f_1(i), f_2(i), \cdots, f_a(i)\}$, and they are independent of the rest of them. In addition, each $\boldsymbol{\Phi}^{(a)}$ is orthonormal and the model parameters $\boldsymbol{b}_{F_a(i)}^{(a)}$ are uncorrelated within its level and between the different levels.

In [236], the MLCA is described as the least square problem:

$$
E = \sum_{i \in \mathcal{C}} \|\boldsymbol{s}_i - \tilde{\boldsymbol{s}}_i\|^2 \tag{6.4}
$$

under the same constraints stated previously, so that

$$
\langle \boldsymbol{b}^{(a)} \boldsymbol{b}^{(c)} \rangle = 0 \qquad \forall a, c \in 0, \ldots, L \qquad \text{with} \qquad a \neq c \tag{6.5}
$$

Observe that, since $\boldsymbol{b}^{(0)} = 1$, this equation is implicitly imposing that each $\boldsymbol{b}^{(a)}$ has null mean. However, this formulation ignores the effect of having different group proportions in the training set as that in the real population. This means that if a training dataset contains K_{F_a} cases with a specific combination of factor values, for instance L1 vertebrae in a lumbar spine dataset, it is implicitly assumed that K_{F_a}/K is the probability of having L1 vertebrae not only in the dataset but also in the real population. In general, this may not be true, and the real probability α_{F_a} may be different to K_{F_a}/K. For the purpose of illustration, let us assume we want to construct a model of a vertebra, taking into account the position across the spine and the subject variability. Let also assume that we have two databases, one containing vertebrae of the

whole spine and another of only cervical vertebrae. This means that a model created using (6.6) will consider cervical vertebrae to be more likely to exist than thoracic or lumbar ones, which is not true in the human population. Thus, herein it was derived an extended version of the MLCA robust to unbalanced data, using partial results from the work in [236] and [237].

In a Gaussian setting, it is common to estimate the modes of variation and model parameters by minimising the cases and their approximation as instances of the model ($\tilde{\boldsymbol{s}}_i$):

$$E = \langle \|\boldsymbol{e}\|^2 \rangle = \langle \|\boldsymbol{s} - \tilde{\boldsymbol{s}}\|^2 \rangle \tag{6.6}$$

In the case of (6.6), the probability of each s_i is given by the probability of occurrence of each shape in the dataset, meaning $1/K$ for each x_i. Therefore, this value is a constant and can be neglected in the minimization process. However, in reality the probability of each x_i should be the probability in the real population. This probability, named $w_{F_{L-1}}$, is defined as the probability of a shape to have a specific combination of factors α_{L-1} in the real population divided by the number of patients with this combination in the training dataset, K_{F_a}:

$$E = \sum_{i \in C} w_{F_{L-1}(i)} \|\boldsymbol{s}_i - \tilde{\boldsymbol{s}}_i\|^2$$
$$w_{F_{L-1}} = \frac{\alpha_{F_{L-1}}}{K_{F_{L-1}}} \tag{6.7}$$

Observe that it is defined in terms of the proportions in the hierarchical level $L - 1$ instead of L. As previously explained, the last factor, f_L, identifies the subject, while $\alpha_{F_{L-1}}$ is the probability of finding a subject with factors values $f_1, \cdots, f_{L-1}$. It is also required the same constraints stated in (6.5). Observe, that the formulation presented by Timmermann [236] only coincides with the proposed formulation when the sample of K cases contains the same proportion of factors as in the real population. In other terms, $K_{F_{L-1}} = \alpha_{F_{L-1}} K$.

6.2.2 Derivation of the model

As stated in (6.5), a constraint of the model is that the parameters $\boldsymbol{b}_{F_a}^{(a)}$ are to be uncorrelated across the different levels. This allows a separation of the minimisation problem of (6.7) into a set of subproblems:

$$E^{(a)} = \sum_{i=1}^{K} w_{F_{L-1}(i)} \left\| \boldsymbol{s}_i - \boldsymbol{b}_{F_a(i)}^{(a)} \boldsymbol{\Phi}^{(a)} \right\|^2 \quad , \forall a \in 0 \dots L \tag{6.8}$$

In the article presented by [236], the readers can find a rigorous proof of this result for the energy presented in (6.6), which can be straightforwardly adapted for (6.7).

The new subproblems are still dependent to each other by their constraints. This dependency can be eliminated by creating a set of energies, whose unconstrained minimisation is equivalent to that of the constrained original problem. In order to find the new energies, the same procedure as stated in Appendix 1.B from [237] was employed. This procedure creates the equivalent set of energies by demonstrating that they provide the solution, which automatically hold all the restrictions specified in (6.5). The resulting energies are:

$$\tilde{E}^{(a)} = \sum_{i=1}^{K} w_{F_{L-1}(i)} \left\| \overline{\boldsymbol{s}}_{F_a(i)}^{(a)} - \boldsymbol{b}_{F_a(i)}^{(a)} \boldsymbol{\Phi}^{(a)} \right\|^2 \quad \forall a = 0, \dots, L \tag{6.9}$$

This set of energies employs the following set of group-wise means:

$$\left. \begin{array}{l} \overline{\boldsymbol{s}}_{F_a}^{(a)} = \dfrac{\sum_{i \in \mathcal{C}_{F_a}} w_{F_{L-1}(i)} \boldsymbol{s}_i^{(a)}}{\sum_{i \in \mathcal{C}_{F_a}} w_{F_{L-1}(i)}} \\[2ex] \boldsymbol{s}_i^{(a+1)} = \boldsymbol{s}_i^{(a)} - \overline{\boldsymbol{s}}_{F_a(i)}^{(a)} \end{array} \right\} \quad \forall a = 0, 1, \dots, L-1 \tag{6.10}$$

obtained recursively with

$$\boldsymbol{s}_i^{(0)} = \boldsymbol{s}_i$$

Observe that this group-wise means are robust against an unfaithful representation of the cases in the dataset and the real population.

In these expressions, it was employed all the data at each level a. However, the new energies only require the group-wise mean at each factor value. Therefore, the

problem may be compacted by taking into consideration that:

$$
\begin{aligned}
\tilde{E}^{(a)} &= \sum_{i=1}^{K} w_{F_{L-1}(i)} \left\| \overline{\boldsymbol{s}}_{F_a(i)}^{(a)} - \boldsymbol{b}_{F_a(i)}^{(a)} \boldsymbol{\Phi}^{(a)} \right\|^2 \\
&= \sum_{F_a} \left(\sum_{i \in \mathcal{C}_{F_a}} w_{F_{L-1}(i)} \right) \left\| \overline{\boldsymbol{s}}_{F_a}^{(a)} - \boldsymbol{b}_{F_a}^{(a)} \boldsymbol{\Phi}^{(a)} \right\|^2 \\
&= \sum_{F_a} \alpha_{F_a(i)}^{(a)} \left\| \overline{\boldsymbol{s}}_{F_a}^{(a)} - \boldsymbol{b}_{F_a}^{(a)} \boldsymbol{\Phi}^{(a)} \right\|^2
\end{aligned}
\tag{6.11}
$$

where

$$
\alpha_{F_a}^{(a)} = \sum_{i \in \mathcal{C}_{F_a}} w_{F_{L-1}(i)} \quad \forall a = 0, 1, \dots, L
$$

are the marginal probabilities for the corresponding factors.

Hence, the energy minimisation problem is finally defined as:

$$
\tilde{E}^{(a)} = \sum_{F_a} \alpha_{F_a}^{(a)} \left\| \overline{\boldsymbol{s}}_{F_a}^{(a)} - \boldsymbol{b}_{F_a}^{(a)} \boldsymbol{\Phi}^{(a)} \right\|^2 \quad \forall a = 1, \dots, L
\tag{6.12}
$$

with

$$
\phi^{(0)} = \overline{\boldsymbol{s}}_{F_0}^{(0)}
$$

. This energy is under the constraints that each $\boldsymbol{\Phi}^{(a)}$ is orthonormal. Thus, each individual energy may be minimised independently using weighted PCA [238].

6.2.3 Selection of the number of modes of variation

The modes of variation describe the normal variability of the population from the mean shape. However, they are estimated from a limited training set and part of these computed modes encode noise instead of useful information. Thus, it is common to retain a subset of the most relevant modes. In the case of the R-MLSSM, this selection must be performed at each level. The most common criteria is to select the group of modes that describes 95% of the total variation, given by the PCA eigenvalues. This, however, often overestimates the correct number of modes, producing over-fitting. Thus, it was used the Cattel's scree test [239] for this purpose. Although this test is subjective to the user, it is usually more robust than the standard 95% of the total variation.

6.2.4   Reconstruction process

A generative statistical model is characterized by the capacity to generate samples of the object described. Given a new case, s, not present in the training set, its best representation with the model parameters is named the reconstruction of the case, $\tilde{s}$. It is typically obtained by minimizing the quadratic difference between s and $\tilde{s}$:

$$b = \underset{b}{\operatorname{argmin}} \, \|s - \phi^{(0)} - b\Phi\|^2 = (s - \phi^{(0)})\Phi^{\mathrm{T}} \quad \text{and} \quad \tilde{s} = \phi^{(0)} + b^*\Phi. \quad (6.13)$$

where b^* is obtained by restricting each b_k, between $-3\sigma_k$ and $3\sigma_k$, with σ_k being the standard deviation of the mode k in Φ. This projection, in general, is considered to remove noise and spurious variations with respect to the normal variability of the object. This justifies the use of this reconstruction as a filter, for instance, in active shape model (ASM) [32].

For R-MLSSM, an analogous projection process can be obtained for the reconstruction of a new case.

$$b_c = \underset{b_{F_1}^{(1)}, \ldots, b_{F_L}^{(L)}}{\operatorname{argmin}} \left\| s - \phi^{(0)} - \sum_{a=1}^{L} b_{F_a}^{(a)} \Phi^{(a)} \right\|^2 \quad (6.14)$$

This minimisation problem may be solved by concatenating all the $b^{(a)}$ to create b_c, and the matrices of modes $\Phi^{(a)}$ to create Φ_c, and then, deriving the problem by the group of model parameters, b_c, achieving:

$$b_c = \underset{b_c}{\operatorname{argmin}} \, \|s - \phi^{(0)} - b_c\Phi_c\|^2$$

$$\text{with } b_c = (s - \phi^{(0)})\Phi_c^{\mathrm{T}}\big(\Phi_c^{\mathrm{T}}\Phi_c\big)^{-1} \quad \text{and} \quad \tilde{s} = \phi^{(0)} + b_c^*\Phi_c. \quad (6.15)$$

However, two different scenarios are distinguished for the reconstruction. In the scenario considered for equation (6.15), the factors corresponding to the new case have been implicitly considered as unknown. A second scenario appears when those factor values, $\{f_1, \ldots, f_{L-1}\}$, are known. In that case, the model parameters up to level $L-1$ can be the identified with the estimated ones in the model construction, $b^{(a)} = b_{F_a}^{(a)}$, for

$a = 1, \cdots, L - 1$. The solution to this problem is:

$$
\begin{aligned}
\boldsymbol{b}_{F_L}^{(L)} &= (\boldsymbol{s} - \tilde{\boldsymbol{s}}_{F_{L-1}}) \boldsymbol{\Phi}^{(L)\mathrm{T}} \text{ with } \tilde{\boldsymbol{s}}_{F_{L-1}} = \boldsymbol{\phi}^{(0)} + \sum_{a=1}^{L-1} \boldsymbol{b}_{F_a}^{(a)} \boldsymbol{\Phi}^{(a)} \\
\tilde{\boldsymbol{s}} &= \tilde{\boldsymbol{s}}_{F_{L-1}} + \boldsymbol{b}_{F_L}^{*(L)} \boldsymbol{\Phi}^{(L)}
\end{aligned}
\tag{6.16}
$$

This second scenario does not usually occur, it is the one implicitly assumed in the construction of the MLCA and R-MLCA. This assumption is related to the imposition of the model parameters until level $L - 1$ to be the same for two different shapes if the combination of factor values are the same. In general, this scenario appears when integrating external information. For instance, a clinician or an accurate automatic method can evaluate the degeneration degree of an intervertebral disc (IVD) and provide this information in order to improve the IVD segmentation accuracy.

6.2.5 Classification

In the scenario of having a new shape with unknown factor values, F_{L-1}, there exists the question of whether they could be estimated from the statistical shape model. This issue is essentially a classification problem, which can be solved in two different manners: the model parameters are used as features in a standard classifier, such as neural network, Logistic Regression or Support vector machine [24–26, 29, 30]. The second option is to use the SSM or SAM as classifier [117]. In general, PCA does not produce vectors that are optimal for the separation of classes, and therefore, the second option has not been fully explored in previous works. However, since this paper aims at developing a new type of SSM and exploiting its possibilities, it seems more appropriate to follow the second type. In this paper, we propose to solve the probability problem by the maximum a posteriori probability in a Bayesian framework:

$$
F_{L-1}^* = \operatorname*{argmax}_{F_{L-1}} P(F_{L-1}|\boldsymbol{s})
\tag{6.17}
$$

where

$$
P(F_{L-1}|\boldsymbol{s}) \propto p(\boldsymbol{s}|F_{L-1}) P(F_{L-1})
$$

with a proportionality factor independent of the factor values. The prior probabilities, $P(F_{L-1})$, are the expected proportions considered in the model construction, $\alpha_{F_{L-1}}$. The likelihood $p(\boldsymbol{s}|F_{L-1})$ is the probability distribution with the combination of factors values $\{f_1, \ldots, f_{L-1}\}$. Given the R-MLSSM properties, this likelihood follows a multi-dimensional Gaussian distribution. Thus,

$$p(\boldsymbol{s}|F_{L-1}) = \mathcal{N}\left(\boldsymbol{s}_{F_{L-1}}, \Sigma^{(L)}\right)$$
$$\text{with} \quad f_a = 1, \ldots, q_a \quad \forall i = 0, 1, \ldots, L-1 \tag{6.18}$$

The covariance matrix is usually computed as $\boldsymbol{\Phi}^{(L)} \boldsymbol{D}^{(L)} \boldsymbol{\Phi}^{(L)\mathrm{T}}$, with $\boldsymbol{D}^{(L)}$ the diagonal matrix collecting the variances of every principal mode. However, this form is commonly not full rank, since the number of degrees of freedom in the input representation, $\boldsymbol{s}$ multiplied by the dimensions is usually much higher than the number of training cases. A non-degenerate positive-defined covariance matrix can be estimated by the method proposed in [108]:

$$\Sigma^{(L)} = \boldsymbol{\Phi}^{(L)} \boldsymbol{D}^{(L)} \boldsymbol{\Phi}^{(L),T} + \sigma_\epsilon \left(I - \boldsymbol{\Phi}^{(L)} \boldsymbol{\Phi}^{(L),T}\right) \tag{6.19}$$

The standard deviation σ_ϵ corresponds to that of the residual modes of variation, and it should be smaller than the standard deviation of the last principal mode, $0 < \sigma_\epsilon < \sigma_K^{(L)}$, with $\sigma_K^{(L)}$ being the lowest standard deviation. In general, this value is relatively small, and in the experiments, it was found that a good candidate was $\sigma_\epsilon = \sigma_K^{(L)}/2$.

In case it is necessary to estimate only a subset, $\mathcal{S} \subset [1, L-1]$, of factors, $F_{\mathcal{S}} = \{f_c \mid c \in \mathcal{S}\}$, the corresponding probabilities can be obtained by marginalising over the non-desired ones:

$$P(F_{\mathcal{S}}|\boldsymbol{s}) = \sum_{F_{\overline{\mathcal{S}}}} P(F_{\mathcal{S}}, F_{\overline{\mathcal{S}}} \mid \boldsymbol{s}), \tag{6.20}$$

where the summation runs through all the combination of values for the factors in the complementary set $\overline{\mathcal{S}} = [1, L-1] \setminus \mathcal{S}$.

In the case of the standard SSM, an analogous classification procedure could be employed. Each combination of factor values defines a class for which a corresponding SSM is to be built. Similar to using the R-MLSSM, the probability for each class would

have a corresponding mean. However, the covariance matrix $\Sigma^{(L)}$ in the R-MLSSM is common for all the classes, estimated from the whole dataset, whereas in the case of individual SSMs, each class has its own covariance matrix computed independently. This implies that the estimation with individual SSMs requires larger datasets for a reliable estimation.

Observe that if the training database does not contain a single case with specific combination of factor values, it will be not possible to compute the probability for those combinations. For instance, having a training database of IVDs with no cases of degeneration grade three at the spinal position L1-L2 precludes the model from considering such combination. However, the variation in shape due to common medical related factors, such as the stages of a disease, the grade of fractures, or the stage of other disorders, is usually continuous. Thus, it is possible to approximate the missing shapes as the average among its neighbouring shapes. For instance, in the previous case scenario with no cases of level three of IVD degeneration at the spinal position L1-L2, a synthetic shape can be created by averaging the IVD mean shapes at T12-L1 and L2-L3 with degeneration 3 and L1-L2 with grades 2 and 4.

However, the variation in shape due to some factors is expected to be progressive. This is the case of the IVD degree of degeneration, the vertebral fracture severity, or the vertebral position along the spine. In those cases, it is possible to approximate the mean of the missing class by the average between the mean of the classes corresponding to the previous and next factor values. In the case scenario of an IVD dataset with no cases of degeneration grade 3 at L2-L3, a synthetic shape can be created by averaging the IVD mean shapes at L1-L2 and L3-L4 with degeneration degree 3.

6.3 Experiments and Data

6.3.1 Data

Two databases of meshes were considered. They were obtained from semi-automatic segmentation of several CT and MRI datasets. The total number of vertebrae is 405, separated into 15 cases for each of the 12 thoracic vertebral positions and 45 cases

for each of the 5 lumbar positions. These vertebral meshes were segmentations of 15 thoracic and lumbar spine CTs from the spine web [199] and 30 lumbar spine CTs from the project MySpine [34].

The total number of IVDs is 1280 IVDs, 256 for each lumbar position. The total number of IVDs per position and degree of degeneration following the Pfirrmann classification [158] is presented in Table 6.1. These IVD meshes were segmentations of 256 patients from the project MySpine [34].

Table 6.1: number of IVDs per position and degree of degeneration.

Lumbar	Degeneration grade				
segments	I	II	III	IV	V
L1-L2	22	95	116	21	2
L2-L3	28	97	101	28	2
L3-L4	39	87	87	39	4
L4-L5	27	46	66	96	21
L5-S1	12	43	51	115	35
Sum	128	368	421	299	64

The point correspondence, required to create the SSMs, was achieved using a free form deformation technique to adapt a template mesh to all the ground-truth meshes. To reduce the dependency of the initial shape, the process was iteratively repeated changing the template by the updated mean of all the meshes at each iteration [109].

6.3.2   Models

The following models are used for the evaluation of the proposed R-MLCA technique:

- **Complete bilinear model of Vertebrae**, the whole vertebra database is used. The first factor is the position across the spine and the second one being the subject.

- **Complete trilinear model of IVDs**: The whole database is employed. The first factor is the position across the spine, the second factor is the degree of degeneration and the third factor is the subject.

- **Non-complete bilinear model of Vertebrae**: This model contains the whole dataset except those in the same spinal position as the case being evaluated. For

instance, if the experiment is performed in L1 vertebra the R-MLSSM will not contain a single case of L1. The first factor is the position across the spine and the second one being the subject.

- **Non-complete trilinear model of IVDs**: This model contains the whole dataset except those in the same spinal position and degeneration as the case being evaluated. For instance, if the experiment is performed in L1-L2 IVD with degeneration grade 3, the R-MLSSM will not contain a single case of L1-L2 IVD with degeneration 3. The first factor is the position across the spine, the second factor is the degree of degeneration and the third factor is the subject.

- **Global Model:** This model is constructed using all the shapes, vertebrae or IVDs altogether, regardless their position or degeneration grade. The result was a unique model for IVDs and another for vertebrae.

- **Positional Model:** These models were built by stratifying the datasets according to the spinal position. This results in 17 models for the thoracic and lumbar vertebrae and 5 for the lumbar IVDs.

6.3.3 Evaluation of the models

The two applications depicted in section 6.2: reconstruction (section 6.2.4) and classification (section 6.2.5) were evaluated using a leave-one-out cross validation in the following set of experiments:

- Reconstruction and classification of both datasets in a leave-one-patient-out scheme using both the vertebral and the IVD *R-MLSSM*.

- Reconstruction of both datasets in a leave-one-group-out scheme using the *R-MLSSM with known factor values*. In this experiment, the factor values until the level $L - 1$ were provided and not estimated.

- Reconstruction and classification of both datasets in a leave-one-group-out scheme using a *Non complete R-MLSSM*. In this experiment, one level, a is selected.

Then, all the shapes that contain the same factor values on this level as the shape
to be reconstructed were removed in the model construction step.

- Comparison of the specificity and sensitivity of the classification using the positional, global, Non-complete R-MLSSM and R-MLSSM models of both IVDs and vertebrae.

As explained in the last paragraph of section 6.2.5, the classification in the case of
the *Non complete R-MLSSM* was performed by computing the missing average shapes
as the mean of their neighbouring shapes.

In addition, two other experiments were performed.

- **Evaluation of rebalancing the model:** A group of 100 patients were selected
from the IVD database maintaining the distribution of the number of cases with
each degeneration grade at each position as homogeneous as possible. Subsequently, a model was constructed and evaluated using the whole 256 patients of
the database.

- **Uncorrelation of the modes of variation:** An important property of the R-MLSSM is that the modes of variation at each level are uncorrelated to the modes
of the other levels. Although, this property was imposed in the constraints defining the model, we propose an experiment to test it. The evaluation of the uncorrelation was carried out by computing the covariance matrix between the model
parameters at different hierarchy levels. These matrices should have all their values equal to zero. Thus, their maximum value was used for the evaluation.

6.3.4   Point Correspondence

The point correspondence, required to create the SSMs, was achieved using a free
form deformation technique to adapt a template mesh to all the ground-truth meshes.
To reduce the bias, the process was iteratively repeated changing the template by the
updated mean of all the meshes at each iteration [109].

6.4   Results

6.4.1   Parameters Selection

Retained number of modes: 4, 4 and 20 at each level in the R-MLSSM of IVDs, and, 5 and 25 in the vertebral R-MLSSM.

Number of landmarks: 1200 for each IVD and 4000 for each vertebra.

Number of shapes: 1280 IVDs, 280 at each lumbar position. 405 vertebrae, 15 at each thoracic position and 45 at each lumbar position.

6.4.2   Reconstruction Error

Fig. 6.1 shows the reconstruction error, measured as the mean Euclidean point to point distance, between the ground truth meshes of each of the 1280 IVDs (a) and 405 vertebrae (b) and their reconstructions. This process was performed in a leave-one-patient-out basis for three types of models: two standard SSMs and the R-MLSSM. The latter was used with two different reconstructions scenarios: providing all the factor values of the case that is reconstructed, named *R-MLSSM with known factor values*, and without having them, named *R-MLSSM*. This figure also presents the reconstruction error of the *Non-complete R-MLSSM model*, where all the cases with the same factor values as the one being reconstructed (same position and degeneration for IVDs, and same position for vertebrae) were not included.

Fig. 6.3 shows a comparison between four reconstructed vertebrae with the R-MLSSM from random patients at positions T2, T7, T11, L5 and the original shapes.

Table 6.2 and 6.3 show the mean, percentile 95 (95-p) and maximum value of the vertebrae and IVD reconstruction error, respectively. The number of modes of variation was given by the scree test (Section 6.2.3).

Since the database contains 15 cases of thoracic spines and 45 cases of lumbar spines, the positional model of the thoracic vertebrae have only 14 modes of variation. Thus, the reconstruction error using the positional model does not highly improve when the used number of modes approaches 19 (14+5 modes from the first level).
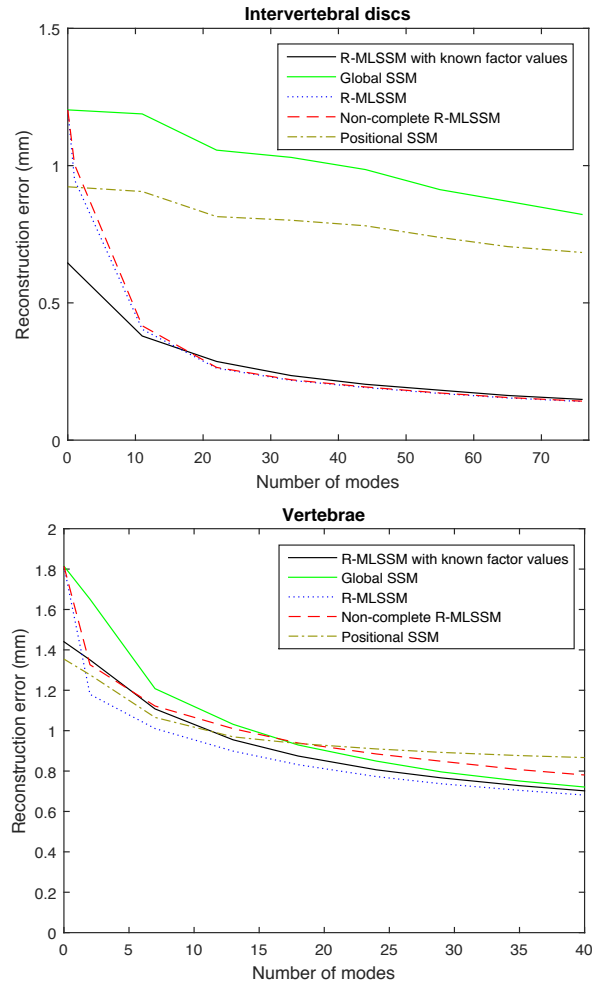
Figure 6.1: Reconstruction error with respect to the number of modes of variation for IVDs and vertebrae using a leave-one-out validation. The *positional SSM* contains one model for each spinal position (5 for IVDs and 17 for vertebrae). In the case of the *R-MLSSM*, the number of modes were given to each level in increasing order, until reaching the selected retained number of modes (Section 6.2.3). The *R-MLSSM with known factor values* corresponds to the reconstruction for which the position or position and degeneration were provided. *Non-complete R-MLSSM* curve shows the mean error achieved with models that do not contain shapes with the same position or position and degeneration, as the one being reconstructed.

Table 6.2: Mean, percentile 95 (95-p) and maximum vertebral reconstruction error at each spinal position with 5 and 25 modes of variation for the first and second level, respectively. These values were selected using the scree test (Section 6.2.3).

Error measures	T1	T2	T3	T4	T5	T6	T7	T8	T9
Mean (mm)	0.74	0.46	0.43	0.51	0.55	0.54	0.56	0.58	0.54
95-p (mm)	1.74	0.91	0.82	1.04	1.10	1.05	1.09	1.15	1.01
Maximum (mm)	3.28	1.94	2.24	2.21	2.03	2.24	2.46	1.86	3.32
Error measures	**T10**	**T11**	**T12**	**L1**	**L2**	**L3**	**L4**	**L5**	**Global**
Mean (mm)	0.64	0.70	0.76	0.81	0.81	0.83	0.85	0.93	0.73
95-p (mm)	1.23	1.43	1.54	1.67	1.62	1.72	1.72	1.90	1.57
Maximum (mm)	2.83	2.91	3.50	3.70	3.53	3.59	3.42	4.29	3.18

Table 6.3: Mean, percentile 95 (95-p) and maximum IVD reconstruction error at each spinal position with 4, 4 and 20 modes of variation for the first, second and third level, respectively. These values were selected using the scree test (Section 6.2.3). The positions go from L1-L2 to L5-S1.

Error measures	L1-L2	L2-L3	L3-L4	L4-L5	L5-S1	Global
Mean (mm)	0.33	0.31	0.30	0.35	0.41	0.34
95-p (mm)	0.47	0.41	0.44	0.51	0.62	0.50
Maximum (mm)	0.84	0.72	0.72	0.85	0.97	0.82

This issue, caused by having a low number of cases, does not occur when using the *R-MLSSM*, because each level is constructed with the whole database.

In the case of the IVDs, some groups of position and degeneration were too small to create an SSM. In contrast, the R-MLSSM with three hierarchical levels is able to acquire the information of the degeneration at each position and provide much lower reconstruction error than the global or the positional models. This second advantage was further tested using a *Non-Complete R-MLSSM*. In the case of the vertebrae, where the experiment is done eliminating all the shapes with the same spinal position, the error was of more important (Fig. 6.1) than in the case of the IVDs where, only those with the same position and degeneration were excluded. However, this second scenario is more common in the reality. For instance, vertebral shapes are mostly extracted from medical images. Thus, these databases contain similar amount of vertebrae at each spinal position. However, vertebral fractures are not very common and a database with fractures at each spinal position is rare [240].

Observe that the difference between the reconstruction using the *R-MLSSM* and

R-MLSSM with known factors is that the first modes of variations of the *R-MLSSM* are used to estimate the correct mean shape at each level, whereas in the *R-MLSSM with known factors*, these means are provided. Thus, the *R-MLSSM* curve is shifted towards the left direction, respect to that of the *R-MLSSM with known factors*, as many modes as used to estimate the first levels shapes. This advantage of having already selected the mean shape is also shared when using the *positional SSM*.

6.4.3   Classification

The results of the classification are presented in Tables 6.4, 6.5 and 6.6. The specificity and sensitivity of the classification using R-MLSSM was compared with that obtained by employing the same method presented in Section 6.2.5 but using a standard SSM for each spinal position (Spe/Sen Positional SSM in the tables) or an SSM for each degree of degeneration. In addition, the three tables show the classification of the spinal position or degeneration using a non-complete R-MLSSM. In this last experiment, the mean shape of the group of shapes that is missing was estimated by the average of the group-wise means of its two neighbouring positions.

For the sake of completeness, the sensitivity and specificity are defined below:

$$\text{Specificity(Spe)} = \frac{\text{TN}}{\text{TN + FP}} \quad \text{Sensitivity(Sen)} = \frac{\text{TP}}{\text{TP + FN}} \tag{6.21}$$

where TP, TN, FP and FN are the number of true positives, true negatives, false positives and false negative, respectively.

Table 6.4: Specificity and Sensitivity of the classification of the whole database (1280 IVDs) according to their degree of degeneration (deg: I to V) using a leave-one-out cross validation. The table also shows a comparison among the R-MLSSM, Non-complete R-MLSSM (NC-R-MLSSM) and using a single SSM per each position.

Classification Measures	I	II	III	IV	V	Global
Spe R-MLSSM	78.3%	100.0%	94.7%	100.0%	100.0%	83.9%
Sen R-MLSSM	40.0%	84.6%	44.4%	35.1%	62.9%	62.9%
Spe Degeneration SSM	55.5%	61.5%	57.4%	60.7%	91.2%	63.4%
Sen Degenration SSM	40.7%	26%	25%	35.9%	46.9%	35.2%
Spe NC-R-MLSSM	34.7%	65.4%	42.2%	76.4%	86.1%	54.4%
Sen NC-R-MLSSM	36.0%	19.8%	28.3%	11.3%	52.9%	23.0%

Table 6.5: Specificity and Sensitivity of the classification of the whole database (1280 IVDs) according to their lumbar position (L1-L2 to L5-S1) using a leave-one-out cross validation. The table also shows a comparison among the R-MLSSM, Non-complete R-MLSSM (NC-R-MLSSM) and using a single SSM per each position.

Classification Measures	L1-L2	L2-L3	L3-L4	L4-L5	L5-S1	Global
Spe R-MLSSM	100%	100%	99.8%	99.4%	99.8%	99.8%
Sen R-MLSSM	100%	100%	96.9%	97.7%	100%	98.9%
Spe Positional SSM	100%	100%	99.8%	99.4%	99.4%	99.7%
Sen Positional SSM	100%	100%	95.9%	97.3%	100%	98.5%
Spe NC-R-MLSSM	99.0%	90.7%	94.7%	98.9%	100%	96.6%
Sen NC-R-MLSSM	57.7%	100%	96.2%	96.1%	88.5%	87.7%

Table 6.6: Specificity (Spe) and Sensitivity (Sen) of the classification of the vertebra datasets according to their spinal position using a leave-one-out cross validation. The table also shows a comparison between the R-MLSSM, Non-complete R-MLSSM (NC-R-MLSSM) and using a single SSM per each position.

Measures	T1	T2	T3	T4	T5	T6	T7	T8	T9
Spe R-MLSSM(%)	100	99.5	99.5	99.7	99.7	100	100	100	100
Sen R-MLSSM(%)	100	93.3	86.7	86.7	93.3	100	100	100	100
Spe Positional SSM(%)	100	99.3	99.5	99.7	99.7	100	100	100	100
Sen Positional SSM(%)	100	93.3	80.0	86.7	93.3	100	100	100	100
Spe NC-R-MLSSM(%)	100	97.0	98.2	98.8	93.6	98.2	94.1	95.4	98.2
Sen NC-R-MLSSM(%)	73.3	80.0	80.0	66.7	66.7	86.7	73.3	80.0	60.0

Measures	T10	T11	T12	L1	L2	L3	L4	L5	Global
Spe R-MLSSM(%)	100	100	100	99.1	99.3	98.3	99.3	99.7	99.7
Sen R-MLSSM(%)	100	100	86.7	95.6	91.1	91.1	93.3	100.0	94.2
Spe Positional SSM(%)	100	100	100	99.1	98.3	98.3	99.7	99.3	99.6
Sen Positional SSM(%)	100	100	86.7	95.6	93.3	86.7	91.1	100.0	93.9
Spe NC-R-MLSSM(%)	98.8	100	95.2	99.2	90.2	93.9	94.3	100	96.7
Sen NC-R-MLSSM(%)	53.3	80.0	93.3	77.8	61.1	61.2	55.6	44.4	72.3

The results show that the R-MLSSM is able to accurately classify the position of both vertebrae and IVDs. However, similarly to the reconstruction, the main advantage of this model is that it allows the classification of factors for which no representative exists or their number is very small. This is demonstrated with the *Non-complete R-MLSSM*. Notice that in the case of the *positional SSM*, a Non-complete version cannot be constructed, because of its own definition.

In the case of the *Non-complete R-MLSSM*, there were no mean shapes that represent the missing groups. However, the shape of both vertebrae and IVDs varies continuously across the position and across the degree of degeneration. Thus, these

mean shapes can be approximated by computing the average of the neighbouring mean shapes or by performing an extrapolation when the missing shapes were the first or the last one. This interpolation and extrapolation procedures are less accurate for shapes with particular features as the L5. Thus, the classification of the L5 and the L4 (that was estimated using L3 and L5) were not as accurate as the rest of the vertebrae.

In the case of the IVDs, although its shape is affected by the degeneration, this influence is smaller than the inter-subject variability. This means that the reconstruction improved by taking the degeneration into account, but the classification results are rather poor. Thus, a proper classification of the degeneration grade cannot be attained using solely shape information. This statement complies with Pfirrmann's criterion [158] that remarks the importance of the nucleus pulposus intensity in T2-weighted MRI to grade the degeneration.

On the other hand, the IVD and vertebral shape variation caused by the spinal position is sufficiently large to allow a precise classification.

6.4.4 Influence of the rebalancing in the MLCA

As shown in Section 6.2.1, it is possible to construct a model, for which the proportion of cases with different factors in the population is known and different from the proportion of cases with these factors in the training sample. In order to test the improvement of this rebalanced model, a subset of 100 patients' IVDs were selected, trying to maintain the number of cases across the different positions and degenerations as uniform as possible. Then, MLSSM with and without rebalancing were constructed. The rebalancing was performed to maintain the proportions observed in the complete dataset, shown in Table 6.1. The reconstruction error obtained from each of the two models was evaluated in a leave-one-out fashion using the complete dataset. Fig. 6.2 shows the higher accuracy attained by the rebalancing MLSSM.

6.4.5 Qualitative results

For visualisation purposes, this section only includes vertebrae images, since IVDs do not exhibit as visually evident characteristic features as vertebrae. Fig. 6.3 shows the
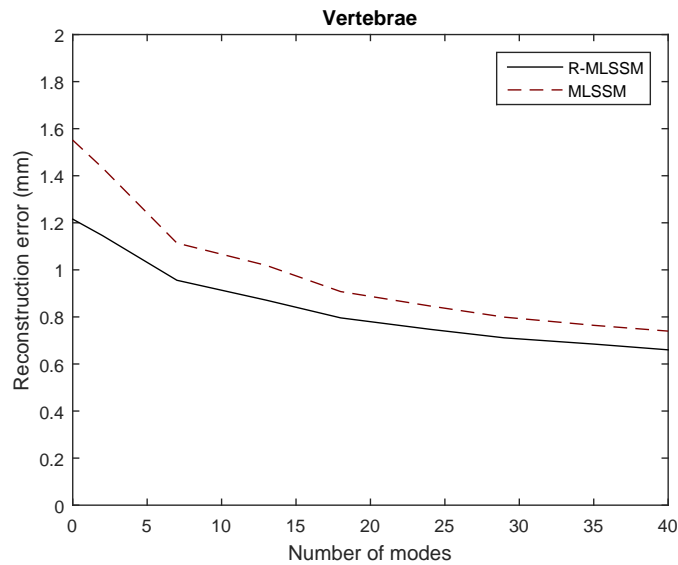
Figure 6.2: Reconstruction error curve of the MLSSM and R-MLSSM. The models were constructed with 100 patients from the IVD database, trying to maintain the distribution across the different positions and degenerations as uniform as possible. The error was computed in a leave-one-out fashion over the whole database of 256 patients.

manual segmentations superimposed to their reconstructions of a T2, T7, T11 and L5 vertebra from four random patients. This figure illustrates the apparent good reconstruction of the model regardless the spinal position.

In addition, the first mode of variation of the two hierarchical levels of the vertebral model are presented in Fig. 6.4 and Fig. 6.5. The former presents the variation of the first mode in the first hierarchical level. This level encodes the variation of the spinal positions and successfully shows that the vertebral shape deforms from a top thoracic-like shape to a low-lumbar-like one. The latter image presents the variation in shape of the first mode variation in the second hierarchical level (inter-subject variability). In this second scenario, the mean shape of different spinal positions were used to visualise the effect of the deformations in different type of vertebrae.

6.4.6 Uncorrelation of the modes of variation

The R-MLSSM definition includes as constraint that the model parameters from different levels must be uncorrelated between each other. This property was checked
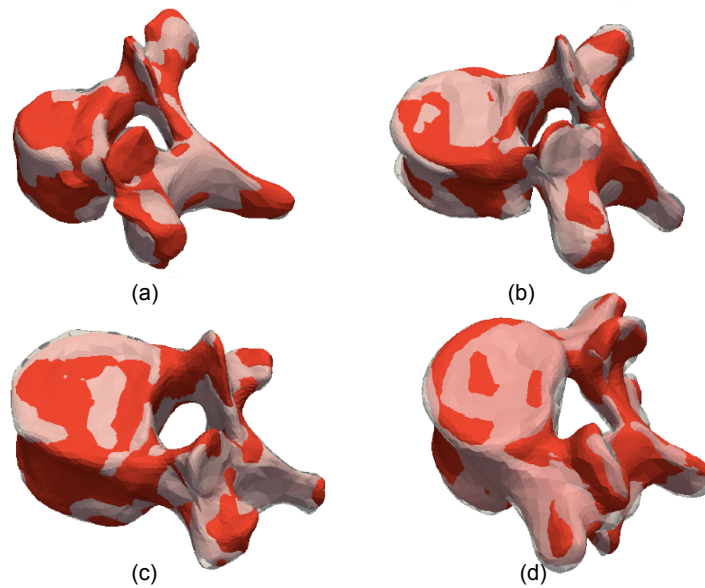
Figure 6.3: Superimposition of reconstructed vertebral shapes (white meshes) in different spinal positions and the original vertebrae (red meshes), from randomly chosen subjects. Images (a) to (d) show the spinal positions T2, T7, T11 and L5, respectively.
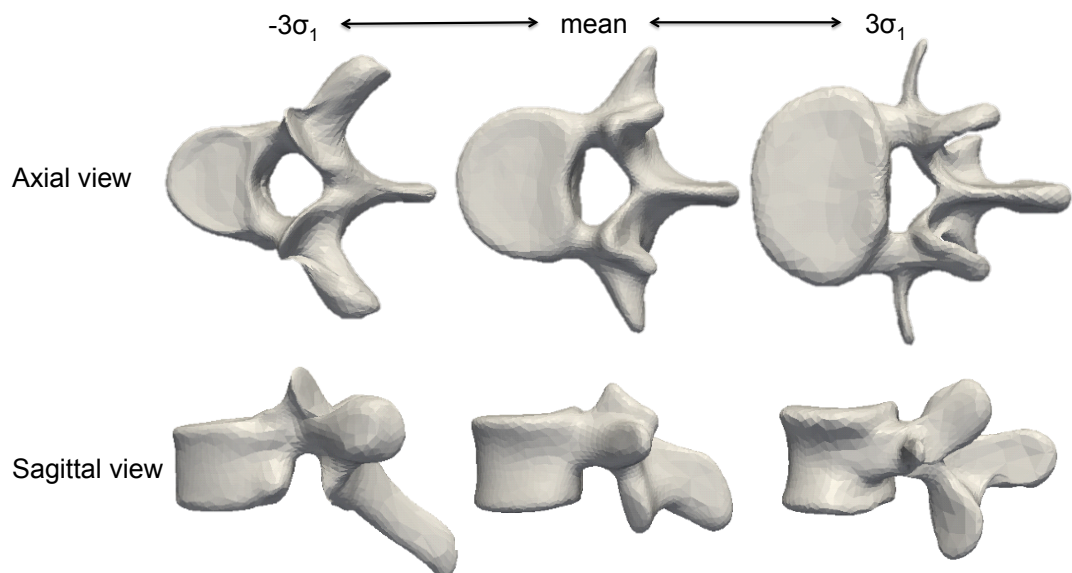
Figure 6.4: First mode of variation of the first hierarchical level of the vertebral model. Two different views are presented to properly show that the variation in shape corresponds to the variation across the spine.
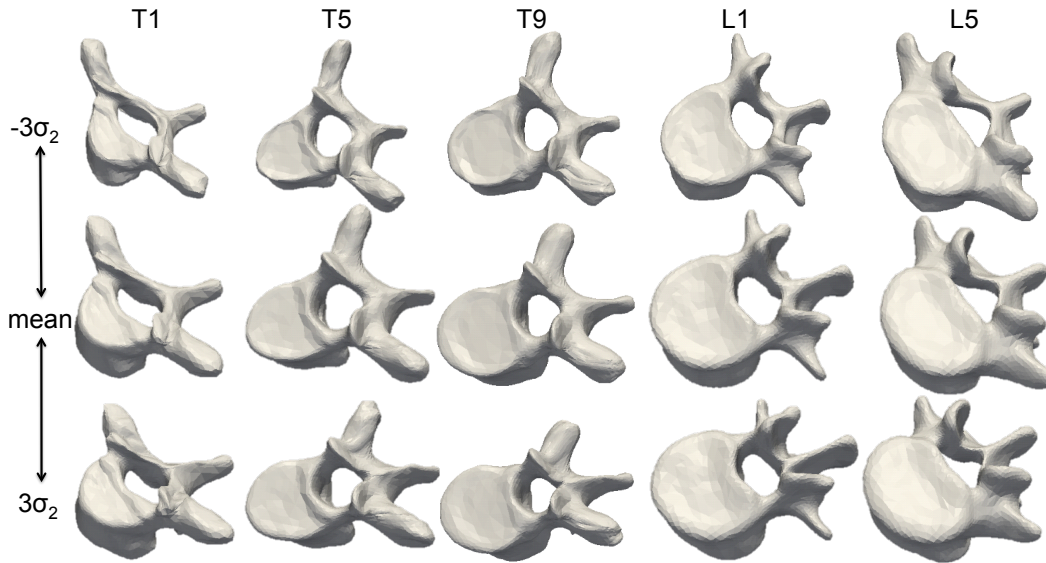
Figure 6.5: First mode of variation of the second hierarchical level of the vertebral model. This figure presents the variation in shape across subject population at different spinal positions.

numerically by estimating the covariances

$$\langle b^{(a)} \otimes b^{(c)} \rangle \simeq \sum_k (b_k^{(a)^{\mathrm{T}}} b_k^{(c)})$$

$$\forall a, c \in 1 \cdots L \qquad \text{with} \qquad a \neq c.$$

(6.22)

where k represents each case in the dataset. The maximum value was 1.24×10^{-5}, which is sufficiently small to be considered as numerical noise.

6.5 Discussion

From the experimental results, it was observed that the advantage of the R-MLSSM is twofold: First, its reconstruction and classification abilities are always equal or superior to that of having individual SSMs for each factor value. Second, it is capable of modelling the information of groups of data $\mathcal{C}_{F_a}$, for which the number of cases K_{F_a} is small or even zero. The latter leads to a much higher reconstruction power as shown with the IVDs (Fig. 6.4.2), and allows the classification into level values that are not present in the training database, as shown with the *Non-complete R-MLSSM* in

Tables 6.5 and 6.6. This classification is not possible with individual SSMs per degree of degeneration and position, since they cannot be generated for level values where no training case exists.

Another advantage of the proposed formulation is the possibility of rebalancing the model when the real proportions of the cases in the population are known, and are different to those in the training database. In this work, two datasets of the spine covering different regions are used. The number of vertebrae in each spinal position is different in each dataset and therefore, the R-MLSSM requires being rebalanced to represent the real population.

6.5.1 Reconstruction

Section 6.2.4 presented two different scenarios for reconstruction: the first one when the model parameters until level $L - 1$ are known and the second when they are unknown. The former is implicitly assumed in the construction of the R-MLSSM yielding the most reliable reconstructions. However, this information is usually unknown and it is commonly expected to be computed during the process. Nevertheless, the results show that the reconstruction with unknown (*R-MLSSM*) factor values provides results as accurate as those with known ones (*R-MLSSM with known factor values*).

6.5.2 Classification

The classification technique introduced in Section 6.2.5 was developed to exploit the advantages of the R-MLSSM. For instance, it allows a prior probability that corresponds to the α factors introduced in Section 6.2.1 for the rebalanced formulation. It employs a covariance matrix with the whole training database, in order to produce more reliable results than the standard SSM when the number of training samples is rather small. It allows the computation of the classification when the number of training samples for a specific combination of factors is zero, which is not possible with the standard SSM.

6.5.3   Limitations

The Gaussian assumption of the SSM is also valid for each hierarchical level of the R-MLSSM. Another limitation is originated in the construction of the R-MLSSM, which is performed by extracting the information given by pathologies, positions, etc. Thus, the final hierarchical level contains solely the information of the inter-subject variability from the entire database. This implies that this inter-subject variation must be shared across the whole database. For instance, an extreme case would be the creation of a vertebral R-MLSSM with a first hierarchical level separating vertebral bodies (VB) and vertebral processes. The resultant model would combine the processes and VB deformations, allowing the VB to deform in the same manner as processes and vice versa.

6.6   Conclusions

Herein it has been introduced a new Multi linear SSM, which in contrast with the state-of-the-art models, holds all the properties that are expected, such as working on databases with missing and unevenly distributed data or producing optimal selection of a subset of modes of variation. The proposed model enables more accurate reconstructions than the standard SSM and it allows the classification of new objects according to the factors at each level, even when the training set contains very few or no samples with such combination of factors. It has been also shown that this model takes into account the case where the training database does not contain a faithful representation of the distribution of the factor values in the population. Although the model has only been tested for the case of shape models, it could be used for intensity appearance. This appearance model could be combined with the shape one to provide more accuracy in the classification of objects. For instance, the classification of the IVD degeneration lacks of accuracy, because the shape is not as good discriminant of the IVD degeneration as the intensity is. However, these experiments were not performed in this thesis and they have been left for future work. The reason is that the method for IVD classification introduced in Chapter 5 provides results as accurate as the values

given by the experts and therefore, they are still used for the final purpose.

Chapter 7

Combining all source of information: fusing multimodal 3D spine-related models into a personalised Volumetric model

In this dissertation, it has hitherto been described methods to perform different tasks for the creation of patient-specific models for simulations. This chapter provides the necessary tools for combining the segmented structures and creates the personalised volumetric model. From Chapter 3 and Chapter 4, it was acquired the segmentation of IVDs and vertebrae from MR and CT images, respectively. Therefore, this chapter begins with the introduction of a method that aligns the IVDs and vertebrae surface meshes into a single complete anatomical model. This method employs an adaptation of the segmentation framework explained in Chapter 4 in order to avoid overlaps between vertebrae. Finally, a mesh morphing algorithm, based on B-splines, is employed to map a template volumetric mesh to the patient-specific surface mesh. This morphing reduces possible misalignments and guarantees the convexity of the model elements. This morphing method was **not** developed by the author of this thesis. Instead, an already existing method was employed for this step. This method is, nevertheless, commented in the methodology for completeness.

This chapter follows the publication [241].

7.1   Motivation

The construction of patient-specific biomechanical models for simulation is an important task for the uprising computational medicine. These models may be employed in many applications, such as the study of diseases or conditions [2, 3], estimating outcomes of treatments [4–6] or predicting the conditions for bone fractures, or other disorders [8, 9].

This chapter focuses on the creation of patient-specific volumetric meshes (VM), adapted to the anatomy of the patient using one or several medical images. In order to facilitate the estimation of material properties, the intensities from the medical images are stored in each cell as well as the degree of degeneration or fracture.

This process can be decomposed into two steps: Alignment of the anatomical structures into a single anatomical surface model and the generation of the volumetric mesh. In the literature, the alignment process is not commonly required, since all the structures are usually extracted from the same image.

The alignment or matching of an anatomical structure into a medical image is a common problem in image-guided intervention. Although, these anatomical structures usually belong to the same patient as the image, they may have been extracted from a different image modality and/or different time point. Thus, this process is usually solved with an image to image registration [242, 243]. The drawback of this procedure when applied to articulated structures, such as the spine, is that acquiring images from different modalities or different time points implies that the patient changed his or her pose. Therefore, a rigid registration cannot be used (Fig. 7.1). In addition, a non-rigid registration approach is not desirable either, because this procedure may change the shape of the vertebrae. Nonetheless, there exist registration procedures that allows to define objects as rigid to overcome this limitation [244, 245], however, these type of approaches are usually more computationally expensive, because they need all the image information, or they require segmentations in both MR and CT, or they produce

gaps and overlaps that result in unrealistic configurations. Moreover, these registration methods either do not completely restrict the deformations to be rigid or they could allow the overlap or collapse of two vertebrae. Thus, in this thesis it was developed a mesh to image registration technique for the alignment step. The method is based on a strategy similar to the segmentation framework from Chapter 4. However, it restrains the shape to rigid motions instead of to the B-splines space.
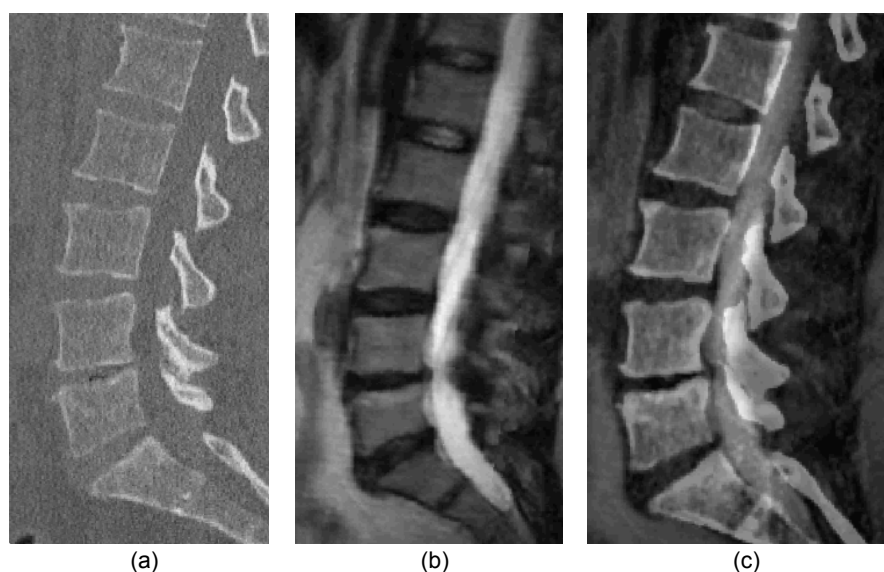
Figure 7.1: Example of CT-MR registration. Original CT image (a), original MR image (b), Aligned CT image and superimposed to the MR image (c). The latter shows that different vertebra should be aligned independently and thus a rigid registration is not accurate enough.

There exist different types of volumetric mesh generation methods:

- **Method A:** The volumetric mesh is generated directly from the patient-specific surface mesh. The simplest example is the generation of a tetrahedral mesh filling the interior of a triangular mesh [246].

- **Method B:** A template volumetric mesh is deformed using the intensity of a medical image [6, 247]. This strategy combines in a single process the segmentation and the generation of the volumetric mesh. It is, however, difficult to apply when more than one image is required.

- **Method C:** The segmentation of the structure of interest is directly used by con-

sidering the voxels as cells of a volumetric mesh [101, 102]. This approach allows fast simulations to be performed, but models are not precise since the size of the cells is not flexible, producing not satisfactory boundaries that lead to inaccurate finite element analysis [248].

- **Method D:** A template volumetric mesh is morphed to adapt to the patient-specific surface mesh [103, 104].

In this study, a mesh morphing technique was also introduced (**Method D**) to deform a template volumetric mesh to the previously built patient-specific surface mesh. This technique propagates the geometrical and topological characteristics of the template volumetric mesh to the patient-specific anatomical surface mesh. Vertices and cells of the generated patient-specific volumetric mesh have one-to-one anatomical correspondences with the template. This facilitates the propagation of the material properties and boundary conditions from the template.

7.2 Automatic creation of patient specific volumetric meshes

7.2.1 Vertebrae alignment on MR data

The proposed matching technique requires an initial alignment of the vertebrae and IVDs. This process starts by defining the upper and lower centre of each vertebra endplate and computing the vertebral body (VB) centres (c_1). Subsequently, the unit vector pointing from the bottom to the top endplate is computed ($\hat{u}_1$). The same process is repeated using consecutive pairs of IVDs, with each IVD centre corresponding to a vertebral endplate. Thus, the corresponding vertebral centre (c_2) is computed as well as the unit vector pointing from the bottom to the top IVD ($\hat{u}_2$). Then, the rigid transformation is given by the translation from c_1 to c_2 and by the rotation matrix R_o is attained with the Rodrigues rotation formula [186]:

$$R_o = \mathbb{I} + B + \frac{B^2}{1 + \hat{u}_1 \cdot \hat{u}_2} \quad \text{with} \quad B = \hat{u}_1 \hat{u}_2^T - \hat{u}_2 \hat{u}_1^T \qquad (7.1)$$

where $\mathbb{I}$ is the identity matrix.

After being initalised, vertebrae are rigidly displaced towards the vertebral boundaries in the MR image (Fig. 7.3) with a similar procedure to that introduced in Chapter 4. However, in this new scenario, no statistical shape model (SSM) or B-Spline constrained are employed, since only rigid transformations at each vertebra are allowed.

For the sake of clarity, the group of energies, instances and indexes employed in this chapter and related to those in Chapter 4 are explained below:

v: Index running across all the vertebrae composing the region of the spine being used.

p: Index running across all the points of one particular vertebra.

$\boldsymbol{S}_v^{\mathrm{B}}$: Instance of a vertebral shape that is restricted to a rigid transformation from the initial one. Each point of this shape is represented by $\boldsymbol{s}_{v,p}^{\mathrm{B}}$. Observe that in Chapter 4, this parameterisation was performed using B-splines. Thus, its representation in this chapter is different and given by:

$$\boldsymbol{s}_{v,p}^{\mathrm{B}} = \boldsymbol{R}_v \boldsymbol{s}_{v,p}^{o} + \boldsymbol{c}_v \qquad (7.2)$$

with $\boldsymbol{R}_v$ being a rotation matrix, $\boldsymbol{s}_{v,p}^{0}$ the points in the initial shape $\boldsymbol{S}_v^{0}$ of vertebra v and $\boldsymbol{c}_v$ a translation vector.

$\boldsymbol{S}_v^{\mathrm{I}}$: Free instance that is obtained by displacing each individual landmark using the energy $E^{\mathrm{I}}(\boldsymbol{S}^{\mathrm{I}}, I)$.

I: The image intensity, in this chapter the MR image.

$E^{\mathrm{SIM}}(\boldsymbol{S}^{\mathrm{B}})$: Energy involving the SIM model, the definition is given in (4.16).

$E^{\mathrm{I\text{-}B}}(\boldsymbol{S}^{\mathrm{B}}, \boldsymbol{S}^{\mathrm{I}})$: Energy that relates shapes $\boldsymbol{S}_v^{\mathrm{B}}$ and $\boldsymbol{S}_v^{\mathrm{I}}$ for all v. This energy is defined in Section 4.5.3 as:

$$E^{\mathrm{I\text{-}B}}(\boldsymbol{S}^{\mathrm{B}}, \boldsymbol{S}^{\mathrm{I}}) = \frac{1}{2} \sum_v \|\boldsymbol{S}_v^{\mathrm{B}} - \boldsymbol{S}_v^{\mathrm{I}}\|_F^2 \qquad (7.3)$$

$E^{\mathrm{I}}(\boldsymbol{S}^{\mathrm{I}}, I)$: This energy is computed as the weighted summation of a group of features. In the alignment process, there exist two new set of features, one for the region

surrounding the vertebra foramen and another for the vertebral body (VB). The processes were not used in this setting, because they are not well visualised in the MR image and therefore did not provide useful information.

The features used in the foramen were:

1. **Directional derivative along the normal direction pointing inwards.** This feature searches for changes from low to high intensity values in the image.

2. **Negative Intensity.** This feature searches for the maximum value in the profile of intensities extracted along the normal direction of the mesh at each vertex.

For the VB:

1. **Directional derivative along the normal direction pointing outwards**. This feature searches for changes from high to low intensity values in the image.

2. **Intensity.** This feature searches for the minimum intensity in the profile.

3. **Distance to the initial point at each iteration.** This feature serves as a spring energy, which penalises large movements.

As in Chapter 4, the energy problem is based on minimising a linear combination of the individual energies given by:

$$\boldsymbol{S}^{\mathrm{B}} = \operatorname*{argmin}_{\boldsymbol{S}^{\mathrm{B}}} \min_{\boldsymbol{S}^{\mathrm{I}}} E(\boldsymbol{S}^{\mathrm{B}}, \boldsymbol{S}^{\mathrm{I}}, \boldsymbol{I}) \quad \text{where} \tag{7.4}$$

$$E(\boldsymbol{S}^{\mathrm{B}}, \boldsymbol{I}, \boldsymbol{S}^{\mathrm{I}}) = w^{\mathrm{I}} E^{\mathrm{I}}(\boldsymbol{S}^{\mathrm{I}}, I) + w^{\mathrm{B\text{-}I}} E^{\mathrm{B\text{-}I}}(\boldsymbol{S}^{\mathrm{B}}, \boldsymbol{S}^{\mathrm{I}}) \tag{7.5}$$

$$+ w^{\mathrm{SIM}} E^{\mathrm{SIM}}(\boldsymbol{S}^{\mathrm{B}})$$

In order to solve this energy, the same alternating optimisation process introduced in Section 4.5.6 may be employed. However, since the SSM is not used, the process can be reduced to only two steps:

Optimisation for the shape $\boldsymbol{S}^{\mathrm{I}}$. First $\boldsymbol{S}^{\mathrm{I}}$ is achieved through the optimisation of $E^{\mathrm{I}}(\boldsymbol{S}^{\mathrm{I}}, I) + E^{\mathrm{B\text{-}I}}(\boldsymbol{S}^{\mathrm{B}}, \boldsymbol{S}^{\mathrm{I}})$. This optimisation is performed at each landmark independently, following the typical strategy used in ASM.

Gradient descent step for the shape S^B. This shape involves two terms of the energy:

$$w^{\text{I-B}} E^{\text{I-B}}(\boldsymbol{S}^{\text{B}}, \boldsymbol{S}^{\text{I}}) + w^{\text{SIM}} E^{\text{SIM}}(\boldsymbol{S}^{\text{B}}) \tag{7.6}$$

$\boldsymbol{S}^{\text{B}}$ is parameterised by a set of angles $\boldsymbol{\psi}_v$ and translation vectors $\boldsymbol{c}_v$, defining the rotation and translation of the shape with respect to its previous step. As usual, the gradient descent requires the computation of the partial derivate of the energies with respect to all the variables to be optimised ($\boldsymbol{\psi}_v$ and $\boldsymbol{c}_v$), which are:

$$\frac{\partial E^{\text{I-B}}}{\partial \psi_{v,k}} = \sum_p \left(\boldsymbol{R}_v \boldsymbol{s}_{v,p}^o + \boldsymbol{c}_v - \boldsymbol{s}_{v,p}^B \right)^{\text{T}} \frac{\partial \boldsymbol{R}_v}{\partial \psi_{v,k}} \boldsymbol{s}_{v,p}^o$$

$$\frac{\partial E^{\text{I-B}}}{\partial \boldsymbol{c}_v} = \sum_p \left(\boldsymbol{R}_v \boldsymbol{s}_{v,p}^o + \boldsymbol{c}_v - \boldsymbol{s}_{v,p}^B \right)^{\text{T}}$$

$$\frac{\partial E^{\text{SIM}}}{\partial \psi_{v,k}} = \frac{\partial \boldsymbol{s}_{v,p}^{\text{B}}}{\partial \psi_{v,k}} \frac{\partial E^{\text{SIM}}}{\partial \boldsymbol{s}_{v,p}^{\text{B}}} = \boldsymbol{s}_{v,p}^{\text{o,T}} \frac{\partial \boldsymbol{R}_v}{\partial \psi_{v,k}} \frac{\partial E^{\text{SIM}}}{\partial \boldsymbol{s}_{v,p}^{\text{B}}}$$

$$\frac{\partial E^{\text{SIM}}}{\partial \boldsymbol{c}_v} = \frac{\partial \boldsymbol{s}_{v,p}^{\text{B}}}{\partial \boldsymbol{c}_v} \frac{\partial E^{\text{SIM}}}{\partial \boldsymbol{s}_{v,p}^{\text{B}}} = \frac{\partial E^{\text{SIM}}}{\partial \boldsymbol{s}_{v,p}^{\text{B}}} \tag{7.7}$$

with $\psi_{v,k}$ being each of the components $\psi_{v,x}, \psi_{v,y}, \psi_{v,z}$ of the angle $\boldsymbol{\psi_v}$ and $\partial E^{\text{SIM}}/\partial \boldsymbol{s}_{v,p}^{\text{B}}$ being describe in (4.25).

7.2.2 Morphing of the template volumetric mesh into the patient-specific surface mesh

Two steps are used in the morphing. Firstly, an iterative closest point (ICP) [249] method is used to perform an affine registration. Secondly, a mesh-to-mesh non-rigid registration based on B-splines is employed to adapt a template volumetric mesh to the patient-specific surface mesh. In registration, cubic B-splines are commonly used to parameterise with continuous and smooth transformations, with the additional benefit of a reduced number of degrees of freedom [250]. This transformation is controlled by a regular grid of points.

The proposed framework includes an internal energy that aims at preserving the size and proportions of the volumetric mesh. This energy is based on elastic properties
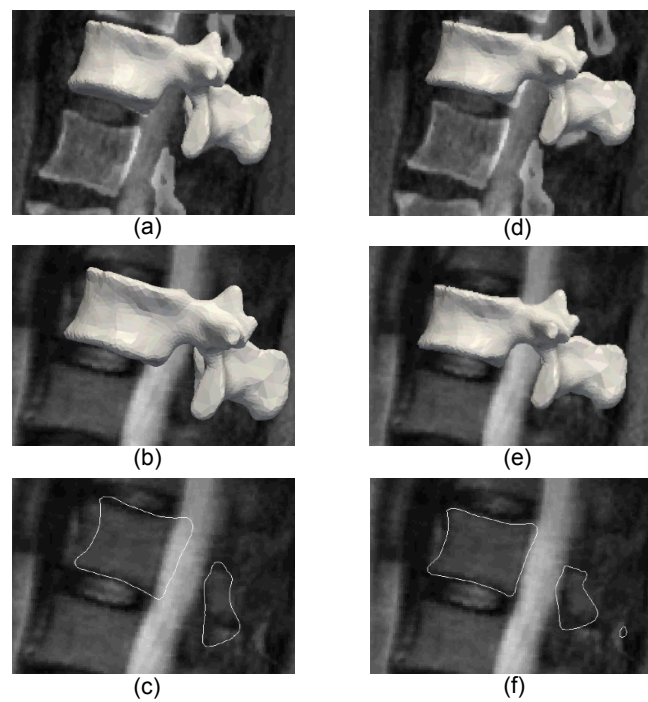
Figure 7.2: An example of the initial alignment of the L1 vertebra using only IVD information ((a) - (c)) and of the full alignment with the addition of the MR information ((d) - (f)). Observe that using only the centre of the IVD produces already similar results to those achieved through the rigid registration CT-MR. Top images show the aligned vertebra superimposed to the transformed CT image and MR image, middle images show the aligned vertebra and MR image, and the bottom images show the contour of the aligned vertebra in one MR slice.

relative to the volumetric cell edge lengths and solid angles, assuming a continuous material with homogeneous Young's modulus.

The similarity metric contains two symmetric energies, which are computed as the weighted squared summation of the point to surface distance from the target mesh to the moving one and vice versa. The weights were defined as 1 minus the squared dot product of the normals. The goal of having two symmetric energies is to avoid the registration process to fail in narrow structures, such as the transverse processes. The point to surface distance is computed with respect to specific regions. Therefore, a vertex belonging to the surface mesh of an L1 vertebra can be only attracted by the surface of the volumetric mesh belonging to the L1 vertebra.

The employed optimisation technique was steepest gradient descent, because of the simplicity of its implementation.

7.2.3 Mapping image intensities from the MR and CT to the patient-specific volumetric mesh

The segmentation of the IVDs and vertebra defines the region of interest in the MR and CT images. Since the material properties are correlated to the image intensity, it was also created a method to map these intensities into the volumetric mesh. In order to cope with the difference in size between the cells in the volumetric mesh and the image voxels, a weighted average of the voxels that completely or partially intersect with the volumetric mesh was used. The weight factors were proportional to the intersection volume.

7.3 Data

The dataset contains lumbar CT and MR images from 13 males and 17 females with a mean age of 40 (age interval: 27-62 years) as well as the surfaces meshes from the segmentation of the vertebrae and IVDs. All the images were collected at the National Center for Spinal Disorders (NCSD) located in Budapest, Hungary. Patients were selected for participating in the European MySpine project [34].

7.3.1   Magnetic resonance image of Lumbar Spine

T2-weighted MR coronal and sagittal acquisitions from an open 0.4T MR machine (Hitachi, Twinsburg, OH). The in-plane resolution was $0.7 \times 0.7 mm^2$ with a spacing between slices of $4.0mm$. These two type of images were fused, using the method from Chapter 3, to achieve an isotropic size of $0.7mm$ at each direction.

7.3.2   Computed Tomography of Lumbar Spine

Direct CT scans from patients suffering from low back pain using a bone window. The Axial in-plane resolution is $0.608 \times 0.608 \ mm^2$ with a spacing between slices of 0.625 mm.

7.3.3   Surface and volumetric meshes

The surface meshes were obtained using the methods from Chapter 3 and Chapter 4.

The template volumetric mesh comprises the annulus fibrosus, nucleus pulposus, vertebrae and string representations of the major muscles and ligaments connected to the lumbar spine. The latter did not have any correspondence in the surface meshes.

7.4   Results

7.4.1   Implementation details

- The weights of the vertebral body features were: $1.0mm/in$ for the directional derivative, $1.0in^{-1}$ for the intensity and $0.5mm^{-1}$ for the distance feature.

- The weights of the vertebral foramen features were: $1.0mm/in$ for the directional derivative, $0.5in^{-1}$ for the intensity.

- The morphing employs 4 scales, with number of grid control points from $8 \times 4 \times 4$ to $64 \times 32 \times 32$ doubling at each scale.

- The criteria to stop the alignment was that 100% of the landmarks do not move more than 0.2 times the size of a voxel in the direction of the normal at the specific

landmark. This criteria resulted in 3 to 5 iterations. In addition, the maximum number of iterations were set to 20.

- The size of the profiles was set individually for each landmark p of the mesh. In the first iteration, it was set to 20 voxels in the direction pointing outwards and $\min(20, a)$ voxels pointing inwards. The value a is half of the number of voxels from p to the intersection of the mesh and a line following the normal direction of the mesh at p. In the last iteration, they were set to 4 voxels inwards and 4 outwards.

- The number of resolutions was kept to one, since the initialisation already locates the IVDs in a good location.

where the unit in represents the unit of the image intensity.

7.4.2 Visual results

The results were visually evaluated by an expert, who first assessed the vertebral surface alignment and subsequently the volumetric mesh. The alignment was found accurate (Fig. 7.3) as well as the models in all cases (Fig.7.4). The alignment was considered accurate when the contours of the aligned vertebrae in MR could have been delineated by an expert. However, in few patients was found that the vertebral body height in MR and CT did not coincide. Therefore, if the vertebral contours slightly overlapped the IVD region because of this reason, the alignment was still considered accurate. For the volumetric meshes this effect is partially compensated by the mesh morphing algorithm.

7.4.3 Quantitative evaluation

An expert manually delineated the contour of the lumbar spine in the mid-sagittal and mid-coronal slices of 15 randomly selected patients (Fig. 7.5). This contouring was repeated twice, obtaining contours A and B, to compute the intra-observer variability. Table 7.1 presents the mean and 95 percentile of the point to surface distance from the contours A and B to the surface meshes after the alignment and to the surface of the
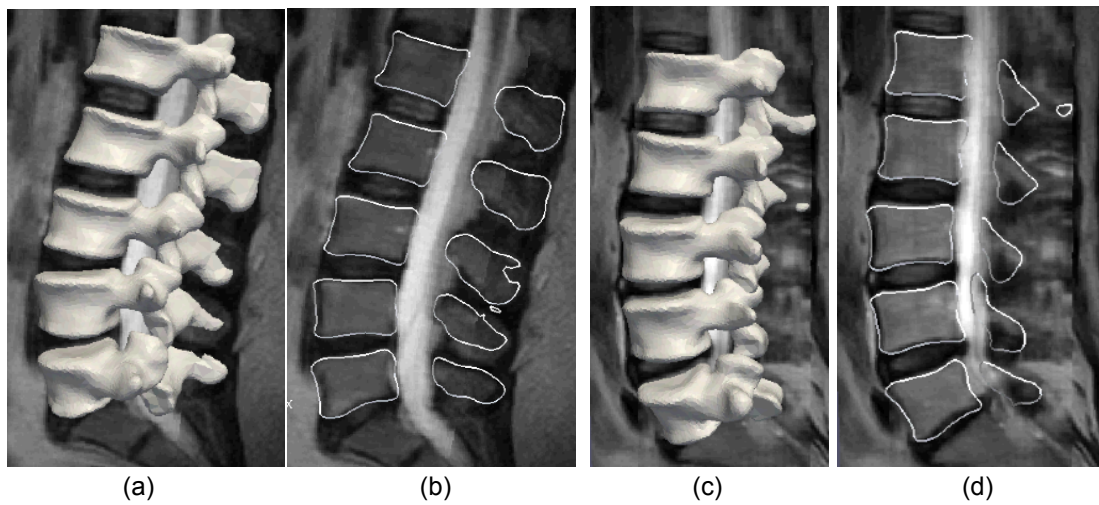
Figure 7.3: An example of the vertebral alignment of two patients. Sub-figures (a) and (c) show the whole vertebrae whereas (b) and (d) only the section belonging to the MR slice.
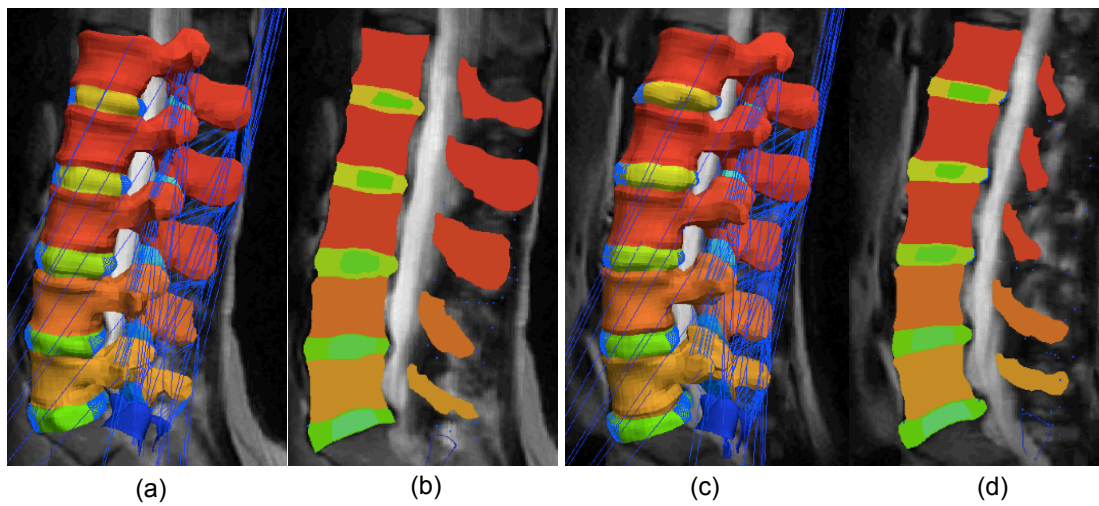
Figure 7.4: An example of two patient-specific volumetric meshes. Sub-figures (a) and (c) show the whole vertebrae whereas (b) and (d) only the section belonging to the MR slice.

volumetric mesh. This table also presents the intra-observer variability computed as the distance from contours A to contours B.
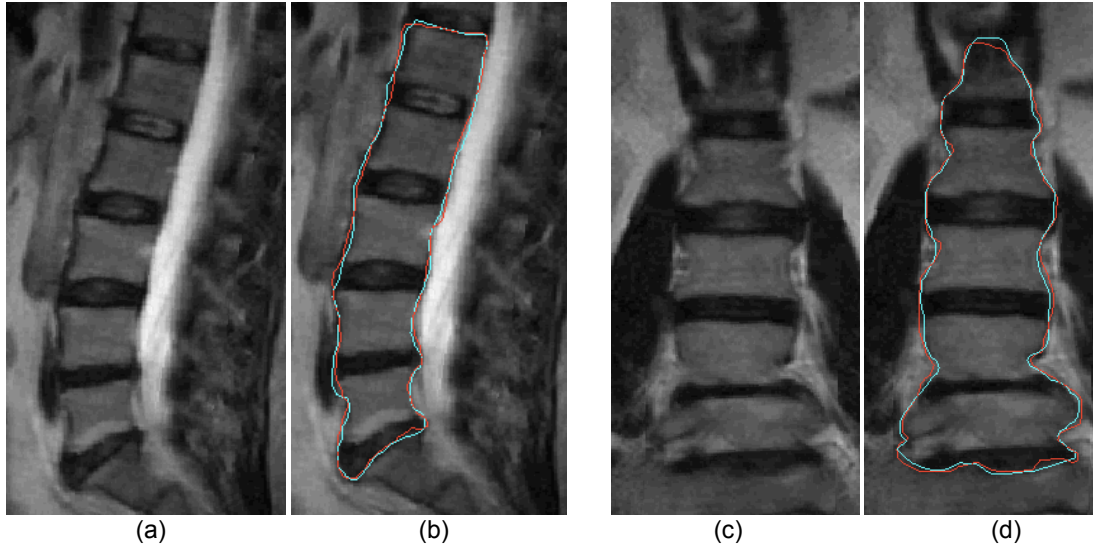
Figure 7.5: Example of the two contours delineated in the Sagittal and coronal MR images. Observe that the boundaries are not clear, producing error higher than a voxel size.

Table 7.1: Mean, 95 percentile (95-p) and maximum value of the point to surface distance (PSD) from contour A and B to the lumbar spine surface meshes (SM) and volumetric meshes, and from contours A to B.

Measures	contour A		contour B		Contour A
	to SM	to VM	to SM	to VM	to B
mean PSD	1.11	1.01	1.15	1.09	0.81
95-p PSD	1.69	1.84	1.73	1.57	1.21
Maximum PSD	2.9	2.8	2.8	2.7	2.1

7.4.4 Computational time

The experiment were run using a PC with Intel(R) Xeon CPU E5620 at 2.40 Ghz with 8 GB of RAM and running a 64-bit Windows 7 operating system. All the code was written in C++ using the libraries from the Insight Toolkit (ITK) and Visualisation toolkit (VTK) [157, 251] for basic manipulation of mesh and images. The alignment requires 1 minute for each vertebrae whereas the morphing takes 1 hours and 50 minutes for each patient (four scales) as average.

7.5   Discussion

The proposed method begins with an initial alignment of the vertebral surface meshes using the centre of the IVDs in MR. Subsequently, their position is adjusted by matching the vertebral mesh borders to those in the MR image. Finally, a morphing technique is used to create the volumetric mesh by adapting a template to the IVD and vertebral meshes after the alignment.

The current methodology w The process was evaluated using the point to surface distance from manual contours to the aligned meshes (and the surface of the volumetric mesh). The mean distance to the ground truth was 1.11mm (1.15mm), a value between 1 and 2 voxel size (0.7mm), and slightly larger than the intra-observer variability (0.81mm). These results support the relatively good accuracy of the method. However, the errors are not negligible, due to thick and blurry vertebral borders observed in MRI, which also affects the manual delineations.

Although, it was not proposed a method to compute boundary conditions, material properties and other important parameters for biomechanical models, the proposed method facilitates the propagation of most of these parameters to the patient-specific model. In addition, the process allows the extraction of the intensity values from the image, which is an important step towards the material property calculation.

7.6   Conclusions

A pipeline for the creation of patient-specific volumetric meshes for biomechanical simulations has been proposed and tested in images and segmentations of vertebrae and intervertebral discs of the lumbar spine. The process exploits the fact that the spine is an articulated object. It begins with a rigid alignment of the individual vertebrae in between the corresponding IVD pairs. Subsequently, vertebrae are aligned individually using the MR intensities. This second step exploits the high intensity of the spinal cord and the location of the IVDs to adjust the vertebrae properly.

The second part is the morphing of a template volumetric mesh to the spine segmentation using a mesh morphing process. This process was not developed during the

thesis and it was only employed to finalise the construction of the volumetric mesh.

This two-step method has the advantage of allowing the morphing to correct small vertebra-IVD misalignment prompt to occur given the thick and blurry borders of the vertebra in the MR images.

Chapter 8

Conclusions and Outlook

8.1 Overview

This thesis posed the challenge of developing a framework to automatically construct patient-specific anatomical and labelled models. As a proof of concept, spine models were constructed from CT and MR images, resulting in the following contributions:

- A new statistical model that encodes the information of the separation between objects, named Statistical Interspace model (SIM), similarly as SSM encodes the inner variation of an object (Chapter 4).

- A new technique that extends PCA to multi linearity, named rebalanced Multi-level component analysis (R-MLCA), that allows the creation of SSMs with multiple factors, such as the grade of fracture of a vertebra (Chapter 6).

- A method to train intensity features for the matching algorithm of point-based segmentation frameworks (Chapter 3).

- The development of a segmentation framework, which minimises a set of energies given the SIM, a group of SSMs and the intensity energy (Chapter 4) to attain anatomically correct and accurate segmentations.

- A fusion algorithm for merging images of the same modality and patient to increase the resolution while providing more realistic voxel intensities for the computation of the material properties (Chapter 3).

145

- A novel method to perform mesh to image rigid registrations in order to align articulated structures, such as vertebrae and IVDs, extracted from different images (Chapter 7). In order to avoid overlaps, the method includes the SIM model.

8.2 Conclusions

Personalised medicine is the future of health care. In spine, the diagnosis almost always has got some patient-specific details and the treatment should be individualised in most of the cases. In more complicated cases the importance of the surgical planning has been already emphasised by other authors [252] and in the future patient specific rapid prototyped implant manufacturing can be the dominant surgical approach for instrumented spinal surgeries. Different - preliminary - computer simulation methods are already available for the surgical planning and some of these tools are connected with the intraoperative surgical navigation systems [253]. The platform for the patient-specific simulation of different treatment of the whole lumbar spine has been already developed too [34]. In these decision-supporting, surgical-planning and/or outcome predictive computational systems, the proper, 3D segmentation of the spinal elements, and their to build the patient spine model are the key starting points for the workflow.

In this thesis statistical models were employed, and new ones were developed, to construct anatomically correct spine models for biomechanical simulations. This work can be structured into three parts, addressing each of the three objectives presented in Chapter 1.

In addition, the models originated from the proposed pipeline were used in a real clinical setting (Appendix A). The results showed that the current pipeline provides patient-specific models that are suitable for simulations.

8.2.1 Development of a Segmentation Framework that extracts anatomically correct object shapes with SSMs

In this thesis, two different segmentation frameworks has been proposed, each of them solving different issues that the state-of-the-art methods using SSMs have. Among

them, the segmentation framework proposed in Chapter 4, using Statistical interspace model (SIM), provides the greatest improvement in terms of accuracy and in reducing the need for a large database for creating SSMs. The latter improvement is the consequence of two different factors: First, it is no longer necessary to have a model of the whole spine, but rather one for each individual vertebra, and second, since the SSMs are used as an energy in a framework where B-splines controls the possible shape deformations, the segmentation has a greater degree of freedom allowing more precision with fewer training samples. However, the clear benefit of using this novel framework is that, to the best knowledge of the author of this dissertation, it is the only framework that has successfully prevented overlaps, excessive separation between objects and unrealistic rotations. All these issues may not significantly influence the accuracy of the segmentation using standard measurements, but prevent the models to be employed for simulations.

This new framework appears to have two main limitations: The employed energy to warp the mesh within the intensity image may not be considered as completely optimal. However, since the group of energies are integrated modularly in the framework, any of them could be replaced by another energy of the same type. A further limitation is that to optimise the set of energies to obtain the segmentation, there exists no closed form solution, as with the standard SSM. Thus, the optimisation procedure may not attain the global minimum and also has slower convergence.

8.2.2 Development of a classification method that can be integrated in the segmentation framework

Patient-specific volumetric meshes for biomechanical simulations require the computation of material properties. For this process, the identification of the stage of a disease, or disorder affecting these material properties is of utmost importance. In addition, this labelling of anatomical structures may improve the segmentation results if it is smartly combined within a unique framework. During the development of this thesis, a classification framework that labelled IVDs according to their degree of degeneration was created, which attains results of similar accuracy to that of an expert in the field.

However, as stated in Chapter 5, this framework was specific to IVDs and it could not be embedded in a unique framework with the segmentation. Thus, in Chapter 6, a new technique was proposed, named rebalanced multilevel component analysis (R-MLCA), that allows the creation of models with respect to multiple factors, such as a stage of a disease or the grade of a bone fracture.

The clear limitation of this technique is that it does not provide a set of modes that only modify one factor. For instance, assume that a database of lumbar spine CT includes patients with different stages of scoliosis and vertebrae with different grades of fracture. A model created with R-MLCA will have a level, with a set of modes controlling all the possible stages of scoliosis, and second one controlling all possible stages of scoliosis and grade of fractures at the same time, instead of having a level that solely influences the grade of fracture. In the literature, different frameworks that do not have this issue have been proposed [168, 231, 232], but, on the other hand, they have other drawbacks as mentioned in Chapter 6.

8.2.3 Development of an alignment method to merge articulated anatomical structures from different images

Chapter 7 includes the procedure to align articulated structures from different images. Since vertebrae are rigid objects, whose shape should not change with the patient's posture, each vertebra was rigidly aligned between their correspondent IVDs. The proposed approach employs the SIM model to avoid inter-vertebral overlaps, excessive separation and other issues that are common in the alignment of articulated objects. This method was specifically design for our purpose and it is preferable with respect to the state-of-the-art methods, which employ image-to-image registration with a rigid penalisation. The reason is that the latter is either more computationally expensive, they require segmentations in both images, or do not completely restrict the deformations to be rigid, since otherwise, they could allow the overlap or collapse of two vertebrae, which is not desirable either.

8.3   Future lines of research

The possible addition to this thesis are fourfold.

8.3.1   Automation of the initialisation

In this thesis, the initialisation of the vertebrae or IVD has been performed by manually selecting the centre of the IVDs either in CT or MR, allowing the user to select the number of vertebrae and IVDs. However, the automation of this step could facilitate the creation of models when the number of vertebrae and IVDs is known and a large number of models must be created. Examples of methods to perform such tasks are: [27, 28, 161, 162].

8.3.2   Rebalanced multi-linear statistical appearance model (R-MLSAM)

The R-MLCA proposed in Chapter 6 could be used to create appearance models, by employing the same approach presented in [33] with PCA. This model may allow the possibility of classifying the IVDs according to their degree of degeneration but experiments would be required to demonstrate it is feasibility.

8.3.3   Statistical interspace model with generation ability

The SIM, introduced in Chapter 4, contains the covariance matrix and the mean values of the relative position vectors between pairs of points on both sides of the space that is being modelled. A future line of research is to study the possibility of creating a model with a similar procedure to that of the SSM. This model will combine the information of multiple points and will require the use of a dimensionality reduction technique to acquire its possible modes of variation. The resultant model will encode the relative information between different pairs of points as the SSM does. This extra information may improve the relative position of whole objects, which is not precise with a point-wise model.

8.3.4 Substituting CT images for VFA or DXA

The main issue of using CT images is the radiation that patients are exposed to. Thus, the use of 2D modalities, such as X-rays, VFAs or DXAs to create 3D objects with the use of SSMs [47, 48, 59, 61, 73, 119, 123, 254] is a cutting-edge technique that could be integrated into the proposed model construction framework. The goal would be to reformulate the segmentation framework proposed in Chapter 4 to have a reconstruction method that employs the SIM. This model would control the relative position between vertebrae avoiding overlaps, which are an issue in the state-of-the-art methods, such as [47].

8.3.5 Detection of the facet joint osteoarthritis

The SIM encodes the information of the possible shapes of the space between objects. This ability has been exploited to eliminate overlaps between processes, particularly, in the facet joints where the separation is usually smaller than the voxel size. An important disease that have been reported to be related to IVD degeneration is facet joint osteoarthritis [207]. This disease is visualised in CT as a narrower intervertebral process and/or an increase of bone formation around the joint and/or black artefacts. These characteristics should not influence greatly the performance of the propose method, neither in the segmentation nor in the alignment. But more importantly, the SIM could be used to classify patients according to this disease. The SIM models the interprocess space using the relative position vectors, which act as local descriptors of the interspace between objects. Therefore, these vectors could be used as features for a standard classifier, such as neural network, logistic regression, adaboost or any other presented in chapter 5, to perform the classification of patients according to the severity of this disease.

Chapter 9

Appendices

Appendix A - Clinical use of the Biomecanical models

Part of the research presented on this thesis was developed in the context of the MySpine project [34], whose consortium was composed of seven european institutions. Among these institutions, one of them designed the template biomechanical model, and another created a set of equations to compute the material properties using the image intensities and the anatomical object labels provided in the proposed framework. The created models, with materials properties, were used to perform biomechanical simulations that were employed to estimate the best possible treatment for patients suffering from low back pain. The near 200 patient-specific biomechanical models showed that the current pipeline provides models that are suitable for simulations.

In addition, a user-friendly graphical interface (GUI), Fig. 9.1, was also implemented within the GIMIAS platform [255]. This GUI was used to allow partners from other institutions to create the models and visualise them. It was divided into five components or modules to allow the user to perform only one part:

- **XNAT window:** Access to an internet database to extract the CT and MR images. The XNAT platform and this particular component of the GUI was not developed by the author of this dissertation.

- **MR Discs:** Segmentation of the IVDs, it is requires for the user to click the centre of the IVDs that are going to be processed.

- **CT Discs:** Segmentation of the vertebrae, it is required for the user to click the centre of the IVDs right below of the vertebrae that are going to be processed.

- **VertAlignmentMR:** Alignment of the vertebra in the MR image, no input from the user is needed.

- **CreateFEM:** Creation of the Biomechanical model. This particular component of the GUI was not developed by the author of this dissertation.

In addition, joining the different modules into a single GUI was not carried out by the author of this dissertation.

Appendix B - Extension of the Interpolation technique to more than 2 views

In this appendix, the initial bi-linear interpolation process presented by Li *et al.* [151] is extended to the case of having more than 2 views. Although, their method includes a second step based on wavelets, that step does not have any restriction on the number of volumes to be fused. Observe that the different views of MR images are commonly perpendicular. Therefore, it is reasonable to expect this property, as assumed in [151]. However, for the sake of completeness, the equations in the case of a non-perpendicular case are also presented in the last part of this appendix.

Perpendicular problem

This setting is similar to that in Fig. 3.5 with the addition of a third volume in the axial view. Thus, the result is an image volume with cuboids inside that does not have their intensity defined. The facing problem is to find the value of each point p within these cuboids. As shown by Li *et al.* [151] for the 2D case, the first step is to find the closest voxels with intensities surrounding each of the voxels p (Fig. 9.2 - a). Then, two triangular pyramids are constructed joining three different points of the set $v_1, \cdots, v_6$ and p. Observe that there exists 4 possible combinations of opposed pair of triangular pyramids, as it was proposed in [151], the pair of triangular pyramids for

which the summation of all the sides is minimum is selected. To simplify the notation, let us define an index k identifying each of the pyramids ($k = 1, 2$) and an index i running along the three vertices of each pyramids different to p, so that the vertices $v_1, \cdots, v_6$ become $v_{i,k}$ with $i = 1, 2, 3$.

For each of the pyramids k, it is required to compute the value of its height h_k and the pixel intensity at point q_k. These q_k points are the projection of p to the plane given by vertices $v_{i,k}$ $\forall i$.

$$I(\boldsymbol{q}_k) = \sum_{i \in M} \alpha_i I(\boldsymbol{v}_{i,k}) \qquad \text{with} \qquad \alpha_{i,k} = \frac{\sum_{j \in M - \{i\}} d_{j,k}}{\sum_{j \in M} d_{j,k}} \tag{9.1}$$

where $I(\boldsymbol{q}_k)$ represents the intensity of the point $\boldsymbol{q}_k$, M is the set with numbers 1,2 and 3 and $d_{i,k}$ are the distance from $\boldsymbol{v}_{i,k}$ to $\boldsymbol{q}_k$ $\forall i, k$ as shown in Fig. 9.2.

Having computed h_k and $I(\boldsymbol{q}_k)$, the interpolation of point p is performed with the standard linear interpolation.

$$I(\boldsymbol{p}) = \frac{h_2}{h_1 + h_2} I(\boldsymbol{q}_1) + \frac{h_1}{h_1 + h_2} I(\boldsymbol{q}_2) \tag{9.2}$$

Thus, the objectives are to find the values of $d_{i,k}$, and the values of h_k using the distances from each $\boldsymbol{v}_{i,k}$ to $\boldsymbol{p}$, named $x_{i,k}$.

First, the values h_k may be obtained using the formula to compute the volume of a triangular pyramid.

$$V_k = \frac{1}{3} A_k h_k \implies h_k = \frac{3V_k}{A_k} \tag{9.3}$$

where A_k is the area of the triangle base.

Since the angles between the different $x_{i,k}$ are rectangles, the volume of the pyramid can also be computed as:

$$V_k = \frac{1}{3} \left(\frac{1}{2} x_{2,k} x_{3,k} \right) x_{1,k} = \frac{\prod_{i=1}^{3} x_{i,k}}{6} \tag{9.4}$$

In addition, the $b_{i,k}$ are obtained using the Pythagoras theorem and A_k using the

Heron's formula:

$$A_k = \sqrt{t_k(t_k - b_{1,k})(t_k - b_{2,k})(t_k - b_{3,k})} \quad \text{with} \quad t_k = \frac{1}{2}\sum_{i=1}^{3} b_{i,k}$$

$$b_{1,k} = \sqrt{x_{1,k}^2 + x_{3,k}^2} \qquad b_{2,k} = \sqrt{x_{1,k}^2 + x_{2,k}^2} \qquad b_{3,k} = \sqrt{x_{2,k}^2 + x_{3,k}^2} \tag{9.5}$$

leading to the solution of h_k:

$$h_k = \frac{\sum_{i=1}^{3} x_{i,k}}{2\sqrt{t_k(t_k - b_{1,k})(t_k - b_{2,k})(t - b_{3,k})}} \tag{9.6}$$

Having acquired h_k, the $d_{i,k}$ are computed using Pythagoras theorem $d_{i,k} = \sqrt{x_{i,k}^2 - h_k^2}$.

Non perpendicular problem

In the case that images are not perpendicular to each other, the same method as introduced in the previous section may be used. The only difference is the computation of h_k, which may be performed by using the following equation:

$$\sum_{i=1}^{3} \frac{b_{i,k}}{2}\sqrt{s_{i,k}^2 - h_k^2} = A_k \tag{9.7}$$

where $s_{i,k}$ are the slant heights (Fig. 9.3) and A_k is computed using (9.5) with $b_{i,k}$ being described using the law of cosines as follows:

$$b_{1,k} = \sqrt{x_{1,k}^2 + x_{3,k}^2 - 2x_{1,k}x_{3,k}\cos\alpha_{1,k}}$$

$$b_{2,k} = \sqrt{x_{1,k}^2 + x_{2,k}^2 - 2x_{1,k}x_{2,k}\cos\alpha_{2,k}}$$

$$b_{3,k} = \sqrt{x_{2,k}^2 + x_{3,k}^2 - 2x_{2,k}x_{3,k}\cos\alpha_{3,k}} \tag{9.8}$$

$$s_{i,k} = 2\frac{\sqrt{t_{i,k}(t_{i,k} - x_{i,k})(t_{i,k} - x_{j,k})(t_{i,k} - b_{i,k})}}{b_{i,k}}$$

$$\text{with} \quad t_{i,k} = \frac{x_{i,k} + x_{j,k} + b_{i,k}}{2} \quad \text{and} \quad j = mod(i - 1, 3)$$

The value of h_k may be obtained with an optimisation technique or by the resolution of the polynomial that the expansion of this equation leads to.
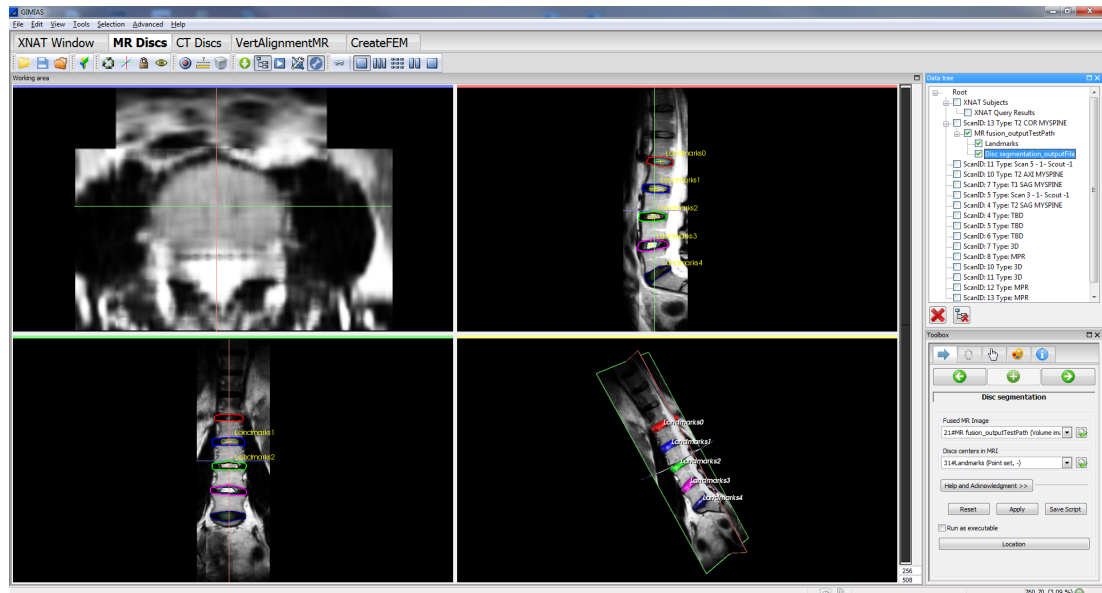
(a)

(b)

Figure 9.1: Graphical User Interface (GUI). It is composed of five parts: XNAT, segmentation of IVDs, segmentation of vertebrae, Alignment of vertebrae in MR and model creation. Each of them was separated in case the user only desires one of the steps.
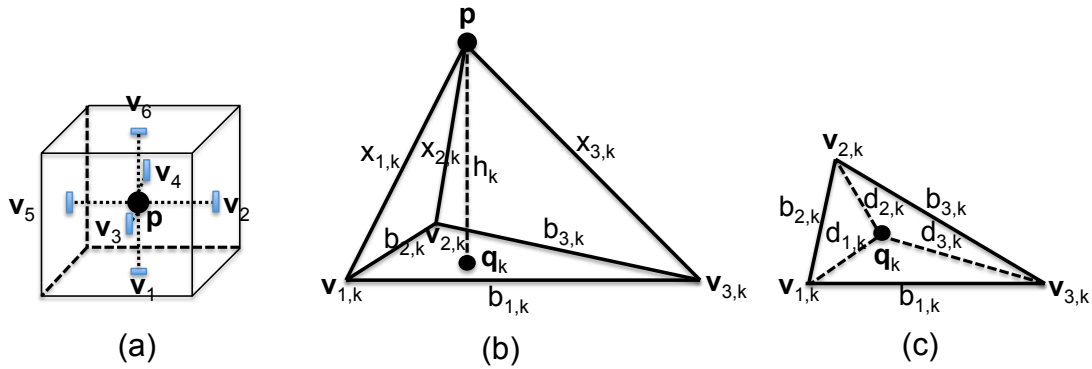
Figure 9.2: Description of the problem. Fig. (a) illustrates a point p that needs to be interpolated using the six values v_i from the six image slices that surrounds it. Joining three v_i and p creates the pyramid (b), whose base was named A_k and it is represented in (c).
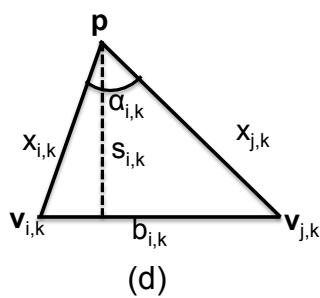
Figure 9.3: Triangular side of figure 9.2 - b, with the slant height ($s_{i,k}$). The value i is each of the three sides and the value $j = mod(i - 1, 3)$.

Bibliography

[1] Kunkler K., "The role of medical simulation: an overview," *The International Journal of Medical Robotics and Computer Assisted Surgery*, vol. 2, no. 3, pp. 203–210, 2006.

[2] Huynh A., Aubin C., Mathieu P., and Labelle H., "Simulation of progressive spinal deformities in duchenne muscular dystrophy using a biomechanical model integrating muscles and vertebral growth modulation," *Clinical Biomechanics*, vol. 22, no. 4, pp. 392–399, 2007.

[3] Imai K., Ohnishi I., Yamamoto S., and Nakamura K., "In vivo assessment of lumbar vertebral strength in elderly women using computed tomography-based nonlinear finite element model," *Spine*, vol. 33, no. 1, pp. 27–32, 2008.

[4] Denozière G. and Ku David N., "Biomechanical comparison between fusion of two vertebrae and implantation of an artificial intervertebral disc," *Journal of biomechanics*, vol. 39, no. 4, pp. 766–775, 2006.

[5] Anekstein Y., Brosh T., and Mirovsky Y., "Intermediate screws in short segment pedicular fixation for thoracic and lumbar fractures: a biomechanical study," *Journal of spinal disorders & techniques*, vol. 20, no. 1, pp. 72–77, 2007.

[6] Haouchine N., Dequidt J., Peterlik I., Kerrien E., Berger M.-O., and Cotin S., "Image-guided simulation of heterogeneous tissue deformation for augmented reality during hepatic surgery," in *Mixed and Augmented Reality (ISMAR), 2013 IEEE International Symposium on*. IEEE, 2013, pp. 199–208.

[7] Liu A., Tendick F., Cleary K., and Kaufmann C., "A survey of surgical simulation: applications, technology, and education," *Presence: Teleoperators and Virtual Environments*, vol. 12, no. 6, pp. 599–614, 2003.

[8] Perry A., Mahar A., Massie J., Arrieta N., Garfin S., and Kim C., "Biomechanical evaluation of kyphoplasty with calcium sulfate cement in a cadaveric osteoporotic vertebral compression fracture model," *The Spine Journal*, vol. 5, no. 5, pp. 489–493, 2005.

[9] Majumder S., Roychowdhury A., and Pal S., "Simulation of hip fracture in sideways fall using a 3d finite element model of pelvis–femur–soft tissue complex with simplified representation of whole body," *Medical engineering & physics*, vol. 29, no. 10, pp. 1167–1178, 2007.

[10] Bro-Nielsen M., "Finite element modeling in surgery simulation," *Proceedings of the IEEE*, vol. 86, no. 3, pp. 490–503, 1998.

[11] Oshima M., Torii R., Kobayashi T., Taniguchi N., and Takagi K., "Finite element simulation of blood flow in the cerebral artery," *Computer methods in applied mechanics and engineering*, vol. 191, no. 6, pp. 661–671, 2001.

[12] Jing W., Brooke S., Sean A S., Sven S., Gonzalo R F. o., Thomas JR H., and Charles A T., "A one-dimensional finite element method for simulation-based medical planning for cardiovascular disease," *Computer Methods in Biomechanics & Biomedical Engineering*, vol. 5, no. 3, pp. 195–206, 2002.

[13] Li H. and Wang Z., "Intervertebral disc biomechanical analysis using the finite element modeling based on medical images," *Comput Med Imag Grap*, vol. 30, no. 6-7, pp. 363 – 370, 2006, Medical Imaging and Telemedicine.

[14] Grau V., Mewes A., Alcaniz M., Kikinis R., and Warfield Simon K., "Improved watershed transform for medical image segmentation using prior information," *IEEE T Med Imaging*, vol. 23, no. 4, pp. 447–458, 2004.

[15] Pan Z. and Lu J., "A bayes-based region-growing algorithm for medical image segmentation," *Computing in science & Engineering*, vol. 9, no. 4, pp. 32–38, 2007.

[16] Ayed I., Punithakumar K., Garvin G., Romano W., and Li S., "Graph cuts with invariant object-interaction priors: application to intervertebral disc segmentation," in *Lect Notes Comput Sc (IPMI)*, Berlin, Heidelberg, 2011, pp. 221–232, Springer-Verlag.

[17] Chen X., Udupa Jayaram K., Bagci U., Zhuge Y., and Yao J., "Medical image segmentation by combining graph cuts and oriented active appearance models," *Image Processing, IEEE Transactions on*, vol. 21, no. 4, pp. 2035–2046, 2012.

[18] Aslan M. S., Shalaby A., Abdelmunim H., and Farag A., "Probabilistic shape-based segmentation method using level sets," *Institution of Engineering and Technology*, pp. 1–13, 2013.

[19] Jurcak V., Fripp J., Engstrom C., Walker D., Salvado O., Ourselin S., and S. C., "Atlas based automated segmentation of the quadratus lumborum muscle using non-rigid registration on magnetic resonance images of the thoracolumbar region," in *I S Biomed Imaging (ISBI)*, may 2008, pp. 113–116.

[20] Tsai A., Jr. Y. A., Wells W., Tempany C., Tucker D., Fan A., Grimson W., and Willske A., "A shape-based approach to the segmentation of medical imagery using level sets," *IEEE T Med Imaging*, vol. 22, no. 2, pp. 137–154, 2003.

[21] Michopoulou S., Costaridou L., Panagiotopoulos E. Speller R., Panayiotakis G., and Todd-Pokropek A., "Atlas-based segmentation of degenerated lumbar intervertebral discs from MR images of the spine," *Eng Med Biol Soc Ann*, vol. 56, no. 9, pp. 2225–2231, sept. 2009.

[22] Roberts M., Cootes T., Pacheco E., Oh T., and Adams J., "Segmentation of lumbar vertebrae using part-based graphs and active appearance models," in *Lect Notes Comput Sc (MICCAI)*, pp. 1017–1024. Springer, 2009.

[23] Castro-Mateos I., Humbert L., Whitmarsh T., Lazary A., del R. B. L., and Frangi A. F., "3D reconstruction of intervertebral discs from T1-weighted magnetic resonance images.," in *I S Biomed Imaging (ISBI)*. 2012, pp. 1695–1698, IEEE.

[24] Gregory J., Testi D., Stewart A., Undrill P., Reid D., and Aspden R., "A method for assessment of the shape of the proximal femur and its relationship to osteoporotic hip fracture," *Osteoporosis International*, vol. 15, no. 1, pp. 5–11, 2004.

[25] Lund M., de B. M., Tanko L., and Nielsen M., "Shape regression for vertebra fracture quantification," in *Medical Imaging*. International Society for Optics and Photonics, 2005, pp. 723–731.

[26] Roberts M. G., Cootes T. F., and Adams J. E., "Robust active appearance models with iteratively rescaled kernels.," in *British Machine Vision Conference– BMVC*, 2007, pp. 1–10.

[27] Schmidt S., Bergtholdt M., Dries S., and Schnorr C., "Spine detection and labeling using a parts-based graphical model," in *Lect Notes Comput Sc (IPMI)*, 2007, pp. 122–133.

[28] Corso J. J., Alomari Raja' S., and Chaudhary V., "Lumbar disc localization and labeling with a probabilistic model on both pixel and object features," in *Lect Notes Comput Sc (MICCAI)*, Berlin, Heidelberg, 2008, pp. 202–210, Springer-Verlag.

[29] Fritscher K., Grunerbl A., Hanni M., Suhm N., Hengg C., and Schubert R., "Trabecular bone analysis in CT and X-ray images of the proximal femur for the assessment of local bone quality," *IEEE T Med Imaging*, vol. 28, no. 10, pp. 1560–1575, 2009.

[30] Chen Y.-W., Luo J., Tateyama T., Han X.-H., Furukawa A., Kanasaki S., and Jiang H., "Statistical shape model of the liver and effective mode selection for classification of liver cirrhosis," in *Information Science and Service Science*

and Data Mining (ISSDM), 2012 6th International Conference on New Trends in. IEEE, 2012, pp. 449–452.

[31] Castro-Mateos I., Pozo Jose M., Lazary A., and Frangi A., "Intervertebral disc classification by its degree of degeneration from t2-weighted magnetic resonance images," *Accepted for publication in the European Spine Journal*, 2016.

[32] Cootes T., Taylor C., and Graham J., "Active shape models- their training and applications," *Comput Vis Image Und*, vol. 61, no. 1, pp. 38–59, 1995.

[33] Cootes T. F., Edwards G. J., and Taylor C. J., "Active appearance models," *IEEE T Pattern Anal*, vol. 23, no. 6, pp. 681–685, 2001.

[34] MySpine ., "MySpine patient-specific spinal treatment simulation," http://www.myspineproject.eu, 2010, Accessed: 2014-05-14.

[35] Koschan A., Kang S., Paik J., Abidi B., and Abidi M., "Color active shape models for tracking non-rigid objects," *Pattern Recognition Letters*, vol. 24, no. 11, pp. 1751–1765, 2003.

[36] Sukno F., Ordás S., Butakoff C., Cruz S., and Frangi A., "Active shape models with invariant optimal features: Application to facial analysis," *IEEE T Pattern Anal*, vol. 29, no. 7, pp. 1105–1117, 2007.

[37] Ahmad T., Taylor C. J., Lanitis A., and Cootes T. F., "Tracking and recognising hand gestures, using statistical shape models," *Image and Vision Computing*, vol. 15, no. 5, pp. 345–352, 1997.

[38] Luettin J., Thacker N. A., and Beet S. W., "Active shape models for visual speech feature extraction," *NATO ASI SERIES F COMPUTER AND SYSTEMS SCIENCES*, vol. 150, pp. 383–390, 1996.

[39] Heimann T. and Meinzer H. P., "Statistical shape models for 3D medical image segmentation: A review," *Med Image Anal*, vol. 13, no. 4, pp. 543–563, 2009.

[40] Castro-Mateos I., Pozo Jose M., Cootes Timothy F., Wilkinson J M., Eastell R., and Frangi Alejandro F., "Statistical shape and appearance models in osteoporosis," *Current osteoporosis reports*, vol. 12, no. 2, pp. 163–173, 2014.

[41] Roberts M. G., Cootes T. F., and Adams J. E., "Linking sequences of active appearance sub-models via constraints: An application in automated vertebral morphometry.," in *British Machine Vision Conference–BMVC*, 2003, pp. 1–10.

[42] Zamora G., Sari-Sarraf H., and Long L. R., "Hierarchical segmentation of vertebrae from X-ray images," in *Medical Imaging 2003*. International Society for Optics and Photonics, 2003, pp. 631–642.

[43] Iglesias J. and de B. M., "Semiautomatic segmentation of vertebrae in lateral X-rays using a conditional shape model," *Academic radiology*, vol. 14, no. 10, pp. 1156–1165, 2007.

[44] Lindner C., Thiagarajah S., Wilkinson J., Wallis G., and Cootes T., "Accurate fully automatic femur segmentation in pelvic radiographs using regression voting," in *Lect Notes Comput Sc (MICCAI)*, pp. 353–360. Springer, 2012.

[45] Howe B., Gururajan A., Sari-Sarraf H., and Long L., "Hierarchical segmentation of cervical and lumbar vertebrae using a customized generalized hough transform and extensions to active appearance models," in *Image Analysis and Interpretation, 2004. 6th IEEE Southwest Symposium on*. IEEE, 2004, pp. 182–186.

[46] Seim H., Kainmueller D., Heller M., Lamecker H., Zachow S., and Hege H., "Automatic segmentation of the pelvic bones from CT data based on a statistical shape model.," in *Spring Eurograph (VCBM)*, 2008, pp. 93–100.

[47] Whitmarsh T., Humbert L., De Craene M., Del Rio Barquero L. M., and Frangi A. F., "Reconstructing the 3D shape and bone mineral density distribution of the proximal femur from dual-energy X-ray absorptiometry," *IEEE T Med Imaging*, vol. 30, no. 12, pp. 2101–2114, 2011.

[48] Sadowsky O., Ramamurthi K., Ellingsen L. M., Chintalapani G., Prince J., and Taylor R. H., "Atlas-assisted tomography: registration of a deformable atlas to compensate for limited-angle cone-beam trajectory," in *Biomedical Imaging: Nano to Macro, 2006. 3rd IEEE International Symposium on*. IEEE, 2006, pp. 1244–1247.

[49] Ahmad O., Ramamurthi K., Wilson K. E., Engelke K., Prince R., and Taylor R., "Volumetric DXA (VXA): a new method to extract 3D information from multiple in vivo DXA images," *Journal of Bone and Mineral Research*, vol. 25, no. 12, pp. 2744–2751, 2010.

[50] Aslan M., Ali A., Chen D., Arnold B., Farag A., and Xiang P., "3D vertebrae segmentation using graph cuts with shape prior constraints," in *IEEE Image Proc*. IEEE, 2010, pp. 2193–2196.

[51] Cremers D., Osher Stanley J., and Soatto S., "Kernel density estimation and intrinsic alignment for shape priors in level set segmentation," *International Journal of Computer Vision*, vol. 69, no. 3, pp. 335–351, 2006.

[52] Li W., Kornak J., Harris T., Lu Y., Cheng X., and Lang T., "Hip fracture risk estimation based on principal component analysis of QCT atlas: a preliminary study," in *SPIE Medical Imaging*. International Society for Optics and Photonics, 2009, p. 72621M.

[53] Rueckert D., Frangi A. F., and Schnabel J., "Automatic construction of 3D statistical deformation models of the brain using nonrigid registration," *IEEE T Med Imaging*, vol. 22, no. 8, pp. 1014–1025, 2003.

[54] Staib L. H. and Duncan J. S., "Model-based deformable surface finding for medical images," *IEEE T Med Imaging*, vol. 15, no. 5, pp. 720–731, 1996.

[55] Tateyama T., Foruzan H., and Chen Y.-W., "2d-pca based statistical shape model from few medical samples," in *Intelligent Information Hiding and Multimedia Signal Processing, 2009. IIH-MSP'09. Fifth International Conference on*. IEEE, 2009, pp. 1266–1269.

[56] McIntosh C. and Hamarneh G., "Medial-based deformable models in nonconvex shape-spaces for medical image segmentation," *Medical Imaging, IEEE Transactions on*, vol. 31, no. 1, pp. 33–50, 2012.

[57] Castro-Mateos I., Pozo J.-M., Lazary A., and Frangi A. F., "2D segmentation of intervertebral discs and its degree of degeneration from T2-weighted magnetic resonance images," in *SPIE Medical Imaging*. International Society for Optics and Photonics, 2014, pp. 903517–903517.

[58] Zhou M., Liang L., Sun J., and Wang Y., "AAM based face tracking with temporal matching and face segmentation," in *Computer Vision and Pattern Recognition (CVPR), 2010 IEEE Conference on*. IEEE, 2010, pp. 701–708.

[59] Tang T. S. and Ellis R. E., "2D/3D deformable registration using a hybrid atlas," in *Lect Notes Comput Sc (MICCAI)*, pp. 223–230. Springer, 2005.

[60] Aviv H. and Leo J., "Registration of a CT-like atlas to fluoroscopic X-ray images using intensity correspondences," *International Journal of Computer Assisted Radiology and Surgery*, vol. 3, no. 6, pp. 493–504, 2008.

[61] Ahmad O. M., Ramamurthi K., Wilson K., Engelke K., Bouxsein M., and Taylor R., "3D structural measurements of the proximal femur from 2D DXA images using a statistical atlas," in *SPIE Medical Imaging*. International Society for Optics and Photonics, 2009, vol. 7260, pp. 5–13.

[62] Gower J., "Generalized procrustes analysis," *Psychometrika*, vol. 40, no. 1, pp. 33–51, 1975.

[63] Smyth P. P., Taylor C. J., and Adams J. E., "Automatic measurement of vertebral shape using active shape models," *Image and Vision Computing*, vol. 15, no. 8, pp. 575–581, 1997.

[64] Pilgram R., Walch C., Blauth M., Jaschke W., Schubert R., and Kuhn V., "Knowledge-based femur detection in conventional radiographs of the pelvis," *Computers in Biology and Medicine*, vol. 38, no. 5, pp. 535–544, 2008.

[65] Guglielmi G., Palmieri F., Placentino M., D'Errico F., and Stoppino L., "Assessment of osteoporotic vertebral fractures using specialized workflow software for 6-point morphometry," *European Journal of Radiology*, vol. 70, no. 1, pp. 142–148, 2009.

[66] Aouache M., Hussain A., Samad S., Hamzaini A., and Ariffin A., "Osteoporosis presence verification using mace filter based statistical models of appearance with application to cervical X-ray images," in *4th Kuala Lumpur International Conference on Biomedical Engineering 2008*. Springer, 2008, pp. 607–610.

[67] Whitmarsh T., Humbert L., Del Río Barquero L. M., Gregorio S., and A. F F., "3D reconstruction of the lumbar vertebrae from anteroposterior and lateral dual-energy X-ray absorptiometry," *Med Image Anal*, pp. 475–487, 2013.

[68] Bryan R., Nair P., and Taylor M., "Use of a statistical model of the whole femur in a large scale, multi-model study of femoral neck fracture risk," *Journal of Biomechanics*, vol. 42, no. 13, pp. 2171–2176, 2009.

[69] Castro-Mateos I., Pozo Jose M., Eltes Peter E., Del Rio L., Lazary A., and Frangi Alejandro F., "3D segmentation of annulus fibrosus and nucleus pulposus from T2-weighted magnetic resonance images," *Physics in medicine and biology*, vol. 59, no. 24, pp. 7847–7864, 2014.

[70] Paragios N., "A level set approach for shape-driven segmentation and tracking of the left ventricle," *IEEE T Med Imaging*, vol. 22, no. 6, pp. 773–776, 2003.

[71] Fritscher K D., Grunerbl A., and Schubert R., "3D image segmentation using combined shape-intensity prior models," *International Journal of Computer Assisted Radiology and Surgery*, vol. 1, no. 6, pp. 341–350, 2007.

[72] Schuler B., Fritscher K., Kuhn V., Eckstein F., and Schubert R., "Using a statistical appearance model to predict the fracture load of the proximal femur," in *SPIE Medical Imaging*. International Society for Optics and Photonics, 2009, pp. 72610W–10.

[73] Lamecker H., Wenckebach T. H., and Hege H.-C., "Atlas-based 3D-shape reconstruction from X-ray images," in *Pattern Recognition, 2006. ICPR 2006. 18th International Conference on*. IEEE, 2006, vol. 1, pp. 371–374.

[74] Davies Rhodri H., Twining Carole J., Cootes Timothy F., and Taylor Chris J., "Building 3-d statistical shape models by direct optimization," *Medical Imaging, IEEE Transactions on*, vol. 29, no. 4, pp. 961–981, 2010.

[75] Kotcheff A. and Taylor Ch. J., "Automatic construction of eigenshape models by direct optimization," *Med Image Anal*, vol. 4, no. 2, pp. 303 –314, December 1998.

[76] Zhang S., Zhan Y., Dewan M., Huang J., Metaxas Dimitris N., and Zhou Xiang S., "Towards robust and effective shape modeling: Sparse shape composition," *Med Image Anal*, vol. 16, no. 1, pp. 265–277, 2012.

[77] Cootes T. F. and Taylor C. J., "A mixture model for representing shape variation," *Image and Vision Computing*, vol. 17, no. 8, pp. 567–573, 1999.

[78] Larsen R. and Baggesen Hilger K., "Statistical shape analysis using non-Euclidean metrics," *Med Image Anal*, vol. 7, no. 4, pp. 417–423, 2003.

[79] Nielsen A. A., "Kernel maximum autocorrelation factor and minimum noise fraction transformations," *IEEE T Image Process*, vol. 20, no. 3, pp. 612–624, 2011.

[80] Kurazume R., Nakamura K., Okada T., Sato Y., Sugano N., Koyama T., Iwashita Y., and Hasegawa T., "3D reconstruction of a femoral shape using a parametric model and two 2D fluoroscopic images," *Comput Vis Image Und*, vol. 113, no. 2, pp. 202–211, 2009.

[81] Schumann S., Tannast M., Nolte L.-P., and Zheng G., "Validation of statistical shape model based reconstruction of the proximal femur, a morphology study," *Medical Engineering & Physics*, vol. 32, no. 6, pp. 638–644, 2010.

[82] De Bruijne M. and Pettersen P., "Supervised shape analysis for risk assessment in osteoporosis," in *I S Biomed Imaging (ISBI)*. IEEE, 2008, pp. 1581–1584.

[83] Schuler B., Fritscher K., Kuhn V., Eckstein F., Link T., and Schubert R., "Assessment of the individual fracture risk of the proximal femur by using statistical appearance models," *Medical physics*, vol. 37, pp. 2560–2571, 2010.

[84] Goodyear S., Barr R., McCloskey E., Alesci S., Aspden R., Reid D., and Gregory J., "Can we improve the prediction of hip fracture by assessing bone structure using shape and appearance modelling?," *Bone*, pp. 188–193, 2013.

[85] Baker-LePain J., Luker K., Lynch J., Parimi N., Nevitt M., and Lane N., "Active shape modeling of the hip in the prediction of incident hip fracture," *Journal of Bone and Mineral Research*, vol. 26, no. 3, pp. 468–474, 2011.

[86] Steven C M., Johan G B., Boudewijn PF L., Van der G. R. J., Reiber Johan H., and Sonka M., "3-d active appearance models: segmentation of cardiac mr and ultrasound images," *Medical Imaging, IEEE Transactions on*, vol. 21, no. 9, pp. 1167–1178, 2002.

[87] Roberts M., Cootes T., and Adams J., "Automatic segmentation of lumbar vertebrae on digitised radiographs using linked active appearance models," in *Proc. Medical Image Understanding and Analysis*, 2006, vol. 2, pp. 120–124.

[88] Luo Z., Zhuang X., Zhang R., Wang J., Yue C., and Huang X., "Automated 3d segmentation of hippocampus based on active appearance model of brain mr images for the early diagnosis of alzheimer's disease.," *Minerva medica*, vol. 105, no. 2, pp. 157–165, 2014.

[89] Yao J. and Taylor R., "Assessing accuracy factors in deformable 2D/3D medical image registration using a statistical pelvis model," in *Computer Vision, 2003. Proceedings. Ninth IEEE International Conference on*. IEEE, 2003, pp. 1329–1334.

[90] Long L R. and Thoma G. R., "Use of shape models to search digitized spine X-rays," in *Computer-Based Medical Systems, 2000. CBMS 2000. Proceedings. 13th IEEE Symposium on*. IEEE, 2000, pp. 255–260.

[91] Al-Helo S., Alomari R., Chaudhary V., and Al-Zoubi M., "Segmentation of lumbar vertebrae from clinical CT using active shape models and GVF-snake," in *Eng Med Biol Soc Ann, EMBC*. IEEE, 2011, pp. 8033–8036.

[92] Engstrom C. M., Fripp J., Jurcak V., Walker D. G., Salvado O., and Crozier S., "Segmentation of the quadratus lumborum muscle using statistical shape modeling," *Journal of Magnetic Resonance Imaging*, vol. 33, no. 6, pp. 1422–1429, 2011.

[93] De Bruijne M., Lund M. T., Tanko L. B., Pettersen P. C., and Nielsen M., "Quantitative vertebral morphometry using neighbor-conditional shape models," *Med Image Anal*, vol. 11, no. 5, pp. 503–512, 2007.

[94] Mysling P., Petersen K., Nielsen M., and Lillholm M., "A unifying framework for automatic and semi-automatic segmentation of vertebrae from radiographs using sample-driven active shape models," *Machine Vision and Applications*, pp. 1–14, 2012.

[95] Toth R. and Madabhushi A., "Multifeature landmark-free active appearance models: application to prostate mri segmentation," *Medical Imaging, IEEE Transactions on*, vol. 31, no. 8, pp. 1638–1650, 2012.

[96] Sun S., Bauer C., and Beichel R., "Automated 3D segmentation of lungs with lung cancer in CT data using a novel robust active shape model approach," *IEEE T Med Imaging*, vol. 31, no. 2, pp. 449–460, 2012.

[97] Whitmarsh T., Fritscher K., Humbert L., Del-Rio-Barquero L., Schubert R., and Frangi A., "Hip fracture discrimination using 3D reconstructions from dual-energy X-ray absorptiometry," in *Biomedical Imaging: From Nano to Macro, 2011 IEEE International Symposium on*, 2011, pp. 1189–1192.

[98] Thodberg H. and Rosholm A., "Application of the active shape model in a commercial medical device for bone densitometry," *Image and Vision Computing*, vol. 21, no. 13, pp. 1155–1161, 2003.

[99] Christodoulou Christina I., Pattichis Constantinos S., Pantziaris M., and Nico-
laides A., "Texture-based classification of atherosclerotic carotid plaques," *Medical Imaging, IEEE Transactions on*, vol. 22, no. 7, pp. 902–912, 2003.

[100] Alien P., Graham J., Farnell D. J., Marjanovic E. J., Adams J., Jacobs R.,
Karayianni K., Lindh C., Van der S. P., Horner K., and o., "Detecting osteoporosis from dental radiographs using active shape models," in *I S Biomed Imaging (ISBI)*. IEEE, 2007, pp. 1256–1259.

[101] van R. B., Weinans H., Huiskes R., and Odgaard A., "A new method to determine trabecular bone elastic properties and loading using micromechanical finite-element models," *Journal of biomechanics*, vol. 28, no. 1, pp. 69–81, 1995.

[102] Crawford R P., Cann Christopher E., and Keaveny Tony M., "Finite element models predict in vitro vertebral body compressive strength better than quantitative computed tomography," *Bone*, vol. 33, no. 4, pp. 744–750, 2003.

[103] Béatrice C., Yohan P., and Stéphane L., "The mesh-matching algorithm: an automatic 3d mesh generator for finite element structures," *Journal of biomechanics*, vol. 33, no. 8, pp. 1005–1009, 2000.

[104] Sigal Ian A., Hardisty Michael R., and Whyne Cari M., "Mesh-morphing algorithms for specimen-specific finite element modeling," *Journal of biomechanics*, vol. 41, no. 7, pp. 1381–1389, 2008.

[105] Aslan M. S., Ali A., Farag A. A., Arnold B., Chen D., and Xiang P., "3D vertebrae segmentation in CT images with random noises," in *Proceedings of the 2010 20th International Conference on Pattern Recognition*. IEEE Computer Society, 2010, pp. 2290–2293.

[106] Zhang X., Tian J., Deng K., Wu Y., and Li X., "Automatic liver segmentation using a statistical shape model with optimal surface detection," *Biomedical Engineering, IEEE Transactions on*, vol. 57, no. 10, pp. 2622–2626, 2010.

[107] Sotoca J., Inesta J. M., and Belmonte M., "Hand bone segmentation in radioabsorptiometry images for computerised bone mass assessment," *Comput Med Imag Grap*, vol. 27, no. 6, pp. 459–467, 2003.

[108] Cremers D., Tischhauser F., Weickert J., and Schnorr C., "Diffusion snakes: Introducing statistical shape knowledge into the mumford-shah functional," *International journal of computer vision*, vol. 50, no. 3, pp. 295–313, 2002.

[109] Castro-Mateos I., Pozo J., Pereanez M., Lekadir K., Lazary A., and Frangi A. F., "Statistical interspace models (SIMs): Application to robust 3D multi-vertebra segmentation," *IEEE T Med Imaging*, vol. 34, no. 8, pp. 1663–1675, 2015.

[110] Sukno F., Ordás S., Butakoff C., Cruz S., and Frangi A., "Active shape models with invariant optimal features (IOF-ASMs)," in *Audio-and Video-Based Biometric Person Authentication*. Springer, 2005, pp. 365–375.

[111] Cootes T. F., Ionita M., Lindner C., and Sauer P., "Robust and accurate shape model fitting using random forest regression voting," in *Computer Vision–ECCV 2012*, pp. 278–291. Springer, 2012.

[112] Lekadir K., Merrifield R., and G.-Z. Y., "Outlier detection and handling for robust 3D active shape models search," *IEEE T Med Imaging*, vol. 26, no. 2, pp. 212–222, 2007.

[113] Yan P., Xu S., Turkbey B., and Kruecker J., "Discrete deformable model guided by partial active shape model for trus image segmentation," *Biomedical Engineering, IEEE Transactions on*, vol. 57, no. 5, pp. 1158–1166, 2010.

[114] Chaohui W., Olivier T., Fabrice M., Salma E., and Nikos P., "3d knowledge-based segmentation using pose-invariant higher-order graphs," in *Medical Image Computing and Computer-Assisted Intervention–MICCAI 2010*, pp. 189–196. Springer, 2010.

[115] Roberts M., Cootes T., and Adams J., "Automatic location of vertebrae on DXA images using random forest regression," in *Lect Notes Comput Sc (MICCAI)*, pp. 361–368. Springer, 2012.

[116] Boykov Y., Veksler O., and Zabih R., "Fast approximate energy minimization via graph cuts," *IEEE T Pattern Anal*, vol. 23, no. 11, pp. 1222–1239, 2001.

[117] Suinesiaputra A., Frangi Alejandro F., Kaandorp Theodorus A., Lamb Hildo J., Bax Jeroen J., Reiber Johan H., and Lelieveldt Boudewijn P., "Automated detection of regional wall motion abnormalities based on a statistical model applied to multislice short-axis cardiac mr images," *Medical Imaging, IEEE Transactions on*, vol. 28, no. 4, pp. 595–607, 2009.

[118] Castro-Mateos I., Pozo Jose M., and Frangi A., "Multi level statistical shape model (MLSSM) with rebalancing: Application to spine modelling," *Submitted for Publication in Med. Image Analy*, 2016.

[119] Steininger P., Fritscher K., Kofler G., Schuler B., Hanni M., Schwieger K., and Schubert R., "Comparison of different metrics for appearance-model-based 2D/3D-registration with X-ray images," in *Bildverarbeitung fur die Medizin 2008*, pp. 122–126. Springer, 2008.

[120] Fleute M., Lavallee S., and Desbat L., "Integrated approach for matching statistical shape models with intra-operative 2D and 3D data," in *Lect Notes Comput Sc (MICCAI)*, pp. 364–372. Springer, 2002.

[121] Van Assen H. C., Danilouchkine M. G., Frangi A. F., Ordás S., Westenberg J., Reiber J. H., and Lelieveldt B. P., "SPASM: a 3D-ASM for segmentation of sparse and arbitrarily oriented cardiac MRI data," *Med Image Anal*, vol. 10, no. 2, pp. 286–303, 2006.

[122] Zheng G., Gollmer S., Schumann S., Dong X., Feilkas T., and Gonzalez Ballester M., "A 2D/3D correspondence building method for reconstruction of a patient-specific 3D bone surface model using point distribution models and calibrated X-ray images," *Med Image Anal*, vol. 13, no. 6, pp. 883–899, 2009.

[123] Baka N., Kaptein B., de B. M., van W. T., Giphart J., Niessen W. J., and Lelieveldt B. P., "2D–3D shape reconstruction of the distal femur from stereo

X-ray imaging using statistical shape models," *Med Image Anal*, vol. 15, no. 6, pp. 840–850, 2011.

[124] Luo H. and O'Donnell T., "A 3d statistical shape model for the left ventricle of the heart," in *Lect Notes Comput Sc (MICCAI)*. Springer, 2001, pp. 1300–1301.

[125] Mansi T., Voigt I., Leonardi B., Pennec X., Durrleman S., Sermesant M., Delingette H., Taylor Andrew M., Boudjemline Y., Pongiglione G., and Apache N., "A statistical model for quantification and prediction of cardiac remodelling: Application to tetralogy of fallot," *IEEE T Med Imaging*, vol. 30, no. 9, pp. 1605–1616, 2011.

[126] Bredbenner Todd L., Eliason Travis D., Potter Ryan S., Mason Robert L., Havill Lorena M., and Nicolella Daniel P., "Statistical shape modeling describes variation in tibia and femur surface geometry between control and incidence groups from the osteoarthritis initiative database," *Journal of biomechanics*, vol. 43, no. 9, pp. 1780–1786, 2010.

[127] Perperidis D., Mohiaddin R., and Rueckert D., "Construction of a 4d statistical atlas of the cardiac anatomy and its use in classification," in *Medical Image Computing and Computer-Assisted Intervention–MICCAI 2005*, pp. 402–410. Springer, 2005.

[128] Huang H., Makedon F., and McColl R., "High dimensional statistical shape model for medical image analysis," in *Biomedical Imaging: From Nano to Macro, 2008. ISBI 2008. 5th IEEE International Symposium on*. IEEE, 2008, pp. 1541–1544.

[129] Roberts M., Pacheco E., Mohankumar R., Cootes T., and Adams J., "Detection of vertebral fractures in DXA VFA images using statistical models of appearance and a semi-automatic segmentation," *Osteoporosis International*, vol. 21, no. 12, pp. 2037–2046, 2010.

[130] Castro-Mateos I., Pozo J., Lazary A., and Frangi A. F., "3D vertebra segmentation by feature selection active shape model," in *Recent Advances in Com-*

putational Methods and Clinical Applications for Spine Imaging, pp. 241–245. Springer, 2015.

[131] Buckwalter J. A., "Aging and degeneration of the human intervertebral disc.," *Spine*, vol. 20, no. 11, pp. 1307, 1995.

[132] Livshits G., Popham M., Malkin I., Sambrook P. N., Macgregor A. J., Spector T., and Williams F. M. K., "Lumbar disc degeneration and genetic factors are the main risk factors for low back pain in women: the UK twin spine study.," *Ann Rheum Dis*, vol. 70, no. 10, pp. 1740–1745, 2011.

[133] Gibson M., Buckley J., Mawhinney R., Mulholland R., and Worthington B., "Magnetic resonance imaging and discography in the diagnosis of disc degeneration. a comparative study of 50 discs," *J Bone Joint Srug*, vol. 68, no. 3, pp. 369–373, 1986.

[134] Campana S., Charpail E., De Guise J., Rillardon L., Skalli W., and Mitton D., "Relationships between viscoelastic properties of lumbar intervertebral disc and degeneration grade assessed by MRI," *J Mech Behav Biomed*, vol. 4, no. 4, pp. 593 – 599, 2011.

[135] Galbusera F., Schmidt H., Noailly J., Malandrino A., Lacroix D., Wilke H., and Shirazi-Adl A., "Comparison of four methods to simulate swelling in poroelastic finite element models of intervertebral discs," *J Mech Behav Biomed*, vol. 4, no. 7, pp. 1234 – 1241, April 2011.

[136] Wei X. and Cumming I., "A region growing algorithm for insar phase unwrapping," in *Geoscience and Remote Sensing Symposium, 1996. IGARSS '96. 'Remote Sensing for a Sustainable Future.', International*, 1996, vol. 4, pp. 2044– 2046 vol.4.

[137] Chevrefils C., Cheriet F., Aubin C.-E., and Grimard G., "Texture analysis for automatic segmentation of intervertebral disks of scoliotic spines from MR images," *IEEE T Inf Technol B*, vol. 13, no. 4, pp. 608–620, 2009.

[138] Kass M., Witkin A., and Terzopoulos D., "Snakes: Active contour models," *Int J Comput Vision*, vol. 1, no. 4, pp. 321–331, 1988.

[139] Chwialkowski M., Shile P., Peshock R., Pfeifer D., and R.W. P., "Automated detection and evaluation of lumbar discs in MR images," in *Engin. in Med. Biol. Society, 1989.*, nov 1989, pp. 571–572.

[140] Roberts N., Gratin C., and Whitehouse G., "MRI analysis of lumbar intervertebral disc height in young and older populations.," *JMRI-J Magn Reson Im*, vol. 7, no. 5, pp. 880–886, 1997.

[141] Ruiqiong S., Dongmei S., Zhengding Q., and Weiss K., "An efficient method for segmentation of MRI spine images," in *Complex Medical Engineering, 2007. CME 2007. IEEE*, may 2007, pp. 713–717.

[142] Chevrefils C., Cheriet C., Grimard G., and Aubin C., "Watershed segmentation of intervertebral disk and spinal canal from MRI images," in *Lect Notes Comput Sc (ICIAR)*. 2007, pp. 1017–1027, Springer-Verlag Berlin Heidelberg.

[143] Law M., Tay K., Leung A., Garvin G., and Li S., "Intervertebral disc segmentation in MR images using anisotropic oriented flux," *Med Image Anal*, 2012.

[144] Seifert S., Wachter I., Schmelzle G., and Dillmann R., "A knowledge-based approach to soft tissue reconstruction of the cervical spine," *IEEE T Med Imaging*, vol. 28, no. 4, pp. 494–507, april 2009.

[145] Neubert A., Fripp J., Engstrom C., Schwarz R., Lauer L., Salvado O., and Crozier S., "Automated detection, 3D segmentation and analysis of high resolution spine MR images using statistical shape models," *Phys Med Biol*, vol. 57, no. 24, pp. 8357, 2012.

[146] Chevrefils C., Cheriet F., Grimard G., Miron M., and Aubin C., "Quantitative evaluation of an automatic segmentation method for 3D reconstruction of intervertebral scoliotic disks from MR images," *BMC Medical Imaging*, vol. 12, no. 1, pp. 26–40, 2012.

[147] Haq R., Besachio David A., Borgie Roderick C., and Audette Michel A., "Using shape-aware models for lumbar spine intervertebral disc segmentation," in *2014 22nd International Conference on Pattern Recognition (ICPR)*. IEEE, 2014, pp. 3191–3196.

[148] Ghosh S. and Chaudhary V., "Supervised methods for detection and segmentation of tissues in clinical lumbar mri," *Computerized Medical Imaging and Graphics*, vol. 38, no. 7, pp. 639–649, 2014.

[149] Chen C., Belavy D., Yu W., Chu C., Armbrecht G., Bansmann M., Felsenberg D., and Zheng G., "Localization and segmentation of 3d intervertebral discs in mr images by data driven estimation," *Medical Imaging, IEEE Transactions on*, vol. 34, no. 8, pp. 1719–1729, 2015.

[150] Bechara B.-P., Leckie S. K., Bowman B. W., Davies C. E., Woods B. I., Kanal E., Sowa G. A., and Kang J D., "Application of a semiautomated contour segmentation tool to identify the intervertebral nucleus pulposus in MR images," *Am. J. Neuroradiol*, vol. 31, no. 9, pp. 1640–1644, 2010.

[151] Yuan X. and Chi-Fishman G., "Volumetric tongue reconstruction by fusing bidirectional MR images," in *I S Biomed Imaging (ISBI)*, april 2006, pp. 1352 –1355.

[152] Van Ginneken B., Frangi A. F., Staal J. J., ter H. R. B. M., and Viergever M. A., "Active shape model segmentation with optimal features," *IEEE T Med Imaging*, vol. 21, no. 8, pp. 924–933, 2002.

[153] Valstar M., Martinez B., Binefa X., and Pantic M., "Facial point detection using boosted regression and graph models," in *Computer Vision and Pattern Recognition (CVPR), 2010 IEEE Conference on*. IEEE, 2010, pp. 2729–2736.

[154] Milborrow S. and Nicolls F., "Active shape models with sift descriptors and mars.," in *VISAPP (2)*, 2014, pp. 380–387.

[155] Philip F. and Hans-Peter S., "An implementation of triangular b-spline surfaces over arbitrary triangulations," *Computer Aided Geometric Design*, vol. 10, no. 3, pp. 267 – 275, 1993.

[156] Guillemaud R. and Brady M., "Estimating the bias field of mr images," *IEEE T Med Imaging*, vol. 16, no. 3, pp. 238–251, 1997.

[157] Ibánez L., Schroeder W., Ng L., and J. C., *The ITK Software Guide*, Kitware, Inc. ISBN 1-930934-15-7, http://www.itk.org/ItkSoftwareGuide.pdf, second edition, 2005.

[158] Pfirrmann C., Metzdorf A., Zanetti M., Hodler J., and Boos N., "Magnetic resonance classification of lumbar intervertebral disc degeneration," in *Spine*, 2001, vol. 26, pp. 1873–1878.

[159] Zijdenbos A. P., Dawant B. M., Margolin R. A., and Palmer A. C., "Morphometric analysis of white matter lesions in MR images: method and validation," *IEEE T Med Imaging*, vol. 13, no. 4, pp. 716–724, 1994.

[160] Pat L., *Selection of relevant features in machine learning*, Defense Technical Information Center, 1994.

[161] Stern D., Vrtovec T., Pernus F., and Likar B., "Automated determination of the centers of vertebral bodies and intervertebral discs in CT and MR lumbar spine images," in *Proceedings of SPIE*, 2010, vol. 7623, p. 762350.

[162] Peng Z., Zhong J., Wee W., and Lee J.-h., "Automated vertebra detection and segmentation from the whole spine MR images," in *Eng Med Biol Soc Ann. IEEE-EMBS*, jan 2005, pp. 2527–2530.

[163] Okada T., Yokota K., Hori M., Nakamoto M., Nakamura H., and Sato Y., "Construction of hierarchical multi-organ statistical atlases and their application to multi-organ segmentation from ct images," in *Lect Notes Comput Sc (MICCAI)*, pp. 502–509. Springer, 2008.

[164] Lim T. H., Eck J. C., An H. S., Hong J. H., Ahn J.-Y., and You J. W., "Biomechanics of transfixation in pedicle screw instrumentation," *Spine*, vol. 21, no. 19, pp. 2224–2229, 1996.

[165] Jahng T., Kim Y., and Moon K., "Comparison of the biomechanical effect of pedicle-based dynamic stabilization: a study using finite element analysis," *The Spine Journal*, vol. 13, no. 1, pp. 85–94, 2013.

[166] Schlenzka D., Laine T., and Lund T., "Computer-assisted spine surgery," *European Spine Journal*, vol. 9, no. 1, pp. S057–S064, 2000.

[167] Bae M.-H., Pan R., Wu T., and Badea A., "Automated segmentation of mouse brain images using extended mrf," *Neuroimage*, vol. 46, no. 3, pp. 717–725, 2009.

[168] Chen X., Graham J., Hutchinson C., and Muir L., "Automatic generation of statistical pose and shape models for articulated joints," *IEEE T Med Imaging*, vol. 33, no. 2, pp. 372–383, 2014.

[169] Heckemann Rolf A., Hajnal Joseph V., Aljabar P., Rueckert D., and Hammers A., "Automatic anatomical brain mri segmentation combining label propagation and decision fusion," *NeuroImage*, vol. 33, no. 1, pp. 115–126, 2006.

[170] Huang J., Jian F., Wu H., and Li H., "An improved level set method for vertebra CT image segmentation," *Biomedical engineering online*, vol. 12, no. 1, pp. 48, 2013.

[171] Mahmoudi S. and Benjelloun M., "A new approach for cervical vertebrae segmentation," *Progress in Pattern Recognition, Image Analysis and Applications*, pp. 753–762, 2007.

[172] Mastmeyer A., Engelke K., Fuchs C., and Kalender W. A., "A hierarchical 3D segmentation method and the definition of vertebral body coordinate systems for QCT of the lumbar spine," *Med Image Anal*, vol. 10, no. 4, pp. 560–577, 2006.

[173] Tan S., Jianhua Y., Ward M., Yao L., and Summers R., "3D multi-scale level set segmentation of vertebrae," in *I S Biomed Imaging (ISBI)*, 2007, pp. 896–899.

[174] Stern D., Likar B., Pernus F., and Vrtovec T., "Parametric modelling and segmentation of vertebral bodies in 3D CT and MR spine images," *Physics in medicine and biology*, vol. 56, no. 23, pp. 7505–7522, 2011.

[175] Weese J., Kaus M., Lorenz C., Lobregt S., Truyen R., and Pekar V., "Shape constrained deformable models for 3D medical image segmentation," in *Information Processing in Medical Imaging*. Springer, 2001, pp. 380–387.

[176] Kaminsky J., Klinge P., Rodt T., Bokemeyer M., Luedemann W., and Samii M., "Specially adapted interactive tools for an improved 3D-segmentation of the spine," *Comput Med Imag Grap*, vol. 28, no. 3, pp. 119–127, 2004.

[177] Naegel B., "Using mathematical morphology for the anatomical labeling of vertebrae from 3D CT-scan images," *Comput Med Imag Grap*, vol. 31, no. 3, pp. 141–156, 2007.

[178] Ma J. and Lu L., "Hierarchical segmentation and identification of thoracic vertebra using learning-based edge detection and coarse-to-fine deformable model," *Comput Vis Image Und*, pp. 19–27, 2013.

[179] Zhang J., Yan C., Chui C., and Ong S., "Fast segmentation of bone in ct images using 3d adaptive thresholding," *Computers in biology and medicine*, vol. 40, no. 2, pp. 231–236, 2010.

[180] Kirschner M., Becker M., and Wesarg S., "3D active shape model segmentation with nonlinear shape priors," in *Medical Image Computing and Computer-Assisted Intervention–MICCAI 2011*, pp. 492–499. Springer, 2011.

[181] Carballido gamio J., Belongie S. J., and Majumdar S., "Normalized cuts in 3D for spinal MRI segmentation," *IEEE Trans Med Imaging*, vol. 23, pp. 36–44, 2004.

[182] Szu-Hao H., Yi-Hong C., Shang-Hong L., and Novak C., "Learning-based vertebra detection and iterative normalized-cut segmentation for spinal MRI," *IEEE T Med Imaging*, vol. 28, no. 10, pp. 1595–1605, Oct.

[183] Shen H., Litvin A., and Alvino C., "Localized priors for the precise segmentation of individual vertebras from ct volume data," in *Medical Image Computing and Computer-Assisted Intervention–MICCAI 2008*, pp. 367–375. Springer, 2008.

[184] Kim Y. and Kim D., "A fully automatic vertebra segmentation method using 3D deformable fences," *Comput Med Imag Grap*, vol. 33, no. 5, pp. 343–352, 2009.

[185] Klinder T., Ostermann J., Ehm M., Franz A., Kneser R., and Lorenz C., "Automated model-based vertebra detection, identification, and segmentation in CT images.," *Med Image Anal*, vol. 13, no. 3, pp. 471, 2009.

[186] Boisvert J., Pennec X., Labelle H., Cheriet F., and Ayache N., "Principal spine shape deformation modes using Riemannian geometry and articulated models," in *Articulated Motion and Deformable Objects*, pp. 346–355. Springer, 2006.

[187] Van De Giessen M., Streekstra Geert J., Strackee Simon D., Maas M., Grimbergen Kees A., Lucas J V. V., and Vos Frans M., "Constrained registration of the wrist joint," *Medical Imaging, IEEE Transactions on*, vol. 28, no. 12, pp. 1861–1869, 2009.

[188] Kadoury S., Labelle H., and Paragios N., "Spine segmentation in medical images using manifold embeddings and higher-order mrfs," *Medical Imaging, IEEE Transactions on*, vol. 32, no. 7, pp. 1227–1238, 2013.

[189] Rasoulian A., Rohling R., and Abolmaesumi P., "Lumbar spine segmentation using a statistical multi-vertebrae anatomical shape+ pose model," *IEEE T Med Imaging*, vol. 32, no. 10, pp. 1890–1900, 2013.

[190] Seitel A., Rasoulian A., Rohling R., and Abolmaesumi P., "Lumbar and thoracic spine segmentation using a statistical multi-object shape+ pose model," in *Recent Advances in Computational Methods and Clinical Applications for Spine Imaging*, pp. 221–225. Springer, 2015.

[191] Forsberg D., "Atlas-based segmentation of the thoracic and lumbar vertebrae," in *Recent Advances in Computational Methods and Clinical Applications for Spine Imaging*, pp. 215–220. Springer, 2015.

[192] Lorensen William E. and Cline Harvey E., "Marching cubes: A high resolution 3D surface construction algorithm," *SIGGRAPH Comput. Graph.*, vol. 21, pp. 163–169, August 1987.

[193] Mpiperis I., Malassiotis S., and Strintzis Michael G., "Bilinear models for 3-D face and facial expression recognition," *Information Forensics and Security, IEEE Transactions on*, vol. 3, no. 3, pp. 498–511, 2008.

[194] Lilliefors H.-W., "On the kolmogorov-smirnov test for the exponential distribution with mean unknown," *Journal of the American Statistical Association*, vol. 64, no. 325, pp. 387–389, 1969.

[195] Jarque C. and Bera Anil K., "A test for normality of observations and regression residuals," *International Statistical Review/Revue Internationale de Statistique*, pp. 163–172, 1987.

[196] Trujillo-Ortiz A., Hernandez-Walls R., Barba-Rojo K., and Cupul-Magana L., "Hzmvntest: Henze-zirkler's multivariate normality test," A MATLAB file. URL http://www. mathworks.com/matlabcentral/fileexchange/loadFile.do, 2007.

[197] Fletcher P., Lu C., Pizer S., and Joshi S., "Principal geodesic analysis for the study of nonlinear statistics of shape," *Medical Imaging, IEEE Transactions on*, vol. 23, no. 8, pp. 995–1005, 2004.

[198] Dryden I. L. and Mardia K. V., *Statistical shape analysis*, vol. 4, John Wiley & Sons New York, 1998.

[199] S., "Spineweb," http://spineweb.digitalimaginggroup.ca/, 2013, Accessed: 2015-03-24.

[200] Yao J., Glocker B., Klinder T., and Li S., "Recent advances in computational methods and clinical applications for spine imaging," 2015.

[201] Korez R., Ibragimov B., Likar B., Pernuš F., and Vrtovec T., "Interpolation-based shape-constrained deformable model approach for segmentation of vertebrae from CT spine images," in *Recent Advances in Computational Methods and Clinical Applications for Spine Imaging*, pp. 235–240. Springer, 2015.

[202] Hammernik K., Ebner T., Stern D., Urschler M., and Pock T., "Vertebrae segmentation in 3D CT images based on a variational framework," in *Recent Advances in Computational Methods and Clinical Applications for Spine Imaging*, pp. 227–233. Springer, 2015.

[203] Sharan Alok D., Tang Simon Y., and Vaccaro Alexander R., *Basic Science of Spinal Diseases*, JP Medical Ltd, 2013.

[204] Freemont A., Watkins A., Le Maitre C., Jeziorska M., and Hoyland J., "Current understanding of cellular and molecular events in intervertebral disc degeneration: implications for therapy," *The Journal of pathology*, vol. 196, no. 4, pp. 374–379, 2002.

[205] Malandrino A., Pozo José M., Castro-Mateos I., Frangi Alejandro F., van R. M. M., Ito K., Wilke H.-J., Dao Tien T., Tho Marie-Christine Ho B., and Noailly J., "On the relative relevance of subject-specific geometries and degeneration-specific mechanical properties for the study of cell death in human intervertebral disk models," *Frontiers in bioengineering and biotechnology*, vol. 3, 2015.

[206] Luoma K., Riihimäki H., Luukkonen R., Raininko R., Viikari-Juntura E., and Lamminen A., "Low back pain in relation to lumbar disc degeneration.," *Spine*, vol. 25, no. 4, pp. 487–92, 2000.

[207] Fujiwara A., Tamai K., Yamato M., An Howard S., Yoshida H., Saotome K., and Kurihashi A., "The relationship between facet joint osteoarthritis and disc degeneration of the lumbar spine: an MRI study," *European Spine Journal*, vol. 8, no. 5, pp. 396–401, 1999.

[208] Thompson J., Pearce R., Schechter M., Adams M., Tsang I., and Bishop P., "Preliminary evaluation of a scheme for grading the gross morphology of the human intervertebral disc.," *Spine*, vol. 15, no. 5, pp. 411–415, 1990.

[209] Jarman Joshua P., Arpinar Volkan E., Baruah D., Klein Andrew P., Maiman Dennis J., and Muftuler L T., "Intervertebral disc height loss demonstrates the threshold of major pathological changes during degeneration," *European Spine Journal*, pp. 1–7, 2014.

[210] Riesenburger Ron I., Safain Mina G., Ogbuji R., Hayes J., and Hwang Steven W., "A novel classification system of lumbar disc degeneration," *Journal of Clinical Neuroscience*, vol. 22, no. 2, pp. 346–351, 2015.

[211] Derraz F., Beladgham M., and Khelif M., "Application of active contour models in medical image segmentation," in *Information Technology: Coding and Computing, 2004. Proceedings. ITCC 2004. International Conference on*, april 2004, vol. 2, pp. 675 – 681 Vol.2.

[212] Young S. and Krishnapuram R., "A robust approach to image enhancement based on fuzzy logic," *IEEE T Image Process*, vol. 6, no. 6, pp. 808–825, jun 1997.

[213] Zhang J., Zhang J., Lok T., and Lyu M., "A hybrid particle swarm optimization–back-propagation algorithm for feedforward neural network training," *Applied Mathematics and Computation*, vol. 185, no. 2, pp. 1026–1037, 2007.

[214] Lam K. and Yan H., "Fast greedy algorithm for active contours," *Electronics Letters*, vol. 30, no. 1, pp. 21–23, 1994.

[215] Michopoulou S., Boniatis I., Costaridou L., Cavouras D., Panagiotopoulos E., and Panayiotakis G., "Computer assisted characterization of cervical intervertebral disc degeneration in MRI," *Journal of Instrumentation*, vol. 4, no. 05, pp. P05022, 2009.

[216] Ghosh S., Alomari R., Chaudhary V., and Dhillon G., "Composite features for automatic diagnosis of intervertebral disc herniation from lumbar MRI," in *Engin. in Med. Biol. Society,EMBC, 2011*, Sept 2011, pp. 5068 –5071.

[217] Unal Y., Kocer H., and Akkurt H., "A comparison of feature extraction techniques for diagnosis of lumbar intervertebral degenerative disc disease," in *Innovations in Intelligent Systems and Applications (INISTA), 2011 International Symposium on*, june 2011, pp. 490–494.

[218] Alomari R. S., Corso J. J., Chaudhary V., and Dhillon G., "Automatic diagnosis of lumbar disc herniation with shape and appearance features from MRI," in *SPIE Medical Imaging*. International Society for Optics and Photonics, 2010, p. 76241A.

[219] Neubert A., Fripp J., Engstrom C., Walker D., Weber M., Schwarz R., and Crozier S., "Three-dimensional morphological and signal intensity features for detection of intervertebral disc degeneration from magnetic resonance images," *Journal of the American Medical Informatics Association*, vol. 20, no. 6, pp. 1082–1090, 2013.

[220] Lootus M., Kadir T., and Zisserman A., "Automated radiological grading of spinal mri," in *Recent Advances in Computational Methods and Clinical Applications for Spine Imaging*, pp. 119–130. Springer, 2015.

[221] Ruiz-España S., Arana E., and Moratal D., "Semiautomatic computer-aided classification of degenerative lumbar spine disease in magnetic resonance imaging," *Computers in biology and medicine*, vol. 62, pp. 196–205, 2015.

[222] Yushkevich P. A., Piven J., Hazlett H. C., Smith R. G., Ho S., Gee J. C., and Gerig G., "User-guided 3D active contour segmentation of anatomical structures: significantly improved efficiency and reliability.," *NeuroImage*, vol. 31, pp. 1116–1128, 2006 Jul 1 2006.

[223] Newcombe Robert G., "Two-sided confidence intervals for the single proportion: comparison of seven methods," *Statistics in medicine*, vol. 17, no. 8, pp. 857–872, 1998.

[224] Bera Anil K. and Bilias Y., "Rao's score, Neyman's C(α) and Silvey's LM tests: an essay on historical developments and some new results," *Journal of Statistical Planning and Inference*, vol. 97, no. 1, pp. 9–44, 2001.

[225] Malandrino A., Noailly J., Lacroix D., and Beard Daniel A., "The effect of sustained compression on oxygen metabolic transport in the intervertebral disc decreases with degenerative changes," *PLOS Computational Biology*, vol. 7, no. 8, Aug 2011.

[226] Ellingson Arin M., Mehta H., Polly David W., Ellermann J., and Nuckley David J., "Disc degeneration assessed by quantitative T2*(T2 star) correlated with functional lumbar mechanics.," *Spine*, vol. 38, no. 24, pp. E1533–40, 2013.

[227] Hon J Y., Bahri S., Gardner V., and Muftuler L T., "In vivo quantification of lumbar disc degeneration: Assessment of ADC value using a degenerative scoring system based on Pfirrmann framework," *European Spine Journal*, pp. 1–7, 2014.

[228] Comon P., Luciani X., and De Almeida André L., "Tensor decompositions, alternating least squares and other tales," *Journal of Chemometrics*, vol. 23, no. 7-8, pp. 393–405, 2009.

[229] Vasilescu M Alex O. and Terzopoulos D., "Multilinear subspace analysis of image ensembles," in *Proc CVPR IEEE*. IEEE, 2003, vol. 2, pp. II–93.

[230] Tenenbaum Joshua B. and Freeman William T., "Separating style and content with bilinear models," *Neural computation*, vol. 12, no. 6, pp. 1247–1283, 2000.

[231] Geng X., Smith-Miles K., Zhou Z.-H., and Wang L., "Face image modeling by multilinear subspace analysis with missing values," *IEEE T Syst Man Cy B*, vol. 41, no. 3, pp. 881–892, 2011.

[232] Tao D., Song M., Li X., Shen J., Sun J., Wu X., Faloutsos C., and May-
      bank Stephen J., "Bayesian tensor approach for 3-d face modeling," *IEEE
      Trans. Circuits Syst. Video Technol.*, vol. 18, no. 10, pp. 1397–1410, 2008.

[233] Vlasic D., Brand M., Pfister H., and Popović J., "Face transfer with multilinear
      models," *ACM Transactions on Graphics (TOG)*, vol. 24, no. 3, pp. 426–433,
      2005.

[234] Figueras i V. R., Hoogendoorn C., Sukno Federico M., and Frangi Alejandro F.,
      "Bilinear point distribution models for heart motion analysis," in *Biomedical
      Imaging: From Nano to Macro, 2010 IEEE International Symposium on*. IEEE,
      2010, pp. 476–479.

[235] Lecron F., Boisvert J., Benjelloun M. Labelle H., and Mahmoudi S., "Multilevel
      statistical shape models: a new framework for modeling hierarchical structures,"
      in *I S Biomed Imaging (ISBI)*. IEEE, 2012, pp. 1284–1287.

[236] Timmerman Marieke E., "Multilevel component analysis," *British Journal of
      Mathematical and Statistical Psychology*, vol. 59, no. 2, pp. 301–320, 2006.

[237] Smilde Age K., Jansen Jeroen J., Hoefsloot Huub C., Lamers Robert-Jan A.,
      Van Der Greef J., and Timmerman Marieke E., "ANOVA-simultaneous compo-
      nent analysis (ASCA): a new tool for analyzing designed metabolomics data,"
      Bioinformatics, vol. 21, no. 13, pp. 3043–3048, 2005.

[238] Kriegel H.-P., Kröger P., Schubert E., and Zimek A., "A general framework
      for increasing the robustness of pca-based correlation clustering algorithms," in
      Scientific and Statistical Database Management. Springer, 2008, pp. 418–435.

[239] Cattell Raymond B., "The scree test for the number of factors," *Multivariate
      behavioral research*, vol. 1, no. 2, pp. 245–276, 1966.

[240] Felsenberg D., Silman A., Lunt M., Armbrecht G., Ismail A., Finn J., Cockerill
      W., Banzer D., Benevolenskaya L., Bhalla A., and o., "Incidence of vertebral
      fracture in europe: results from the european prospective osteoporosis study

(epos).," *Journal of bone and mineral research: the official journal of the American Society for Bone and Mineral Research*, vol. 17, no. 4, pp. 716–724, 2002.

[241] Castro-Mateos I., Pozo José M., Lazary A., and Frangi A. F., "Automatic construction of patient-specific finite-element mesh of the spine from IVDs and vertebra segmentations," in *SPIE Medical Imaging*. International Society for Optics and Photonics, 2016, pp. 97881U–97881U.

[242] Murphy Martin J., "An automatic six-degree-of-freedom image registration algorithm for image-guided frameless stereotaxic radiosurgery," *Medical Physics*, vol. 24, no. 6, pp. 857–866, 1997.

[243] Markelj P., Tomaževič D., Pernuš F., and Likar B., "Robust gradient-based 3-d/2-d registration of ct and mr to x-ray images," *Medical Imaging, IEEE Transactions on*, vol. 27, no. 12, pp. 1704–1714, 2008.

[244] Gill S., Abolmaesumi P., Fichtinger G., Boisvert J., Pichora D., Borshneck D., and Mousavi P., "Biomechanically constrained groupwise ultrasound to ct registration of the lumbar spine," *Medical image analysis*, vol. 16, no. 3, pp. 662–674, 2012.

[245] Rasoulian A., Abolmaesumi P., and Mousavi P., "Feature-based multibody rigid registration of ct and ultrasound images of lumbar spine," *Medical physics*, vol. 39, no. 6, pp. 3154–3166, 2012.

[246] Steinman David A., Milner Jaques S., Norley Chris J., Lownie Stephen P., and Holdsworth David W., "Image-based computational simulation of flow dynamics in a giant intracranial aneurysm," *American Journal of Neuroradiology*, vol. 24, no. 4, pp. 559–566, 2003.

[247] Sermesant M., Forest C., Pennec X., Delingette H., and Ayache N., "Deformable biomechanical models: Application to 4d cardiac image analysis," *Medical Image Analysis*, vol. 7, no. 4, pp. 475–488, 2003.

[248] Wang Z., Teo Jeremy C.-M., Chui C.-K., Ong Sim H., Yan Chye H., Wang S., Wong H.-K., and Teoh S.-H., "Computational biomechanical modelling of

the lumbar spine using marching-cubes surface smoothened finite element voxel meshing," *Computer methods and programs in biomedicine*, vol. 80, no. 1, pp. 25–35, 2005.

[249] Zhang Z., "Iterative point matching for registration of free-form curves and surfaces," *International journal of computer vision*, vol. 13, no. 2, pp. 119–152, 1994.

[250] Rueckert D., Sonoda L. I., Hayes C., Hill D. L G., Leach M. O., and Hawkes D., "Nonrigid registration using free-form deformations: application to breast MR images," *IEEE T Med Imaging*, vol. 18, no. 8, pp. 712–721, 1999.

[251] Schroeder W., Martin K., and Lorensen B., *The Visualization Toolkit*, Kitware, 2006.

[252] Lafage V., Smith Justin S., Bess S., Schwab Frank J., Ames Christopher P., Klineberg E., Arlet V., Hostin R., Burton Douglas C., and Shaffrey Christopher I., "Sagittal spino-pelvic alignment failures following three column thoracic osteotomy for adult spinal deformity," *Eur Spine J*, vol. 21, no. 4, pp. 698–704, 2012.

[253] Little J.-P. and Adam C.-J., "The effect of soft tissue properties on spinal flexibility in scoliosis: biomechanical simulation of fulcrum bending," *Spine*, vol. 34, no. 2, pp. E76–E82, 2009.

[254] Zheng G., Nolte L.-P., and Ferguson S. J., "Scaled, patient-specific 3D vertebral model reconstruction based on 2D lateral fluoroscopy," *International Journal of Computer Assisted Radiology and Surgery*, vol. 6, no. 3, pp. 351–366, 2011.

[255] Center for C. I. and Simulation Technologies in Biomedicine (CISTIB) at The University of S. U., "Graphical interface for medical image analysis and simulation (GIMIAS)," http://www.gimias.org/, 2016, Accessed: 2016-02-01.